NONLINEAR RESONANCE METHODS FOR ASSESSING ASR SUSCEPTIBILITY DURING CONCRETE PRISM TESTING (CPT)

A Thesis
Presented to
The Academic Faculty

by

Krzysztof J. Leśnicki

In Partial Fulfillment
of the Requirements for the Degree
Master of Science in the
School of Mechanical Engineering

Georgia Institute of Technology
August 2011

NONLINEAR RESONANCE METHODS FOR ASSESSING ASR SUSCEPTIBILITY DURING CONCRETE PRISM TESTING (CPT)

Approved by:

Dr. Laurence J. Jacobs, Advisor
School of Mechanical Engineering
Georgia Institute of Technology

Dr. Kimberly E. Kurtis, Co-Advisor
School of Civil and Environmental Engineering
Georgia Institute of Technology

Dr. Jin-Yeon Kim
School of Civil and Environmental Engineering
Georgia Institute of Technology

Dr. Olivier Pierron
School of Mechanical Engineering
Georgia Institute of Technology

Date Approved: 04/20/2011

ACKNOWLEDGEMENTS

I would like to thank my advisor Dr. Laurence Jacobs and my co-advisor Dr. Kimberly Kurtis for giving me the opportunity to be a part of their research. I greatly appreciate the guidance and support given to me by Dr. Jacobs and Dr. Kurtis throughout my time at Georgia Tech. Their passion for teaching, research, and mentoring of students is inspiring. I especially thank Dr. Jin-Yeon Kim for his dedication and enthusiastic help with my research. His support and extensive knowledge of ultrasonics were instrumental in the progress of my research. I am grateful for his guidance and patience. I would also like to thank Dr. Pierron for taking the time to participate on my thesis committee.

I am thankful for Dr. Jun Chen's help during numerous aspects of the research especially in carrying out preliminary expansion measurements and his help with casting of samples. I would also like to thank the students Brianna Perko and Alex Crotty for their help with the recasting of concrete specimens for petrographic examination. Additionally, I thank Brianna Perko and Kate Raskauskas for their meticulous work with staining and examining concrete samples.

I express my gratitude to fellow students and past students of my lab group and Dr. Kurtis' lab group: Katie Matlack, Frank Bender, Thomas Ruiner, Dennis Schurr, Matthias Seher, Christian Ehrlich, Simon Walker, Dr. Sang Ryul Kim, Yu Liu, Chi Won In, Dr. Jun Chen, Robert Moser, Amal Jayapalan, Brett Holland, Bo Yeon Lee, and Chris Shearer, for providing a friendly work atmosphere as well as their assistance in various matters. Specifically I would like to thank Amal Jayapalan and Robert Moser for their advice and help with laboratory equipment throughout my research.

I would also like to acknowledge the generous funding for this research by the Federal Highway Administration (FHWA), especially Paul Virmani and Fred Faridazar from the Department of Transportation for their support. I also thank Gary Knight and Andy Chafin from Heidelberg cement group for allowing the use of their equipment to aid me in crushing and grading aggregate.

Finally, a special thanks to my friends and family for their support and encouragement, especially my parents. They have sacrificed much in order to provide me with the opportunities I am able to enjoy today and words cannot fully express the appreciation and gratitude I feel for what they have done for me; Thank you.

TABLE OF CONTENTS

CHAPTER 1

CHAPTER 2

CHAPTER 3

CHAPTER 4

CHAPTER 5

CHAPTER 6

CHAPTER 7

CHAPTER 8

CHAPTER 9

CHAPTER 10

APPENDIX A

APPENDIX B

LIST OF TABLES

LIST OF FIGURES

LIST OF SYMBOLS AND ABBREVIATIONS

AMBT	Accelerated mortar bar test
AASHTO	American Association of State Highway and Transportation Officials
ASR	Alkali-silica reaction
ASTM	American Society of Testing and Materials
CPT	Concrete prism test
DFT	Discrete Fourier transform
DC	Direct current
FFT	Fast Fourier transform
FHWA	Federal Highway Administration
HR	Highly reactive
NDE	Nondestructive evaluation
NIRAS	Nonlinear impact resonance acoustic spectroscopy
NR	Nonreactive
NRUS	Nonlinear resonance ultrasound spectroscopy
NRS	Nonlinear reverberation spectroscopy
NWMS	Nonlinear wave modulation spectroscopy
PR	Potentially reactive
PV	Cauchy principle value
QF	Quality factor
RH	Relative humidity
SCMs	Supplementary cementitious materials

A_P	Aggregate proportion
A	Signal amplitude (from FFT)
c	Dashpot constant
C_1	Coefficient proportional to hysteresis parameter
C_3	Coefficient proportional to hysteresis parameter
D	Relative density (OD) of aggregate
E_0	Linear elastic modulus
f	Resonance frequency
f_f	Fundamental frequency
f_0	Linear resonance frequency
$h(t)$	Unit step function
$H\{\ \}$	Hilbert transform
k	Stiffness constant
L	Specimen length in direction of wave propagation
m	Mass
M	Signal amplitude
sgn	Signum function
T_f	Fundamental period
$x_p(t)$	Periodic signal
$x(t)$	Continuous time domain signal
$x[n]$	Sampled time domain signal

α	Hysteresis parameter
β	Coefficient of quadratic anharmonicities
δ	Coefficient of cubic anharmonicities
δ_L	Log decrement
δ_N	Log decrement for N cycles
$\Delta\varepsilon$	Strain amplitude
$\dot{\varepsilon}$	Strain rate
ε	Strain
σ	Stress
θ	Signal phase
Ω	Nonlinear damping parameter proportional to hysteresis parameter
ξ	Damping ratio
ξ_0	Linear damping ratio
η	Nonlinearity parameter proportional to material hysteresis
η_C	Cumulative nonlinearity parameter
v	Wave speed
$\Delta\omega$	Bandwidth of resonance peak
ω_{nat}	Natural frequency (angular)
ω_d	Damped natural frequency (angular)

SUMMARY

This research focuses on the characterization of damage accumulation in concrete specimens. Specifically, a nonlinear vibration technique is used to characterize the damage introduced by ongoing alkali-silica reactions (ASR). The nonlinear resonance testing consists of an analysis of the frequency response of concrete specimens subjected to impact loading. ASR introduces a third gel like phase, which can be expansive in the presence of moisture. The result of ASR is the formation of microcracks and debonding between aggregate and cement phases. Collectively, these changes act to increase the specimens' nonlinearity. As a result, it is found that the concrete samples exhibit nonlinear behavior; mainly a decrease in resonance frequency with an increasing level of excitation strain. The relationship between the amplitude of the response and the amount of frequency shift is used as a parameter to describe the nonlinearity of the specimen. The specimens used in this research are of varying reactivity with respect to ASR, which is induced in accordance with ASTM C 1293. The level of nonlinearity is used as a measure of damage caused by the progress of ASR throughout the one year test duration. These nonlinear resonance results are compared to the traditional measures of expansion described in the standard. The robustness and repeatability of the proposed technique is also investigated by repeated testing of samples assumed to be at a specific damage state. Finally, a petrographic staining technique is used to complement nonlinearity measurements and to further gain understanding of ASR. The results of this study show that the proposed nonlinear resonance methods are very sensitive to microstructural changes and have great potential for quantitative damage assessment in concrete.

CHAPTER 1

INTRODUCTION

1.1 Motivation

Durability is a major concern for infrastructure throughout the United States, as well as the rest of the world. One form of deterioration which may affect concrete structures is the alkali-silica reaction (ASR) [1]. This issue is particularly relevant in regions where there is a reliance on marginal aggregate resources, where low-alkali cement and appropriate supplementary cementing materials (SCMs) are not readily available, and where there is significant exposure to external alkali sources, such as deicing salts and chemicals. However, with more common specifications of longer service life, increasing cement alkali contents, increasing cement content in concrete, and regional exhaustion of nonreactive aggregate sources has resulted in an immediate need for more rapid and reliable assessment of the resistance of concrete mixtures to alkali-silica reaction. That is, it is becoming increasingly important to be able to assess in the lab a specific combination of materials to ensure their long-term durability in the field.

Visual signs of ASR damage include gel staining, cracking, aggregate pop-outs, and relative misalignment between structural members. The degree and pattern of cracking is usually dependent on the restraint of the structure and the level of the reaction [2]; a typical example of the visual signs of ASR is shown in Figure 1.1 [1].

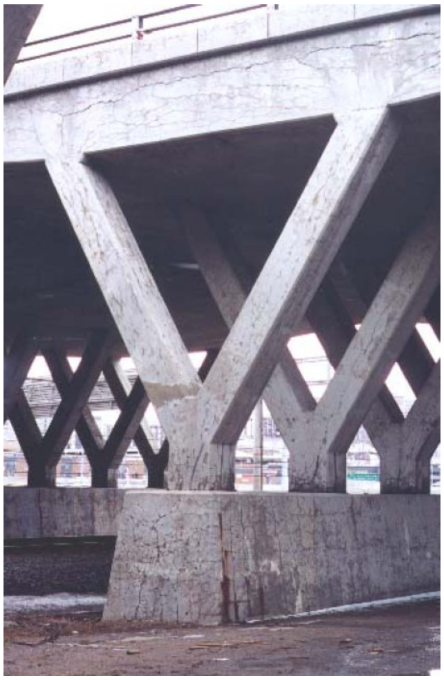

Figure 1.1. ASR in 20 year old highway bridge [1].

1.2 Current Expansion Based Methods

Currently, ASR susceptibility is assessed through length change in the concrete or mortar specimens over time, while subjected to acceleratory conditions. In the United States, the most common standard procedures for this type of test are the “Concrete Prism Test” (CPT), described in ASTM C 1293 [3], and the “Accelerated Mortar Bar Test” (AMBT), described in ASTM C 1260 [4] and ASTM C 1597 [5]. AMBT is a considerably quicker test but it has not been proven to be reliable in all cases. Also, the aggregate must be crushed and sieved to a specified gradation for this test; therefore, the results may not reflect field performance of the uncrushed aggregate. The most accurate, with respect to field performance, method is CPT [2]. For ordinary concrete, the test duration is one year; for concrete containing SCMs, the duration is two years. Expansion on concrete prisms stored over water at 38^{o}C (100^{o}F) is monitored, with expansion of greater than 0.04% by the test end indicating alkali-reactivity, by ASTM C 1293. The prisms should be prepared using cement with Na_2O_e of 0.9±0.1%, with additional alkali added to the mix water to bring the alkali equivalent to 1.25% by mass. The additional internal source of alkali as well as the elevated temperature is believed to accelerate the test, while maintaining good correlation with field performance.

One issue with the test is the long test duration, which is viewed as a considerable drawback [2]. Another drawback of the test is the use of the final expansion measurement as the sole measure of reactivity. For example, it can be difficult to assess the potential of concrete mixtures for reactivity in the field, especially for CPT results close to the expansion limit of 0.04%. A direct measurement of damage would be an improvement. While there have been attempts to relate the degree of reaction to expansion [6], there has still been much discussion centered around the designation of appropriate threshold expansion values as well as the time it takes to cross the threshold, further suggesting that more accuracy in the screening of aggregate for ASR may be necessary.

1.3 Nonlinear Acoustic Techniques

In an effort to improve the nondestructive evaluation of materials, techniques based on wave propagation have been developed over the years. Linear acoustic techniques assume a constant elastic modulus for probing waves and can be applied with Pulse-echo, ultrasonic pulse-velocity, and pulse attenuation techniques. With the pulse echo method, an ultrasonic pulse is sent through the material by a transducer, after which the transducer acts as a receiver for any reflections of the pulse. A defect free material will only have one reflection from the boundary of the specimen. However, when defects are present, there will be multiple reflections allowing easy identification of material flaws. With ultrasonic pulse velocity a wave is sent through a specimen between two positions. The phase velocity can be calculated based on the distance and time of flight for the wave. Samples can be compared based on the calculated phase velocity since defects will cause a decrease in the phase velocity. The final linear technique relies on the attenuation of a propagating wave. As an ultrasonic wave propagates through a specimen, the amplitude of the wave will decrease as a result of interaction with defects, grain boundaries, and internal friction. Presence of defects can then be inferred by measuring the decrease in amplitude of a wave sent between two positions on a specimen. These techniques are in common use but they are not applicable to small scale damage. The changes in nonlinear elastic properties are generally orders of magnitudes higher than the changes in linear elastic properties [7]. Since the changes in nonlinear properties are more pronounced, this offers the opportunity for earlier, as well as more accurate, damage detection using nonlinear NDE techniques.

The earliest nonlinearity work was concerned with nonlinear waves in fluids. This work, in the 18th and 19th centuries, mainly dealt with steepening of a nonlinear wave which leads to the wave "breaking" and creating a shock wave [8]. Classical nonlinear acoustics, which originates from expansion of the elastic strain energy, and the resulting harmonic generation were considered as early as the 1930s. However, application of nonlinear acoustics to solids did not begin until the 1950s with harmonic generation experiments in crystals by Zarembo, Krasil'nikov, and Breazeale [8]. Research in the late 70's by Morris and Richardson showed that measurable nonlinearity, from harmonic generation, could be attributed to microcracks [9, 10].

Additionally, research with geomaterials has led to the definition of a new class of materials ("Structural Nonlinear Elasticity" class) [8]. This class of materials is exemplified by the non-classical hysteretic nonlinear behavior. Studies since the 1940s on the stress-strain relationship and nonlinear behavior of "earth materials" have lead to observation of complicated material behavior. In quasi-static experiments, these materials show considerable nonlinearity in the stress-strain relationship, hysteresis, and discrete memory. The resulting nonlinear effects include harmonic generation, sideband creation from wave cross-modulation, resonance frequency changes, and nonlinear attenuation, all of which are strain amplitude dependent. All of these nonlinear effects can be demonstrated by including nonlinear and hysteretic terms in the constitutive relations and solving the wave equation using the boundary conditions specific to the problem [11].

For flaw detection, the early work in this area was focused on second harmonic generation, which results from classical nonlinearity [10, 12-14]. In this technique, a monotone propagating wave is sent through a sample from one position. As a result of wave interaction with defects and dislocations, a second harmonic of the input wave can be detected at the receiving position. It has been shown that the coefficient of quadratic anharmonicity, β , is proportional to the ratio of the second harmonic amplitude to the square of the primary harmonic amplitude [13]. This technique is widely used in assessing fatigue damage in metals.

Further studies of the hysteretic nonlinear behavior has led to the development of few different techniques, such as nonlinear wave modulation spectroscopy (NWMS) [15-17], nonlinear resonance ultrasound spectroscopy (NRUS) [8, 18-22], scaling subtraction method [23-25], and the technique that has been developed by the present investigators, the nonlinear impact resonance spectroscopy (NIRAS) [26, 27].

NWMS is based on a similar concept to second harmonic generation. However, with two incident waves at frequencies f_1 and f_2, sidebands, at frequencies resulting from the summation and subtraction of the incident frequencies $(f_1 \pm f_2)$, are created instead of a second harmonic and the amplitudes of these waves are related to the quadratic anharmonicity [15]. When hysteresis is present, the sidebands occur at $(f_2 \pm 2f_1)$ and their amplitudes are related to the hysteresis parameter [15]. The techniques have been able to discern damage in a wide variety of materials including Plexiglas, sandstone, and engine components [15]. With regard to ASR damage, NWMS techniques have been applied to AMBT specimens and have shown potential for earlier detection of damage [16, 17].

The scaling subtraction method relies on taking the difference between signals. In a linear system the superposition principal holds and if given a signal at a certain amplitude, A_1, the signal at a higher amplitude would be the original signal scaled by the ratio of the higher amplitude to the original amplitude [23]. For nonlinear systems the superposition principal does not hold and there is a loss of scalability. For experimental measurements, once a reference signal is defined, usually taken as a signal at low amplitude, the SSM signal is created by taking the difference between the recorded signal and the reference signal [24]. The nonlinearity is then deduced by plotting the energy of the SSM signal against the energy of the recorded signal [23]. The result is a power law relationship, where slope can be considered an indication of nonlinearity. This technique is relatively new and has not been widely applied. The experiments demonstrating the technique have tested concrete, lead, and steel samples.

NRUS is a technique that measures the resonance frequency shift with increasing excitation amplitude. Due to the natural amplitude amplification of a resonance mode, this technique can be extremely sensitive, even at low strain amplitudes [8]. The technique is usually applied using transducers sweeping through a range of frequencies which contain a resonance mode of the specimen. NRUS has already been applied to concrete samples with thermal damage [19], reinforced concrete beams [22], bone with mechanical damage [20], and slate with mechanical damage [18]. Initially, the focus in this research was on implementation of the NRUS technique, but the results showed inconsistencies; hence, NIRAS is used for assessment of ASR damage in CPT samples due to the simplicity of the setup as well as consistency and clarity of results.

The NIRAS technique is based on the same basic principles as NRUS. Damaged specimens exhibit nonlinear behavior which is reflected in a decrease in resonance frequency with an increase in the level of excitation [18, 26]. For low levels of strain excitation, it has been shown that there is a linear relation between the relative frequency shift and the excitation amplitude [18]. Since hysteresis effects are dominant in microcracked materials, the ratio of the relative frequency shift to excitation amplitude may be taken as a parameter proportional to one of the nonlinear elastic properties of materials, called the nonlinear hysteresis strength α [18]. This hysteresis strength increases with accumulated damage and can thus be used as a quantitative measure of ASR damage.

1.4 Research Objectives

The aim of this research is to develop a reliable, nonlinear ultrasonic measurement technique that can more quickly quantify damage associated with ASR in concrete specimens. The results of these measurements are compared to the measures of expansion. Additionally, the research focuses on developing an understanding of the sensitivity of the technique as well as ASR through petrographic analysis. This research describes the new technique developed for quantifying ASR damage as well as current results of ongoing testing of concrete prisms undergoing ASR. The research is primarily experimental and the conclusions presented are based on the acquired data.

1.5 Structure of Thesis

This chapter provides the introduction to the research topic which includes the background and motivation for the work as well as brief overview of current standard practices for measuring ASR reactivity and nonlinear techniques used for damage assessment. Chapter 2 introduces the alkali silica reaction and expansion based methods for measuring aggregate reactivity. Chapter 3 describes the creation of the samples and their concrete mixture designs. Chapter 4 describes the nonlinear and vibration theories which this research is based upon. Chapter 5 introduces the analysis techniques and explains the signal processing. Chapter 6 explains the nonlinear measurement techniques and the measurement setups. Chapter 7 describes the petrography techniques used in the research. Chapter 8 presents the measured results for samples described in Chapter 3 as well as the discussion. Chapter 9 presents the conclusions and recommendations from the research. Finally, Chapter 10 includes suggestions for future work based on the remaining questions from the research.

CHAPTER 2

ALKALI SILICA REACTION AND U.S. STANDARD TESTING

2.1 The Alkali Silica Reaction

The alkali silica reaction has complicated mechanisms that result in the formation of an ASR gel reaction product which can be deleterious if it is expansive [28]. The consequences of this reaction were first recorded by Stanton in 1940 [29]. The mechanisms of this reaction and the reasons for subsequent expansion are not yet clearly understood but it is generally accepted that the dissolution of reactive silica is caused by a hydroxide attack [2]. Silica has a tetrahedral structure which leads to a charged surface. The unresolved charges at the surface can be completed by liberation of ions in water. Subsequently, the interaction of the very reactive hydroxide (OH- ion) with silica results in the following reactions [2, 30],

$$\equiv Si - OH^{-} + OH^{-} \longrightarrow \equiv Si - O^{-} + H_2O \tag{2.1}$$

$$\equiv Si - O - Si \equiv +2OH^{-} \longrightarrow 2(\equiv Si - O^{-}) + H_2O \tag{2.2}$$

leading to the dissolution of the silica. Even though the reaction is described as *alkali*-silica, the hydroxide ion is responsible for the initial breakdown of the silica structure. However, a high concentration of alkalis leads to a high concentration of hydroxides (high pH) due to equilibration of charges; therefore, high alkali content indirectly fuels the reaction [2]. Further, the alkali ions may aid in the breakdown of the silicate structure. After the hydroxide reactions, the alkali cations bind to the structure to balance the newly formed negatively charged oxygen atoms forming an alkali-silicate “gel”. The mechanisms of the expansion of the gel are a source of controversy and there is no general agreement upon the mechanism. The theories proposed include osmotic theory and “gel swelling”, or a combination of both [2]. Additionally, there has been a lot of work done showing that presence of calcium is essential in expansion of the ASR “gel” [2]. Regardless of the mechanism, the result is a pressure on the concrete matrix which causes expansion and cracking.

Nevertheless, three ingredients that are accepted to be necessary for the reaction to develop include (i) reactive silica (ii) highly alkaline pore solution and (iii) presence of sufficient moisture. Reactive silica is generally described as poorly crystalline (having an open crystalline framework or disordered amorphous structure). Some examples include opal, chalcedony, microcrystalline to cryptocrystalline or strained quartz, cristobalite, and tridymite [29]. One reason that amorphous silica is more susceptible to ASR is due to its higher rate of solubilization in alkaline solution [2]. This leads to the second requirement of a highly alkaline pore solution. This environment not only increases the silica solubility but also fuels the dissolution as described earlier. The source of the alkalis mainly comes from portland cement (hydraulic cement commonly used for structural concrete [29]), or other internal sources which can include supplementary cementitious materials, aggregates, mixing water, and chemical admixtures. Additional sources can also be external, such as deicing salts and exposure to a marine environment. Finally there must be sufficient moisture available for the expansion of the reaction product. In general, a relative humidity of 80% or higher is required for significant expansion due to ASR [2].

The result of destructive ASR is a gel which swells in the presence of sufficient amounts of moisture, leading to expansion, cracking, increased permeability, and decreased mechanical strength and stiffness [28, 29]. Concrete, as a brittle material, is particularly susceptible to cracking as a result of swelling of the gel due to its low tensile strength as well as weaker interfacial zones at the cement and aggregate boundary. In order to test aggregates for ASR susceptibility, standard testing procedures have been developed based on the observable expansion of laboratory specimens undergoing ASR. In order to test the reactivity of aggregates, the test methods incorporate sufficient moisture and alkalis in the testing procedures, as described in the subsequent sections. Although there are many forms of expansion testing available, this research only utilizes two of the most common procedures used in the United States.

2.2 Concrete Prism Testing through ASTM C 1293

ASTM C 1293, the Concrete Prism Test (CPT) was developed to provide a more reliable assessment of reactivity of aggregates and it has been continually modified to correctly identify known reactive sources [31]. The current version of the test requires 420 kg/m^3 (708 lb/yd3) of cement content, cement with Na_2O_e of 0.9±0.1%, and the alkali content raised to 1.25% Na_2O_e by mass of cement by addition of NaOH to the mixing water [3]. At least three samples must be cast with a length of 285 mm and a 75 mm square cross section $(3in \times 3in \times 11.25\ in)$. This test allows the testing of both coarse and fine aggregate separately. When testing coarse aggregate, a nonreactive fine aggregate is used in the mix design with a fineness modulus of 2.7 ± 0.2 and the coarse aggregate must meet the grading requirements shown in Table 2.1. A fine aggregate is tested with the grading as delivered from the source and a nonreactive coarse aggregate graded according to Table 2.1. In either case, the nonreactive aggregate used must develop less than 0.1% expansion at the end of 14 days in the accelerated mortar bar test (ASTM C 1260). The water to cement ratio must be kept in the range of 0.42 to 0.45. The samples must be initially cured in a moist environment for 23.5 ± 0.5 hours. The first zero reading is required right after demolding of the samples. Subsequently, those samples need to be transferred to a container which is kept at 38 ± 2°C (100.4 °F). The containers that are recommended are 19-22 L pails with airtight lids. The containers must also have perforated racks that elevate the samples above 20 ± 5 mm of water. Additionally, there must be wicks around the inside wall of the container that extend from the top of the container to the water line to limit alkali leaching. Subsequent expansion measurements must be made at 7, 28, 56 days as well as 3, 6, 9, and 12 months. If supplementary cementitious materials are used, additional readings are also required at 18 and 24 months. According to the standard, an average expansion of 0.04% or greater indicates a reactive aggregate. Where % expansion is measured as the difference between the initial zero reading and the current reading normalized by the gauge length of 250 mm . For more details refer to ASTM C 1293 and ASTM C 490 [3, 32].

Table 2.1. Grading requirement for ASTM C 1293.

Sieve Size		**Mass Fraction**	
Passing	**Retained On**	Coarse	Intermediate
19.0 mm	12.5 mm	$\frac{1}{3}$	--
12.5 mm	9.5 mm	$\frac{1}{3}$	$\frac{1}{2}$
9.5 mm	4.75 mm	$\frac{1}{3}$	$\frac{1}{2}$

2.3 Accelerated Mortar Bar Testing

2.3.1 ASTM C 1260/ C 1567

ASTM C 1260, the Accelerated Mortar Bar Test (AMBT), adopted in 1994 from a technique developed in National Building Research Institute (NBRI) in the Republic of South Africa, is widely used in North America [4, 31]. This standard requires a specific gradation, shown in Table 2.2, of the aggregate in question which is suitable for fine aggregate samples. However, coarse aggregate can be crushed to fit the specified requirements, but the results may not reflect the actual performance of the source, unless there is no difference in mineralogy between the whole and crushed aggregate [4]. The ratio of cement to aggregate content is specified as 1:2.25 when the aggregate has an oven-dry (OD) relative density of 2.45 or higher. When the aggregate relative density is less than 2.45 then aggregate proportion, A_P, is determined by the following equation,

$$A_P = 2.45 \times \frac{D}{2.65} \tag{2.3}$$

where

D = relative density (OD) of aggregate;

Table 2.2. ASTM C 1260 grading requirements.

Sieve Size		Mass %
Passing	**Retained On**	
4.75 mm (No. 4)	2.36 mm (No. 8)	10
2.36 mm (No.8)	1.18 mm (No. 16)	25
1.18 mm (No. 16)	600 μm (No. 30)	25
600 μm (No. 30)	300 μm (No. 50)	25
300 μm (No. 50)	150 μm (No. 100)	15

For three specimens, the required cement content is 440 g with a water to cement ratio of 0.47 by mass of cement. At least three mortar bars must be made with dimensions of $25\,mm \times 25\,mm \times 285\,mm$ $(1in \times 1in \times 11.25\,in)$. After casting, the samples need to be cured in a moist cabinet or room for 24 ± 2 hours. After demolding, the samples need an additional 24 hours of curing while immersed in tap water at 80°C (176 °F). The initial zero readings are performed after the end of this curing period. The mortar bars are then immersed in a 1N NaOH solution at 80 °C (176 °F) in a sealed container. The samples are removed from the NaOH solution at regular intervals for expansion measurements as prescribed by ASTM C 1260 throughout the 14 day duration [4]. According to the standard, aggregates are described as non-reactive when expansion is less than 0.10%, potentially reactive when expansion is between 0.10 and 0.20%, or reactive when expansion is greater than 0.20% (% expansion is calculated the same way as for ASTM C 1293 described in ASTM C 490 [32])

For testing reactivity of aggregate with supplemental cementitious materials (SCMs), ASTM C 1567 [5] is used instead, which is a modified version of ASTM C 1260, where a percentage of cement is replaced by the supplemental cementitious material. When metakaolin or silica fume is used a high range water reducer is allowed if improvements in workability are required.

2.3.2 AASHTO T 303

Another common AMBT procedure comes from the American Association of State Highway and Transportation Officials (AASHTO). AASHTO T 303 [33] is very similar to the methodology of ASTM C 1260. The key difference between the methods is in the water to cement ratio. AASHTO T 303 requires a water to cement ratio of 0.5 instead of the 0.47 prescribed by ASTM C 1260. Additionally, AASHTO T 303 does not consider the use of SCMs.

2.4 Limitations of Expansion Based Methods

Expansion based techniques are only applicable to prevention of ASR and cannot be used or readily adopted to monitoring of structures in the field. These testing techniques rely on threshold values and hence there is ambiguity when results are at or near the developed expansion limits. When Thomas et al. tested 184 samples with different combinations of materials, 40% were considered inconclusive [31]. Additionally, there is constant debate about the definition of these limits. While work has been done to try to correlate expansion with the level of damage [6], a direct link between expansion and ASR damage has not been established. Moreover, if there is no field data for a concrete mixture it can be difficult to use results from these test methods to assess the ASR potential since the expansion thresholds have been changed based on comparison to field data.

CHAPTER 3

MATERIALS AND SAMPLE MATRIX

3.1 Mix Designs

In this research the aggregate sources were chosen in order provide a spectrum of reactivity for assessment through the NIRAS technique. The mix design matrix is shown in Table 3.1. All specimens were cast according to the ASTM C 1293 standard. The nonreactive aggregate used in all the mix designs is a limestone from Adairsville, GA.

Table 3.1. Mix design matrix for ASTM C 1293 concrete prisms.

	Coarse Aggregate	**Fine Aggregate**	**SCMs**	**Reactive Aggregate Source**	**Cast Date**	**14-day AMBT Expansion**
Mix 1	NR	NR	--	--	7/23/2009	0.0787%
Mix 2	HR1	NR	--	Las Placitas, NM gravel	4/1/2010	--
Mix 3	NR	HR1	--	Las Placitas, NM gravel (crushed)	4/22/2010	0.8533%
Mix 4	HR2	NR	--	Spratt limestone, Canada	9/17/2009	--
Mix 5	NR	HR2	--	Spratt limestone, Canada (crushed)	4/29/2010	0.2661%
Mix 6	NR	PR1	--	Alabama Sand, AL	11/5/2009	0.1555%
Mix 7	NR	PR2	--	Galena Road Gravel Sand, Peoria, IL	3/18/2010	0.2088%
Mix 8	HR2	NR	25% Class F fly ash	Spratt limestone, Canada	5/17/2010	--
Mix 9	NR	HR2	25% Class F fly ash	Spratt limestone, Canada(crushed)	5/6/2010	--
Mix 10	HR1	NR	25% Class F fly ash	Las Placitas, NM gravel	2/4/2011	

NR = nonreactive (ASTM C 1260 expansion < 0.1%)
PR = potentially reactive (ASTM C 1260 expansion ~ 0.1-0.2%)
HR = highly reactive (ASTM C 1260 expansion > 0.2%)

Additionally, a Type I cement with alkali equivalent of 0.88%, meeting the ASTM C 1293 requirements, was obtained from Lehigh Heidelberg Cement Group's facility in Evansville, Pennsylvania. This cement was used in the casting of CPT samples. Physical and chemical properties of this cement are summarized in Table 3.2.

Table 3.2. Chemical analysis data for Type I cement.

Chemical Requirements ASTM C 114	**Test Result**	**ASTM C150 Specification Limits for Type I Cement**
Silicon Dioxide (SiO_2)	19.11%	
Aluminum Oxide (Al_2O_3)	4.99%	
Ferric Oxide (Fe_2O_3)	3.55%	
Calcium Oxide (CaO)	60.66%	
Magnesium Oxide (MgO)	3.24%	6.0% max
Sulfur Trioxide (SO_3)	3.96%*	3.0% max
Ignition Loss	2.71%	3.0% max
Insoluble Residue	0.24%	0.75% max
Carbon Dioxide - CO_2	1.71%	
Limestone	4.1 %	5 % max.
$CaCO_3$ % in Limestone	94.5%	70 % min
Tricalcium Silicate (C_3S)	42.9%	
Tricalcium Aluminate (C_3A)	7.0%	< 8%
$C_3S + 4.75C_3A$	76%	
Equivalent Alkalies($Na_2O+0.658K_2O$)	0.88%	
Chloride (Cl)	0.01%	

*Although the SO_3 result slightly exceeds the specification, this source (due to its high alkali content) is commonly used for CPT testing.

3.1.1 Preliminary Assessment of Reactivity

The preliminary assessment of reactivity, shown in Table 3.1, was done using ASTM C 1260 during 14-day test duration as described in Chapter 2. These preliminary measurements were performed in order to estimate the reactivity of the selected aggregates. In addition, the AMBT results can be compared with the results from nonlinearity and ASTM C 1293 expansion measurements. Images of the “as received” aggregates are presented in Figure 3.1. The “as received” aggregate was crushed, when necessary, to fit the grading requirements prescribed in ASTM C 1260. The samples were initially cured at about 100% relative humidity and 23 °C (73.4 °F). The average expansion of the three samples at 14 days is presented in Table 3.1,

(a) Las Placitas gravel

(b) Spratt limestone

(c) Adairsville limestone (coarse)

(d) Adairsville limestone (fine)

(e) Alabama sand

(f) Galena road gravel

Figure 3.1. Images of aggregates used in mix designs, as received.

3.1.2 Concrete Prism Samples

All CPT samples were prepared using the ASTM C 1293 testing procedure and cast using the mixer (Eirich R08W) shown in Figure 3.2. Each sample was cast with a water to cement ratio of 0.45. The gradation for coarse aggregate is as specified in ASTM C 1293. For fine aggregates, the gradation is as received and adjusted to have a fineness modulus (FM) of 2.71. Where applicable, crushed aggregate is also graded to achieve a fineness modulus of 2.71. The crushing is done using a jaw crusher, shown in Figure 3.3. Some of the aggregate was crushed at Heidelberg Cement Group using a larger jaw crusher due to the large volume of aggregate.

Figure 3.2. Concrete mixer.

Figure 3.3. Jaw crusher used for crushing aggregates.

For each mix design, a total of eight specimens were cast, six with studs for expansion measurements and two without studs for petrographic examination, which are reserved for microscopic examination and not tested for expansion. Three samples with studs and a petrographic sample (sample without studs) are kept in plastic pails, as described in Chapter 2. These containers are kept in an environmental chamber kept at 38 ± 2°C, shown in Figure 3.4. The rest of the specimens are kept for reference at room temperature. All expansion measurements are made using a comparator (Humboldt) and a steel reference bar, shown in Figure 3.5.

Figure 3.4. Storage of samples in environmental chamber.

Figure 3.5. Comparator for expansion measurements.

CHAPTER 4

THEORETICAL BACKGROUND

4.1 Nonlinear Acoustic Theory

As mentioned in the introduction, classical nonlinearity can be accounted for by expansion of the strain energy, in powers of the strain tensor. Materials which exhibit classical nonlinear behavior include most fluids and monocrystalline solids; they belong to the "Atomic-Elasticity" class, where the lattice anharmonicity is responsible for nonlinearity [8]. In contrast, for materials belonging to the "Structural Nonlinear Elasticity" class, the nonlinearity is a result of the nonlinear bond system. This class of materials has a larger nonlinear response than the atomic elastic materials [8].

It is well known that cracks within a material decrease its resonance frequency by decreasing the overall stiffness of the structure. In addition to this linear change in frequency, there are also prominent nonlinear effects, including the strain amplitude dependent resonance frequency shift [10, 34]. While the physical nature of nonlinear effects is still not fully understood, there is evidence that the cause of nonlinearity can be attributed to the closing, opening, and interaction of microcracks [10]. Microcracks inside a material form a network which acts as a nonlinear bond system. The nonlinear behavior of this bond system can be attributed to Hertzian contact of crack faces and/or opening and closing of cracks in response to exciting wave motion. Presence of fluids further complicates the behavior of the system. Under full saturation conditions, it has been shown, by Ostrovsky and Johnson [8], through modeling that the nonlinearity can decrease. However, with low to moderate saturation, the nonlinearity increases due to thin film fluid effects such as capillary action and dipole forces [8].

The development of the equation of state for the “Structural Nonlinear Elasticity” class of materials which includes the hysteretic and discrete memory behavior relies on the implementation of the Priesach-Mayergoyz space model. This model considers the “soft” portions of the bond system (microcracks) can be modeled as a collection of hysteretic elastic units [11]. These hysteretic elastic units are dependent on the length as well as applied pressure as illustrated in Figure 4.1,

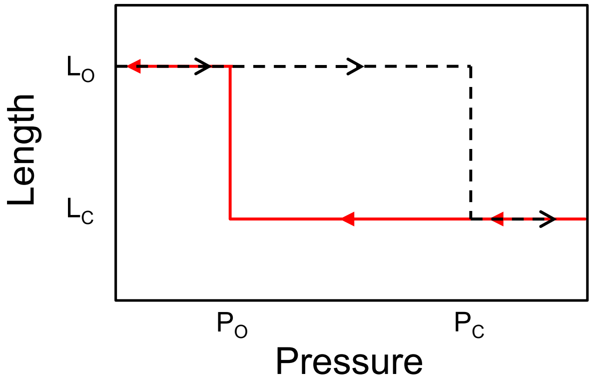

Figure 4.1. Schematic for behavior of hysteretic elastic unit.

In this model, given the equilibrium length at low pressure, L_O, the length changes to L_C upon application of the pressure P_C and back to L_O upon relaxation to the pressure P_O. Using the phenomenological PM space model for hysteresis and classical nonlinear constitutive relations, the nonlinear stress-strain relationship has been shown to be [18, 26, 35, 36],

$$\sigma = \varepsilon \cdot E_0 \left[1 + \beta\varepsilon + \delta\varepsilon^2 + \alpha\left(\Delta\varepsilon + \varepsilon \cdot \operatorname{sgn}(\dot{\varepsilon})\right) \right] \tag{4.1}$$

where

σ = stress, $\frac{N}{m^2}$;

E_0 = linear elastic modulus, $\frac{N}{m^2}$;

β = coefficient of quadratic anharmonicity;

δ = coefficient of cubic anharmonicity;

ε = strain, $\frac{\Delta L}{L}$, where L is length;

α = measure of the material hysteresis;

$\Delta\varepsilon$ = strain amplitude;

$\dot{\varepsilon}$ = strain rate, $\frac{\varepsilon}{\text{second}}$;

$\text{sgn}(\dot{\varepsilon}) = 1$ if $\dot{\varepsilon} > 0$, -1 if $\dot{\varepsilon} < 0$, and 0 if $\dot{\varepsilon} = 0$;

Assuming that effects of hysteresis are dominant in microcracked materials, it has been demonstrated, by using Eq (4.1) in the wave equation and calculating the nonlinear contribution, that the following relationship between frequency shift and strain amplitude is valid for low levels of strain excitation [18, 35, 36],

$$\frac{f_0 - f}{f_0} = C_1 \Delta\varepsilon \tag{4.2}$$

where

f_0 = linear resonance frequency, Hz;

f = resonance frequency at increased excitation amplitude, Hz;

C_1 = coefficient proportional to material hysteresis;

At higher amplitudes there is also an additional quadratic term for the strain amplitude, $D_1 \Delta \varepsilon^2$; however, since the experiments are performed at low levels of strain excitation, this higher order term can be ignored. In these experiments, the amplitude of the displacement or acceleration signal, A, which is proportional to the strain amplitude, is measured instead of strain amplitude. As a result, the absolute hysteresis parameter, α, is not measured. Instead, a scaled hysteresis parameter (η) proportional to α is used as a measure of the material's nonlinearity. The relation used in this investigation is then given by,

$$\frac{f_0 - f}{f_0} = \eta A \tag{4.3}$$

The extraction of the parameter η from recorded data is explained in detail in Chapter 6. An additional effect observed for hysteretic materials is the increase in damping for increasing damage (microcrack density in the sample). It has been demonstrated that there exists a linear relation between change in damping and the strain amplitude [18],

$$\frac{\xi - \xi_0}{\xi_0} = C_3 \Delta \varepsilon \tag{4.4}$$

where

ξ_0 = linear damping ratio;

ξ = damping ratio at increased excitation amplitude;

C_3 = coefficient proportional to material hysteresis;

Since the acceleration amplitude is proportional to strain amplitude,

$$\frac{\xi - \xi_0}{\xi_0} = \Omega A \tag{4.5}$$

where is Ω termed the nonlinear damping parameter.

Since the nonlinearity can attributed to interaction of crack surfaces [8, 10, 37], it is reasonable to assume relatively large and open cracks will not contribute to nonlinearity. It has been shown that second harmonic generation, which is related to β in Eq. (4.1), is dependent on the pressure applied to the crack faces [10, 37]. The results of the studies conducted by Morris et al. and Kim et al. have shown that when cracks are subjected to external pressures (compressive or tensile) the nonlinearity decreases significantly [10, 37]. Since the external compressive or tensile forces restrict motion of the crack faces, the decrease in nonlinearity can be attributed to the lack of contact between the crack faces. Based on this result, a large open crack would not contribute to nonlinearity. Although these studies were only considered for β it is assumed the results also apply to nonlinearity from hysteresis. Furthermore, the work by Gist [38] has shown compelling evidence that hysteretic behavior is a result of the bond system. In this work, sandstone samples were tested in a quasi-static pressure test, where velocity was measured as a function of the applied pressure. The results showed strong hysteretic behavior and dependence of velocity on pressure amplitude. Subsequently, the samples were filled with epoxy, under vacuum, and spun to remove epoxy from rounded pores [8]. Repetition of the pressure test on the epoxy filled specimens resulted in the elimination of hysteresis as well as dependence of velocity on applied pressure, indicating microcracks are indeed responsible for the nonlinearity. Additionally, in the present study, ASR gel can migrate and completely fill newly formed cracks, which can also be responsible for decreased nonlinearity. Under these assumptions, the nonlinearity parameter can be thought of as an "instantaneous" measure of nonlinearity. Since the measurements for tracking nonlinearity in CPT samples are taken at rather large intervals of time the "cumulative" nonlinearity (η_C) can be measured by integration,

$$\eta_C = \int_0^t \eta(\tau)\,d\tau \tag{4.6}$$

With experimental data, a Riemann sum can be used to approximate this integral,

$$\eta_C \approx \frac{1}{2}\sum_{i=2}^{N}(t_i - t_{i-1})(\eta(t_i) + \eta(t_{i-1})) \tag{4.7}$$

This sum is considered a measure of the cumulative damage acquired throughout the test.

4.2 Vibration Theory

The central focus of this work is the use of impact excitation for a vibration analysis from which nonlinear parameters are extracted; therefore this section will serve as a brief overview of the dynamics of vibrations.

The resonance or modal response of a specimen to an impulse is oscillatory and can be modeled by a simple single degree of freedom mass-spring-damper system, illustrated in Figure 4.2.

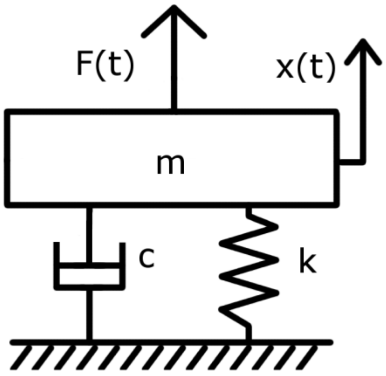

Figure 4.2. Schematic of mass-spring-damper system.

The equation of motion for this system can be found by equating forces. If the displacement is taken from the static equilibrium position the equation of motion becomes,

$$m\ddot{x} + c\dot{x} + kx = F(t) \tag{4.8}$$

This can be normalized by the mass, leading to the following equation,

$$\ddot{x} + 2\xi\omega_{nat}\dot{x} + \omega_{nat}^{2}x = \frac{F(t)}{m} \tag{4.9}$$

where the natural frequency ω_{nat} and damping ratio ξ are defined as,

$$\omega_{nat} = \sqrt{\frac{k}{m}} \tag{4.10}$$

$$\xi = \frac{c}{2\sqrt{km}} \tag{4.11}$$

If the excitation is an impulse, such as a hammer impact, the response is given by [39],

$$x(t) = \frac{1}{m\omega_d} \exp\left(-\xi\omega_{nat} t\right) \sin(\omega_d t) h(t) \tag{4.12}$$

where ω_d is the damped natural frequency,

$$\omega_d = \omega_{nat} \sqrt{1 - \xi^2} \tag{4.13}$$

and $h(t)$ is the unit step function,

$$h(t) = \begin{cases} 1 & t > 0 \\ 0 & otherwise \end{cases} \tag{4.14}$$

CHAPTER 5

SIGNAL PROCESSING BACKGROUND

5.1 Resonance Analysis

As described in Chapter 4, the extraction of the nonlinearity parameter requires measurement of the resonance frequency of a sample. Regardless of the excitation method, a Fourier Transform can be used to extract the frequency information from a recorded signal.

5.1.1 Fourier Series

Any periodic signal, $x_p(t)$, can be represented as a summation of sinusoids at integer multiples of the fundamental frequency, f_f, of the periodic signal. In exponential format the signal can be represented by a Fourier series,

$$x_p(t) = \sum_{k=-\infty}^{\infty} X[k] \exp\left(j2\pi k f_f t\right) \tag{5.1}$$

where the Fourier series coefficients, $X[k]$, are given by,

$$X[k] = \frac{1}{T_f} \int_{T_f} x_p(t) \exp(-j2\pi k f_f t)\, dt \tag{5.2}$$

and T_f is the fundamental period. This concept of a Fourier series can be extended to an aperiodic signal by extending the period of the signal to infinity which leads to the Fourier transformation of the signal.

5.1.2 Fourier Transform

The Fourier transform maps a time domain signal to the frequency domain. Equation (5.2) can be rearranged to eliminate its dependence on the fundamental period,

$$T_f X[k] = \int_{-T_f/2}^{T_f/2} x_p(t) \exp(-j2\pi k f_f t)\, dt \tag{5.3}$$

Now if the fundamental period is extended to infinity the discrete frequencies, kf_f, can be replaced by the continuous frequency f, resulting in,

$$X(f) = \lim_{T_f \to \infty} T_f X[k] = \int_{-\infty}^{\infty} x(t) \exp(-j2\pi f t)\, dt \tag{5.4}$$

which is the Fourier transform of the aperiodic signal $x(t)$ [40].

5.1.3 Discrete Fourier Transform

However, signal acquisition is most commonly achieved through digital devices where the analog input signal is recorded at a specific rate, termed the sampling frequency, F_S. The acquired signal is then discrete in time, $x[n]$, with N samples. In this case the sampled signal can be transformed to the frequency domain using the discrete Fourier transform (DFT) [40],

$$X_{DFT}[k] = \sum_{n=0}^{N-1} x[n] \exp\left[-{j2\pi nk}\middle/{N}\right] \tag{5.5}$$

A requirement that must be met for the sampling frequency in order to achieve the correct frequency spectrum is that the sampling frequency must be greater than twice the maximum frequency of the input signal [40]. This condition is met for all signals acquired in this research by having a sufficiently high sampling rate.

5.1.4 Fast Fourier Transform

The fast Fourier Transform is the generic term for algorithms that compute the DFT efficiently. The DFT normally requires a total of N^2 computations and FFTs reduce these calculation. The software package Matlab® is used throughout the analysis in this research to compute the FFT and it must be noted that the output from the FFT function in Matlab is normalized by a factor of $2/N$ for the presentation of results in the frequency domain. The result is doubled as only the one sided spectrum is shown in the results and the division by the number of sample points is necessary to recover the correct amplitude.

5.2 Damping Analysis

As discussed in Chapter 4, damping of a damaged specimen also changes with the level of excitation. The damping analysis is applied to the vibration signals acquired from impact testing of specimens. The response of a specimen to an impact is a decaying sinusoid, where the envelope is related to the damping in the specimen as discussed in Chapter 4.2. The envelope of the response can be approximated using the Hilbert Transform discussed in the following section. Other techniques for approximating the damping parameter include using the quality factor and the log decrement method which are also discussed in this chapter.

5.2.1 Envelope Approximation

The Hilbert transform creates a complex-valued analytic signal of a real signal. The analytic signal consists of the real part, which is the original signal, and an imaginary part which has a 90° phase shift relative to the original data. So for a given signal $x(t)$ the Hilbert transform is $H\{x(t)\} = v(t)$ and the analytic signal is given as $s(t) = x(t) + jv(t)$. The Hilbert Transform is defined as [41],

$$H\{x(t)\} = v(t) = \frac{1}{\pi} PV \int \frac{s(t')}{t - t'} dt' \tag{5.6}$$

where PV designates the Cauchy principal value of the integral,

$$PV \int_{-\infty}^{\infty} f(x)dx = \lim_{R \longrightarrow \infty} \int_{-R}^{R} f(x)dx \tag{5.7}$$

assuming the integral is convergent. If the integral is not convergent it may still be possible to calculate the principal value for the continuous function $f(x) = P(x)/Q(x)$ by the residue theory. This is done by replacing the variable x with the complex variable z and integrating over a closed contour C that encloses all the poles of $f(z)$ in the upper half plane,

$$PV \int_{-\infty}^{\infty} f(x)dx = \oint_{C} f(z)dz \tag{5.8}$$

Any advanced mathematics textbook can be consulted for more information on the residue theory and Cauchy's principal value, such as the work by Zill and Wright [42]. The analytic signal can also by represented in the complex plane using Euler's identity,

$$s(t) = M \exp(-j\theta) \tag{5.9}$$

where

$$M = \sqrt{x(t)^2 + v(t)^2} \tag{5.10}$$

$$\theta = \arctan\left(\frac{v(t)}{x(t)}\right) \tag{5.11}$$

Taking the magnitude of the analytic signal gives the instantaneous amplitude which approximates the envelope of the signal. For example, consider the signal encountered from a natural vibration of a specimen,

$$x(t) = e^{-at}\cos(\omega t - \phi) \tag{5.12}$$

Using the product theorem for Hilbert transforms [41, 43],

$$H\{x_1 x_2\} = x_1 H\{x_2\} \tag{5.13}$$

the analytic signal is then given by,

$$s(t) = e^{-at}\left(\cos(\omega t - \phi) + j\sin(\omega t - \phi)\right) \tag{5.14}$$

and the instantaneous magnitude of the analytic signal is given by,

$$\left|s(t)\right| = \sqrt{\left(e^{-at}\sin(\omega t - \phi)\right)^2 + \left(e^{-at}\sin(\omega t - \phi)\right)^2} = e^{-at} \tag{5.15}$$

However, for the product theorem to hold true, the spectrum for x_1 must be zero for $\left|\omega\right| \geq \omega_1$ and x_2 must be zero for $\left|\omega\right| \leq \omega_1$, where ω_1 is any chosen frequency. Since the spectrum of a decaying exponential dies out very quickly with frequency, it has negligible amplitude in the frequency range of interest (around damped natural frequency) and the natural vibration has negligible amplitude at lower frequencies; therefore the product theorem holds for the signals in this research. One issue with this method, which is discussed in Appendix A, arises when the there is amplitude modulation caused by beating of a signal. When this occurs, it can be difficult to relate the envelope and the decay rate.

Digitally collected data however is discrete in time and a discrete Hilbert transform is calculated using Matlab ® based on the DFT of the original sequence, as suggested by Marple [44].

5.2.2 Quality Factor

Another approach to estimate damping, assuming the simple mass-spring-damper model, is to use the quality factor. The quality factor (QF) is defined as,

$$QF \equiv \frac{\omega_{nat}}{\Delta\omega} \tag{5.16}$$

where $\Delta\omega$ is the bandwidth and ω_{nat} is the frequency of the resonance peak [39]. The bandwidth of resonance is defined as the frequency range where the energy dissipated per cycle is greater than half the maximum value, which turns out to be approximately 70.7% of the peak amplitude [39]. The limiting frequencies for this range are called half-power points and the bandwidth is approximately,

$$\Delta\omega \approx 2\xi\omega_{nat} \tag{5.17}$$

for the case of lightly damped systems, which is true for most real systems [39]. As a result, the damping ratio can be approximated by,

$$\xi \approx \frac{\Delta\omega}{2\omega_{nat}} \tag{5.18}$$

This result can be easily applied to experimental data to get a reasonable estimate of the damping ratio of the system.

5.2.3 Log Decrement

An alternative assessment is to use the time domain data by implementing the log decrement approach to measure the damping. Given the simple mass-spring-damper model, it is possible to solve for the damping ratio from the amplitudes of the peaks of the oscillations in the time domain. The natural log of the ratio of successive maxima is defined as the log decrement δ_L,

$$\delta_L = \ln\left(\frac{A_j}{A_{j+1}}\right) \tag{5.19}$$

where the maxima are defined as,

$$A_j = x(t_j) \tag{5.20}$$

For greater accuracy, the maxima after a number of cycles, N, can be compared instead,

$$\delta_N = \frac{1}{N}\ln\left(\frac{A_j}{A_{j+N}}\right) \tag{5.21}$$

The result for an underdamped system is that the log decrement is purely a function of the damping ratio [39],

$$\xi = \frac{\delta_N}{\sqrt{4\pi^2 + \delta_N^2}} \tag{5.22}$$

5.3 Instantaneous Frequency

Since, for a typical vibration signal, the signal strength decays with time and it has been shown that resonance frequency changes as a function of excitation amplitude, it is conceivable that a frequency shift will also occur when a time-frequency analysis is done on a single impact signal. This section describes several techniques employed for this investigation. The results are presented in Appendix B since these techniques did not prove to convey meaningful information.

5.3.1 Phase Change

Usually the instantaneous frequency is described as the derivative of the phase of an analytic signal [41]. More accurately, the derivative of the phase describes the average of the frequencies at a particular time. Using this description, a sampled signal can be analyzed for instantaneous frequency with the approximation,

$$f_i = \frac{\varphi[H\{x(t_2)\}] - \varphi[H\{x(t_1)\}]}{t_2 - t_1} \tag{5.23}$$

However, the results show that there are issues with the instantaneous frequency when the signal is not symmetric about the time-axis, which are addressed in the Appendix.

5.3.2 Short Time Fourier Transform (STFT)

The instantaneous frequency can also be calculated using a short time Fourier Transform. This method uses windows to isolate a signal at a specific time such that the signal becomes,

$$x_t(\tau) = x(\tau)w(\tau - t) \tag{5.24}$$

where $w(t)$ is the window function. The Fourier transform then becomes,

$$X(f) = \int_{-\infty}^{\infty} x_t(\tau) \exp(-j2\pi f\tau) d\tau \tag{5.25}$$

and the discrete Fourier transform is given by [45],

$$X_{DFT}[n, \lambda) = \sum_{m=-\infty}^{\infty} x[n+m] w[m] \exp[-j\lambda m] \tag{5.26}$$

where λ is the continuous frequency variable. An issue with this technique is the tradeoff between resolution in time and resolution in frequency. The STFT can be used to create a spectrogram which plots the frequency variable against the time variable where amplitude is shown by a color map. It is not possible to achieve both very high resolution in time and frequency simultaneously. As the window length is reduced frequency resolution decreases but time resolution increases [45]. Therefore, if the signal changes quickly with both time and frequency, it can be difficult to extract any useful information. This happens to be the case for the signals encountered in this research and the results are presented in Appendix B.

CHAPTER 6

NONLINEAR MEASUREMENT TECHNIQUES

6.1 NRUS Test Setup

In the initial stages of the research the nonlinear resonance ultrasonic spectroscopy (NRUS) method was considered. The initial set of measurements used the NRUS method for nonlinear parameter measurements. A representative schematic of the NRUS test setup is shown in Figure 6.1 and the physical test setup is shown in Figure 6.2.

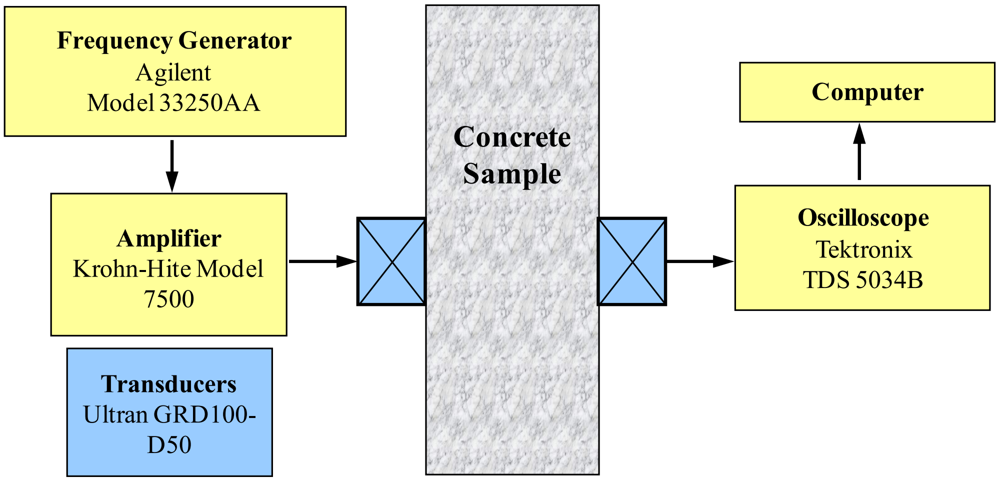

Figure 6.1. NRUS setup schematic.

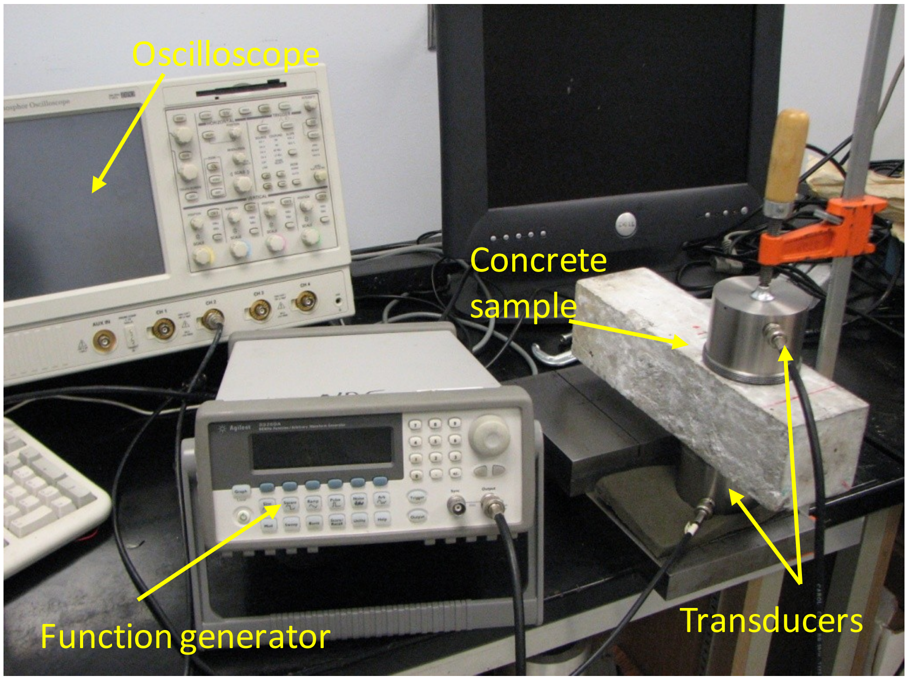

Figure 6.2. NRUS test setup.

In this technique, a function generator (Agilent 33250A) is used to create a sinusoidal input signal with 10 second duration. The sinusoidal signal is swept in frequency in a user specified range around an expected resonance frequency of the sample. The input signal is fed through an amplifier and then transmitted through an ultrasonic longitudinal transducer (Ultran GRD100-D50) to the concrete sample. The transmitted signal is then received by an identical ultrasonic transducer connected to an oscilloscope (Tektronix TDS 5034B) and sampled at 125 kSa/s. In addition, vacuum grease is used on the surfaces of both transducers to improve the transmission and reception of the signal. To ensure the same contact force during the measurement each time, the transducers are clamped to the sample. Data recorded using the oscilloscope is then analyzed using a developed analysis code (based on the software package Matlab®) on a computer.

With this setup, the first compressional wave resonance mode is excited, which can be calculated using the measured compressional wave speed (or the time of flight). Time of flight can be measured using a single transducer which sends a compressional wave through the thickness of the specimen. The time it takes for the signal to travel to the specimen boundary and reflect back to the source is the time of flight, t. Assuming a free surface boundary, the linear resonance frequency is given by [19],

$$f_0 = \frac{v}{2L} = \frac{1}{2t} \tag{6.1}$$

where

L = specimen thickness in direction of wave propagation, meters;

v = wave speed, $\frac{m}{s}$;

t = time of flight, seconds;

However, due to the attenuation in the relatively large CPT specimens, there is no clear reflection of the source wave. Alternatively, two transducers are used and the time of arrival of the signal at the receiving transmitter is used to measure the first compressional resonance frequency,

$$f_0 = \frac{v}{L} = \frac{1}{t_0} \tag{6.2}$$

where

t_0 = time of arrival at receiving transducer, seconds;

Using the time of arrival, the resonance frequency was determined to be around 23-35 kHz for the concrete samples of varied mixture design, but when the frequency sweep was performed in this range there was no clear peak in signal amplitude as expected for resonance. In other words, when a sinusoid at constant amplitude (voltage) is used as an input and the frequency is increased, the output amplitude is expected to increase when the input frequency matches the resonance frequency. Since there was no clear response amplitude increase in the calculated region of interest, the frequency was progressively increased until a significant increase in output signal amplitude was detected. The frequency at the observed amplitude increase was assumed to correspond to the first compressional resonance mode. The frequency sweep was then set to the range around this frequency and the input voltage was progressively increased from about 10 to 190 volts (all the measured data falls in this range but the same voltages are not used for different specimens). The signal in the time domain was then analyzed with a fast Fourier transform (FFT) to obtain the frequency spectrum.

6.1.1 Preliminary NRUS Results

Nonlinear acoustic test setups were developed and evaluated using three existing concrete prism samples subjected to ASTM C 1293 testing. These samples were exposed to the test environment for two years, and the testing for these specimens had already been concluded before the start of this project. All of these concrete samples contained highly reactive sand from El Paso, TX (Jobe), blended with varying supplementary cementing materials, as shown in Table 6.1. The expansion plot from that project is also shown in Figure 6.3.

Table 6.1. Mix Designs and expansions for Jobe concrete prism samples.

	Mix Design	ASTM C 1293 2-Year Expansion (%)
ASR1	No SCMs	0.543
ASR2	8% metakaolin	0.048
ASR6	25% Class C fly ash	0.347

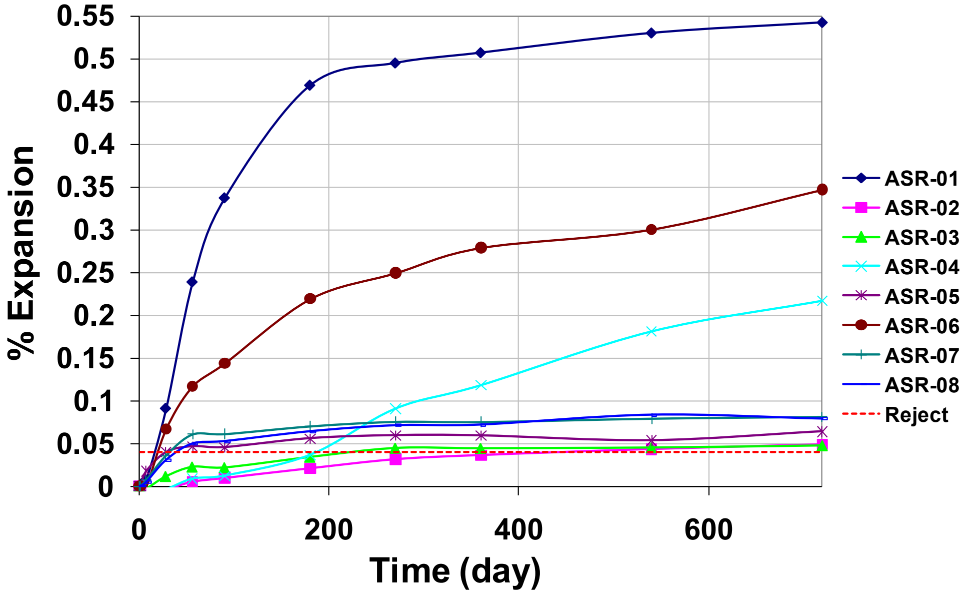

Figure 6.3. Expansions of Jobe samples from previous project.

The results of the FFT analysis for ASR1, ASR2, and ASR6 are shown in Figure 6.4, Figure 6.5, and Figure 6.6, respectively. The amplitude in the frequency domain is representative of the signal amplitude, in volts, at a given frequency. The frequency at which the largest magnitude is measured is then assumed to be the resonance frequency.

The resonance frequency at the lowest excitation is assumed to be the linear resonance frequency, f_0. The left hand side of Eq. (4.3) is then calculated by taking the difference between the linear resonance frequency and the frequency at the current excitation level, as shown in Figure 6.4.

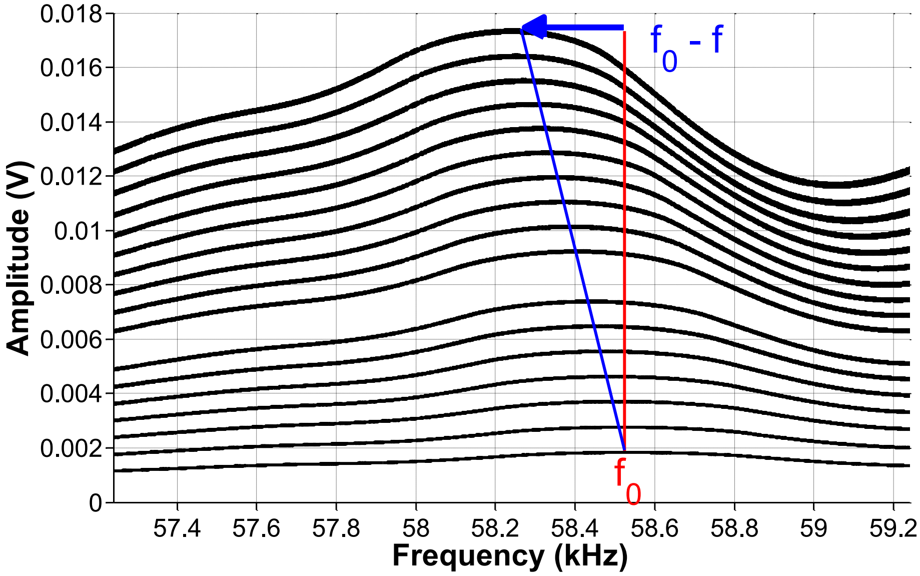

Figure 6.4. FFT for ASR1 sample using NRUS.

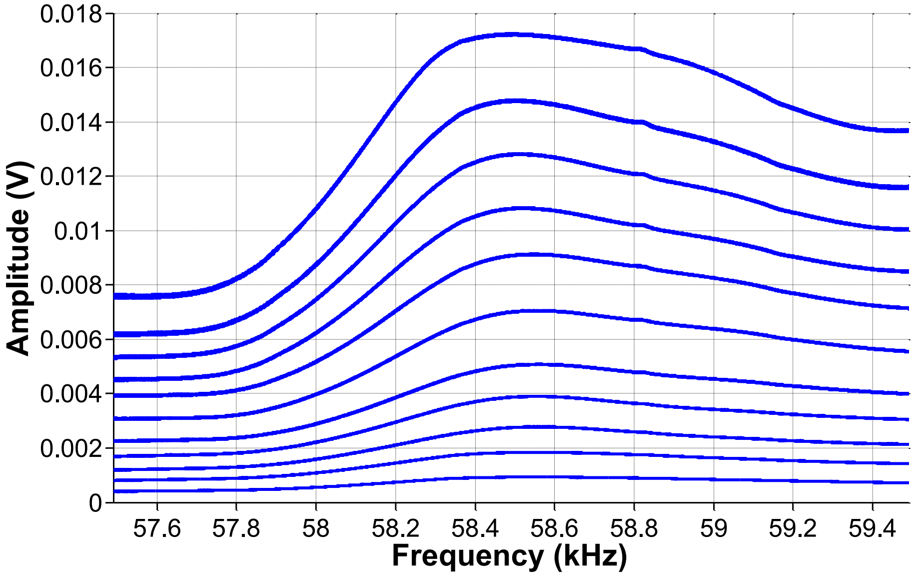

Figure 6.5. FFT for ASR2 sample using NRUS.

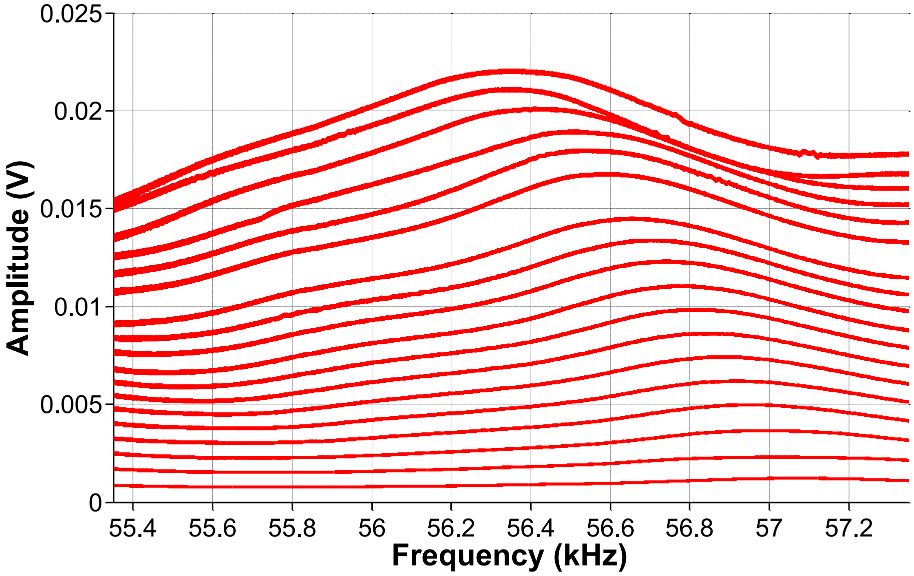

Figure 6.6. FFT for ASR6 sample using NRUS.

The calculated difference, $f_0 - f$, is then normalized by the linear resonance frequency and plotted against amplitude, as shown in Figure 6.7. The nonlinear parameter, η, is then the slope of the data as dictated by Eq. (4.3) and illustrated in Figure 6.7. This way a positive nonlinearity parameter represents a decrease in frequency with increased excitation.

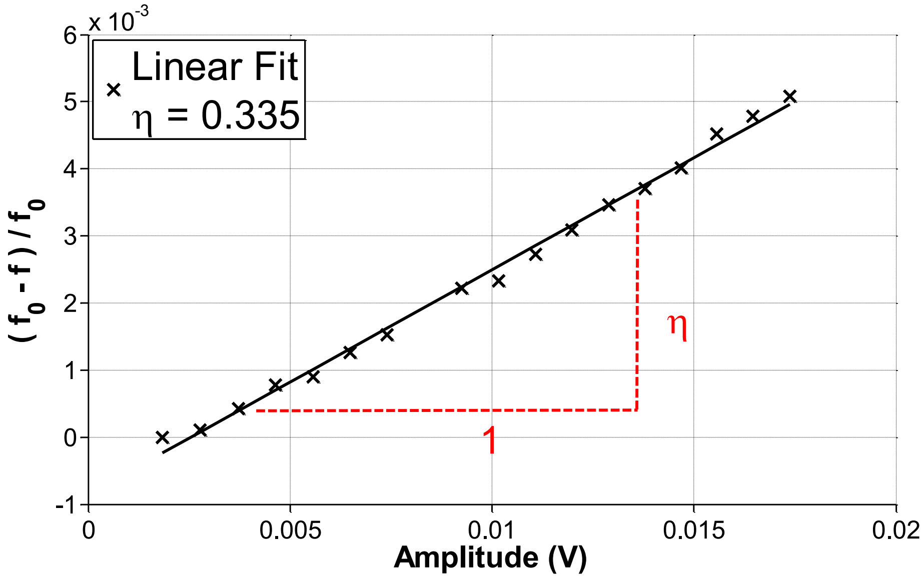

Figure 6.7. Results of frequency sweep for ASR1 (NRUS).

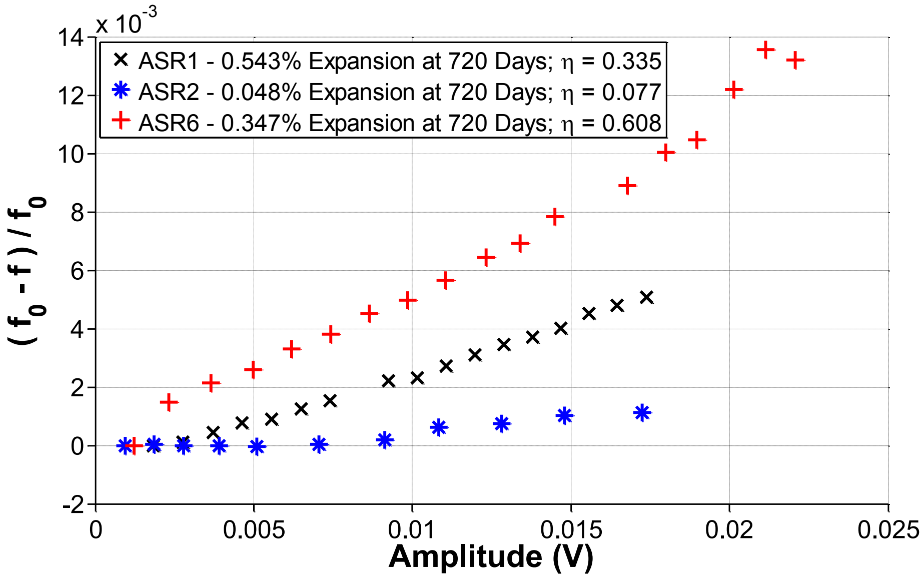

Figure 6.8. Results of frequency sweep with increasing voltage (NRUS).

Figure 6.8 presents the results for the three specimens tested together along with the expansion recorded at 720 days and current nonlinearity. Using the nonlinear parameter, each sample is clearly differentiated, showing distinguishable nonlinearity levels. Surprisingly, compared to the expansion values last recorded at 720 days, there is a discrepancy. The ASR1 sample had more expansion at 720 days compared to ASR6, but the measured ASR6 nonlinearity is higher. However, even though both ASR1 and ASR6 were well beyond the 0.04% expansion limit at 2 years of CPT, it is not clear how any further development of damage has progressed in the samples over this last year of ambient storage. Therefore, a comparison of expansion values from the end of the CPT test to current nonlinearity is not valid and the results only show the ability of the method to distinguish among the samples.

6.1.2 Limitations of NRUS

While this method distinguished between the different concrete mixtures, the peak assumed to be a resonance mode had a higher frequency than what was expected based on time of flight measurements. This local peak could not be confirmed to correspond to resonance frequencies or their harmonics. Since it is unclear where this local peak in the frequency domain originated from, there is a question of robustness and reliability of the technique. In addition, there were difficulties with consistency in the measurements, as illustrated in Figure 6.9. Measurements for the ASR2 sample were repeated by reassembling the setup between measurements. Between each measurement trial, the transducers were removed from the specimen, the specimen and transducers were cleaned, and the specimen was again coupled to the transducers using vacuum grease. It was found that the results were not consistent when the setup was reassembled, producing considerable scatter. It is speculated that this can result from changes in the boundary (transducer to sample coupling) conditions caused by reassembling the test setup.

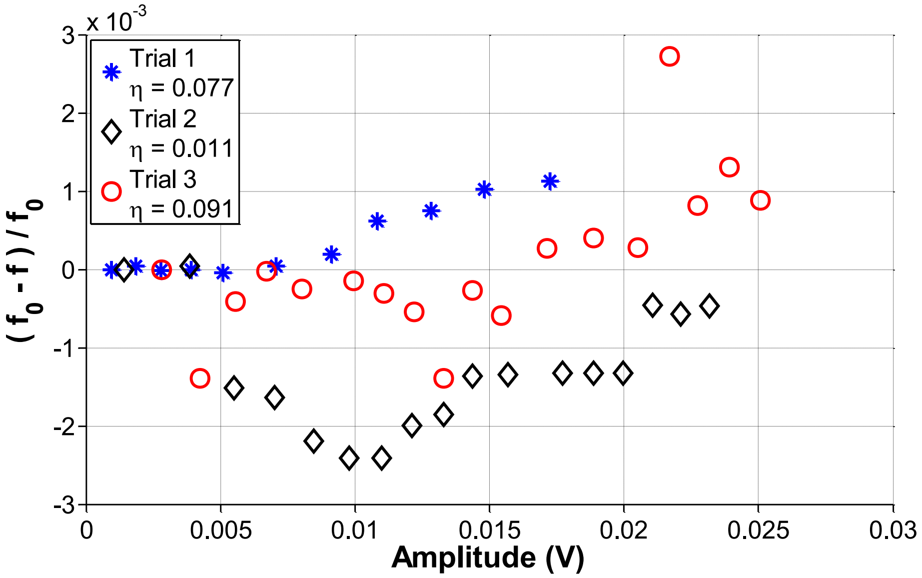

Figure 6.9. Frequency shift variation for ASR2 sample using NRUS.

6.2 NIRAS Test Setup

Due to inconsistent results and unanswered questions with the NRUS technique, an alternate method of excitation was attempted. The new technique uses the natural vibration of the specimen as the probing signal and is termed nonlinear impact resonance acoustic spectroscopy (NIRAS), first introduced by Chen et al. [26]. Instead of a frequency sweep using transducers in ultrasonic frequency range, the sample is excited with a low amplitude impact. The setup is similar to the ASTM C 215 procedure for the measurement of the transverse resonance frequency [46]. The specimen is placed on a 38 *mm* (1.5 *in*) thick support mat to allow free vibration. A 5 oz. hammer is used to strike the sample at its center, as shown in Figure 6.10. An accelerometer (PCB 353B13) is attached using super glue to one end of the specimen, at the center, where the response is at a maximum for the transverse mode. The sample is tested one minute after the attachment of the accelerometer and the signal is then captured using a Tektronix TDS5034B oscilloscope and analyzed using Matlab ®. The schematic for this setup is shown in Figure 6.11. The signal duration captured by the oscilloscope is 0.4 seconds, which allows a complete decay of the response signal, with a sampling rate of 500 kSa/s. The signal is then "zero-padded" and analyzed in Matlab using the fast Fourier transform. The "zero-padding" increases the signal duration by appending trailing zeros at the end of the signal. This increases the apparent resolution in the frequency domain allowing more accurate identification of the resonance peak frequency. The signal processing for both NRUS and NIRAS techniques is essentially the same and both rely on the same nonlinear resonance theory. However, as will be demonstrated throughout the chapter, the NIRAS technique turns out to be much more repeatable and robust and considerably easier to implement.

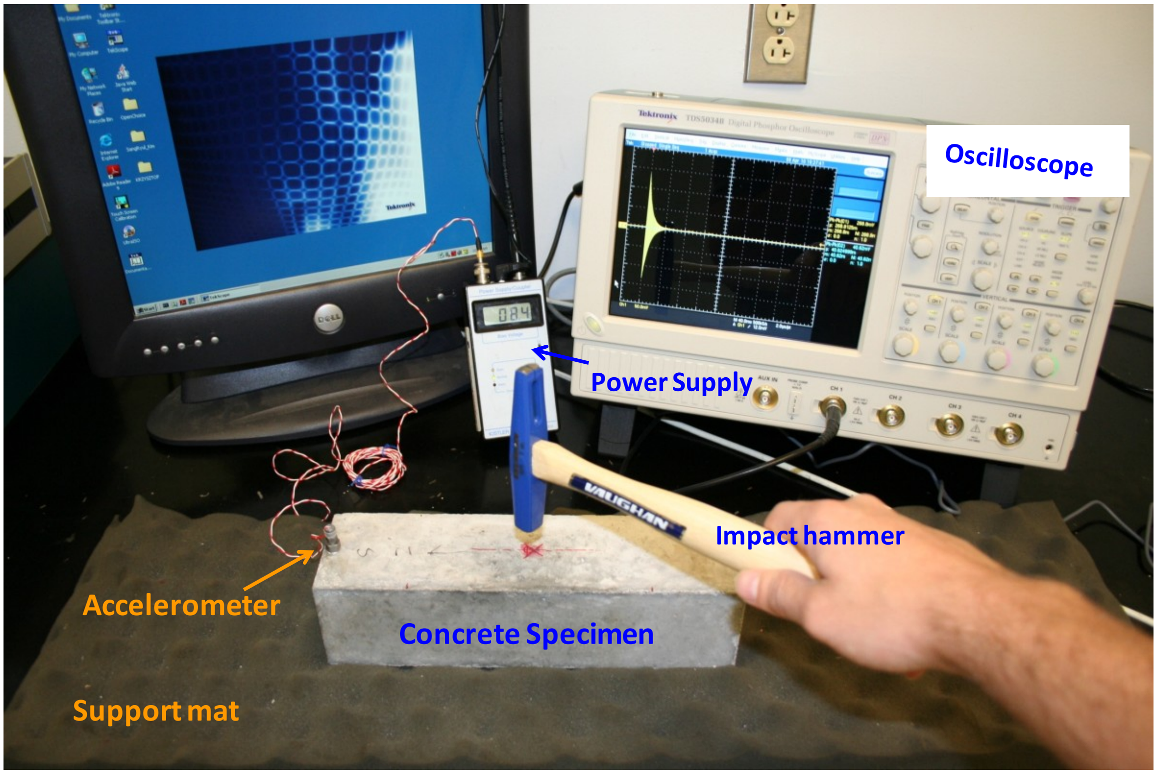

Figure 6.10. NIRAS test setup.

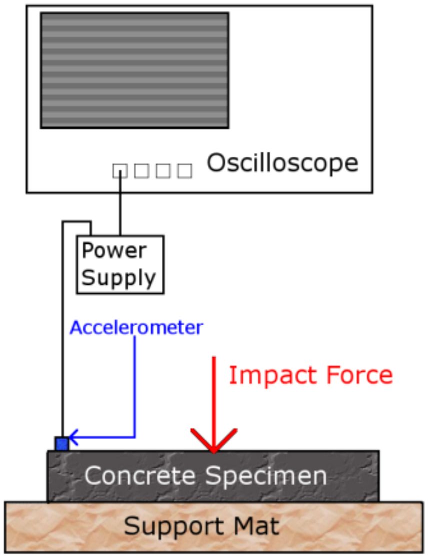

Figure 6.11. NIRAS setup schematic.

6.2.1 Preliminary NIRAS Results

The NIRAS technique was also initially applied to the Jobe samples (Table 6.1) to test the setup. The impact excites the specimen's natural vibration. The typical signal captured by the accelerometer is shown in Figure 6.12 in both the time and frequency domain (for ASR1 in this case). Notice that the signal is a simple decaying oscillation.

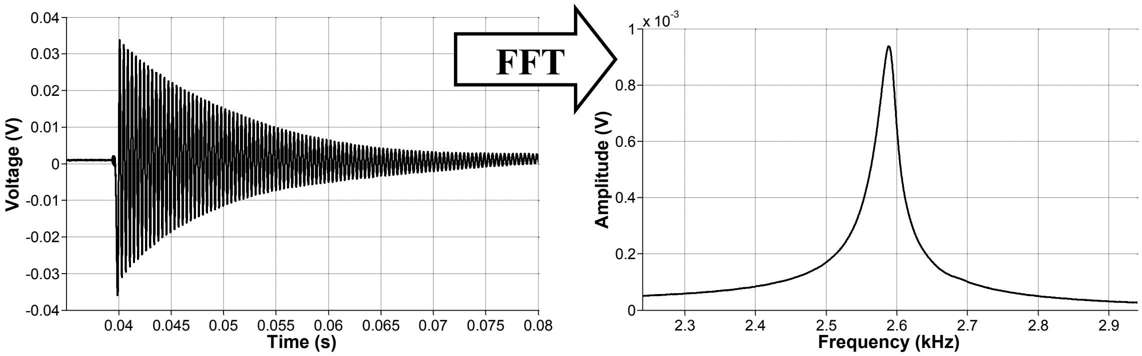

Figure 6.12. Typical NIRAS signal in time and frequency domain.

Figure 6.12 shows that the captured signal has a high signal to noise ratio and the one-sided frequency spectrum has a clearly defined resonance peak. The high signal to noise ratio (SNR) can be seen in time domain signal, which has significantly higher amplitude than the noise before the impact (before 0.04 seconds).

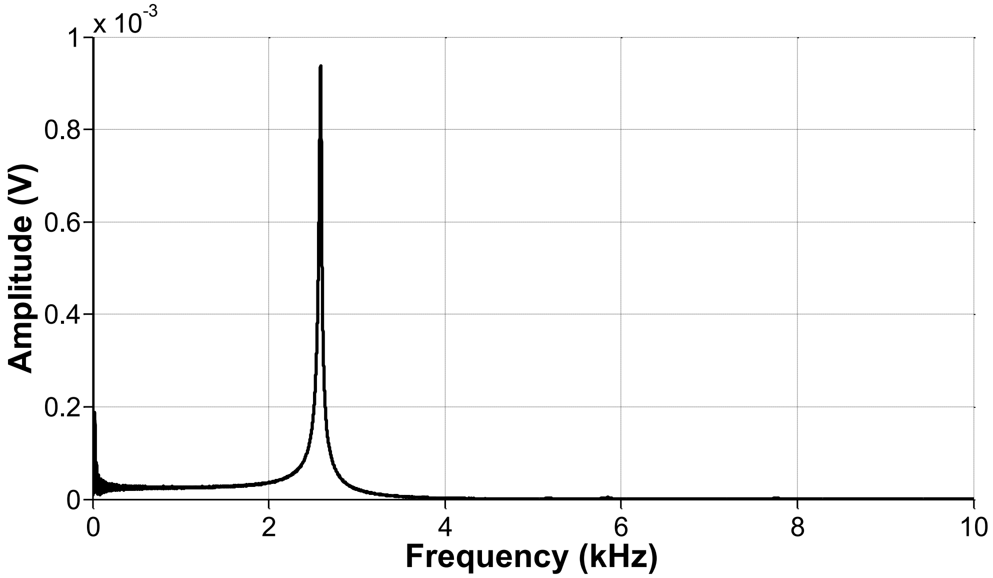

Figure 6.13. One-sided spectrum for recorded acceleration signal.

Figure 6.13 shows a larger portion of the spectrum, demonstrating that the fundamental resonance mode is the only mode exited with this technique. The spectrum is shown up to 10 kHz since this is the maximum frequency that can be excited with the impact hammer. There is some low frequency content at the beginning of the signal which can be induced by the vibration of the support or equipment near the testing area. However, these low frequencies will not affect the results since the resonance occurs at considerably higher frequencies. For testing of nonlinearity, the procedure is repeated 10 times, with progressive increases in the strength of the impact. The result for ASR 1 is shown in Figure 6.14. Just as in the NRUS measurements, the lowest amplitude resonance frequency is assumed to be the linear resonance frequency, f_0. The difference between this linear resonance frequency and the frequency at a higher amplitude impact, $f_0 - f$, is normalized by the linear frequency and plotted against the recorded signal amplitude in Figure 6.15. A linear fit is used for the data in this plot to find the nonlinearity parameter, which is simply the slope. The results, in the frequency domain, for applying the technique to ASR2 and ASR6 samples are also shown in Figure 6.16 and Figure 6.17, respectively.

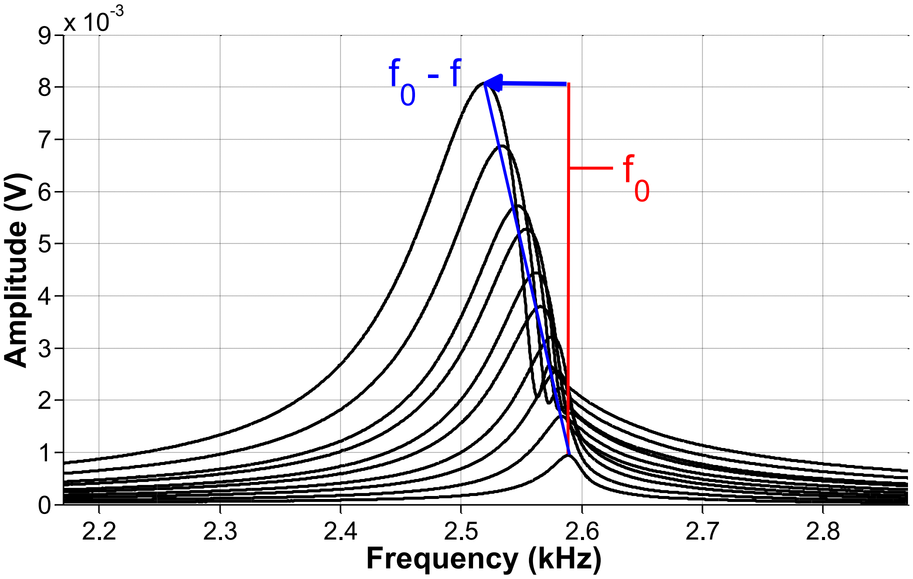

Figure 6.14. FFT for ASR1 sample using NIRAS.

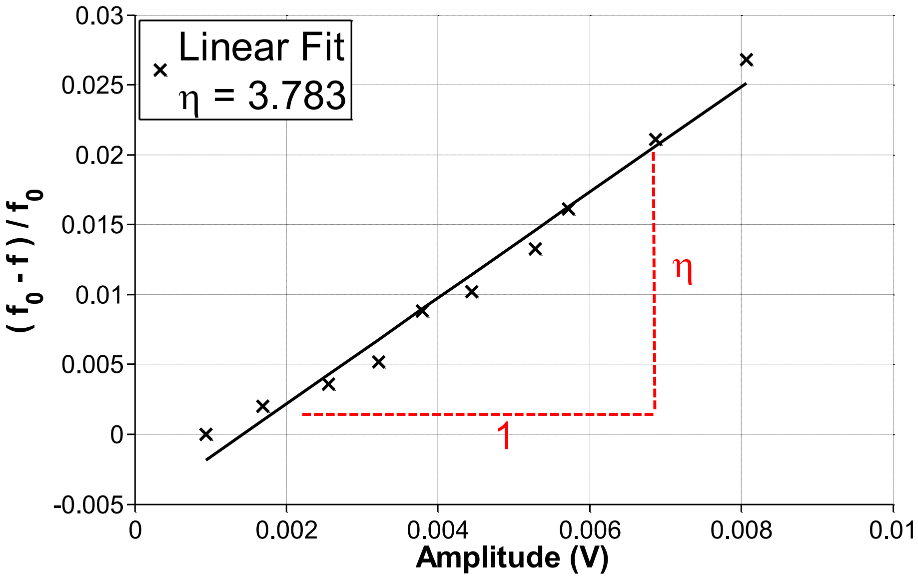

Figure 6.15. Normalized frequency vs. amplitude for ASR1 sample.

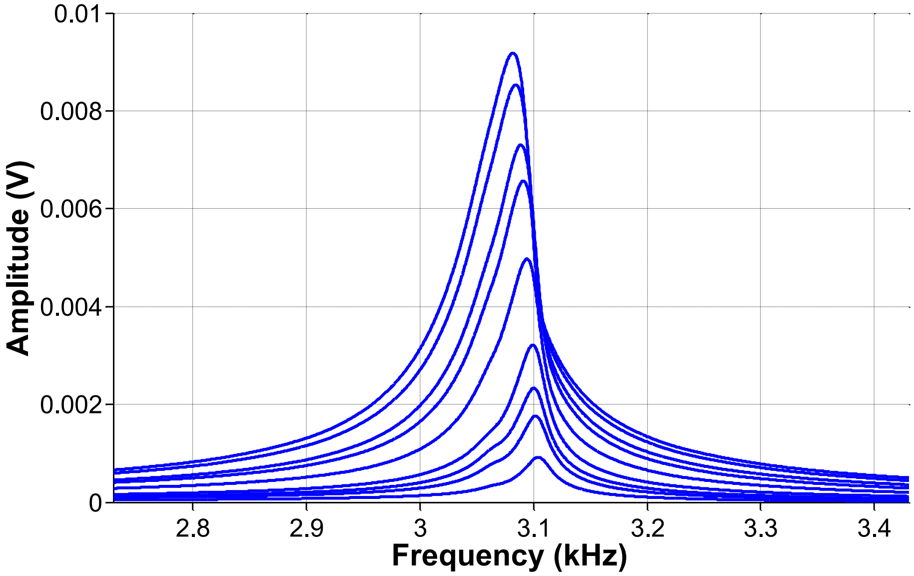

Figure 6.16. FFT for ASR2 sample using NIRAS.

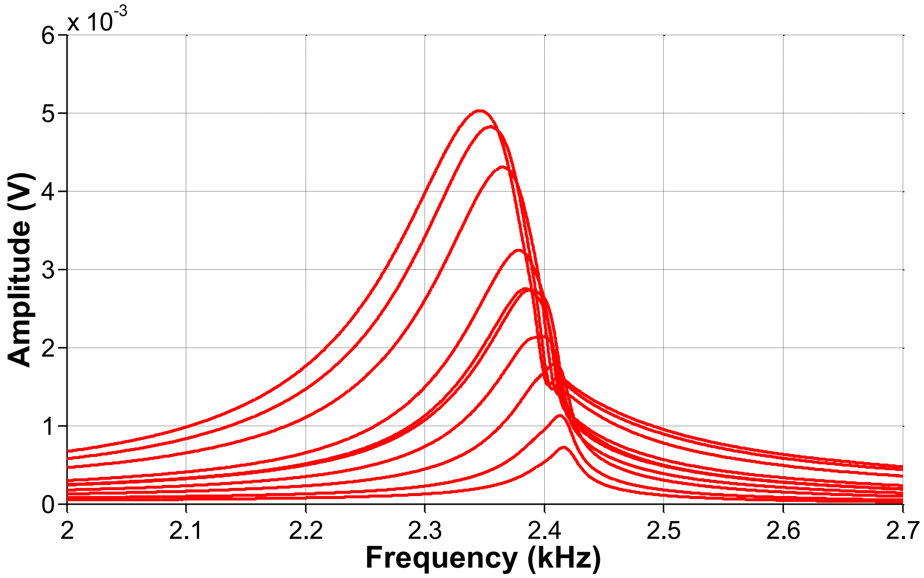

Figure 6.17. FFT for ASR6 sample using NIRAS.

The normalized frequency is plotted against amplitude for all three samples in Figure 6.18. These results show that the sample with the least expansion, ASR2, is well-differentiated from the more expansive mixes. However, once again, contrary to expansion results, the results from both the NRUS and NIRAS techniques suggest that the ASR6 sample is more damaged than ASR1, since the nonlinearity of ASR6 is larger. However, as previously mentioned, the comparison may not be valid since the samples have been in ambient storage for over a year but both nonlinear methods are qualitatively the same.

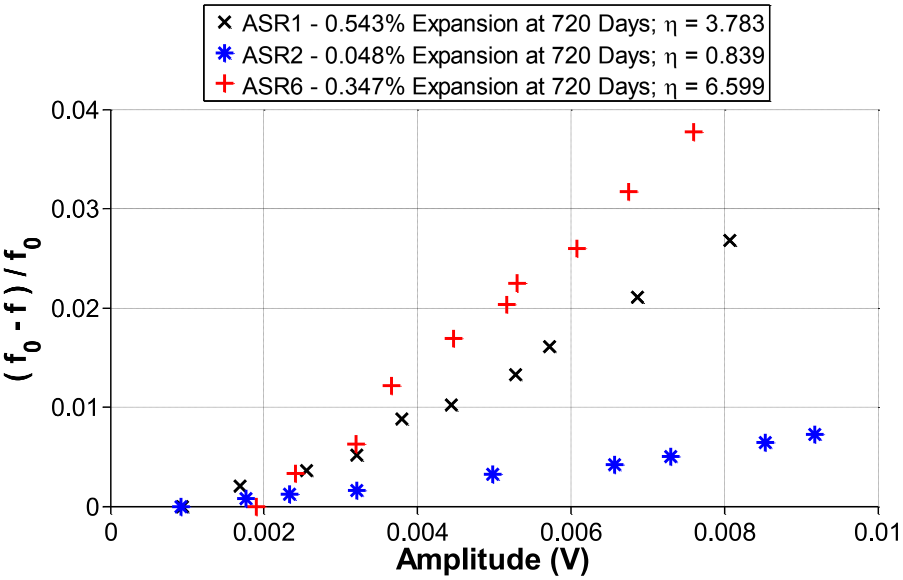

Figure 6.18. Normalized frequency shift vs. amplitude for Jobe samples using NIRAS.

6.2.2 Validation of NIRAS Test Setup

In order to ensure that the measured nonlinearity is solely due to the material behavior, the linearity of the entire experimental measurement setup, which includes a few electronic devices, was confirmed using a linear elastic aluminum (alloy 6061) prism. This prism is of similar dimensions, $76.3\,mm \times 76.3\,mm \times 304\,mm$ $(3\,in \times 3\,in \times 12\,in)$, to the concrete samples. The results in Figure 6.19 and Figure 6.20 clearly illustrate that for an undamaged and isotropic sample, there is no detectable change in the resonance frequency. This also shows that there are no spurious nonlinear effects from the instrumentation. Also, note that resonance peak for aluminum is significantly sharper than broad peaks recorded for concrete due to lower attenuation. Additionally, due to the lower attenuation, the natural vibration takes longer to decay so the window was extended to 2 seconds with a 250 kSa/s sampling rate.

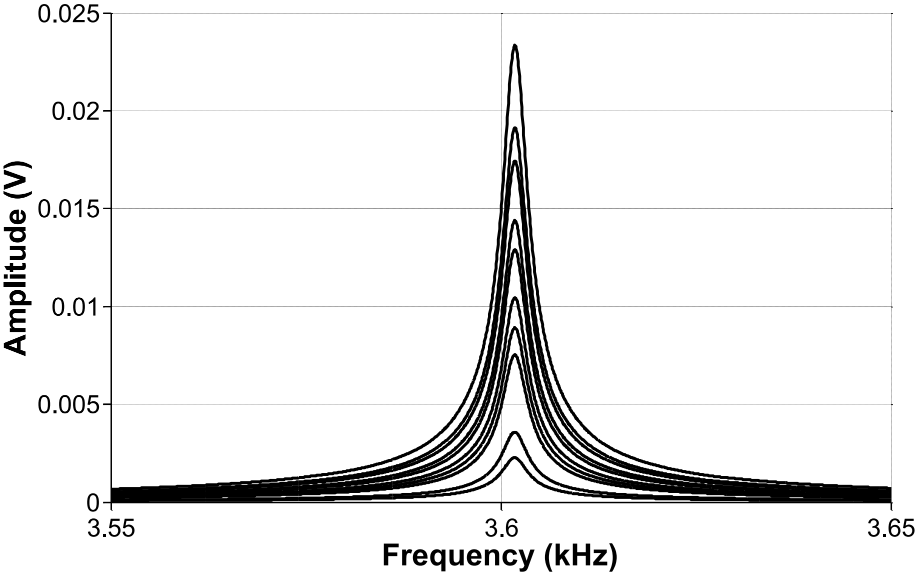

Figure 6.19. FFT for aluminum sample.

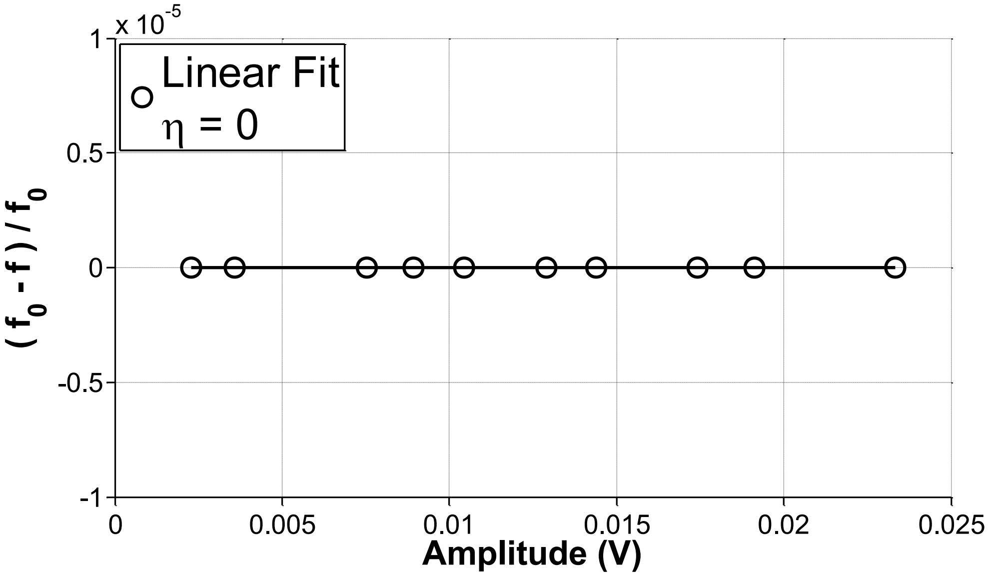

Figure 6.20. Normalized frequency shift vs. amplitude for aluminum sample.

In order to confirm the resonance peak measurements done by the impact testing method, the equation provided in ASTM E 1876 [47] was used to calculate the modulus of elasticity with the measured resonance frequency:

$$E = 0.9465\left(\frac{mf_f^{\,2}}{b}\right)\left(\frac{L}{t}\right)^3 T_1 \tag{6.3}$$

where

E = Young's modulus of elasticity, Pa ;

m = mass of the bar, g ;

b = width of bar, mm ;

L = length of bar, mm ;

t = thickness of bar, mm ;

f_f = fundamental resonant frequency of bar in flexure, Hz ;

T_1 = correction factor for fundamental flexural mode given by:

$$T_1 = 1 + 6.585\left(1 + 0.0752\mu + 0.8109\mu^2\right)\left(\frac{t}{L}\right)^2 - 0.868\left(\frac{t}{L}\right)^4 - \left[\frac{8.340\left(1 + 0.2023\mu + 2.173\mu^2\right)\left(\frac{t}{L}\right)^4}{1 + 6.338\left(1 + 0.1408\mu + 1.536\mu^2\right)\left(\frac{t}{L}\right)^2}\right] \tag{6.4}$$

where μ is Poisson's ratio.

These calculations were performed for aluminum, where the modulus of elasticity is well known to be close to 70 GPa. The calculation with the measured weight and resonance frequency yielded a modulus of elasticity of 69.47 GPa. This result shows the accuracy of determining the resonance frequency of a material with the impact method. Taking 70 GPa as an accepted value yields less than 1% error using the impact testing method. If these calculations are applied to CPT samples, making reasonable assumptions about the Poisson's ratio and dynamic modulus, the calculated resonance frequencies are in the same range as the measured ones. Note that the standard ASTM C 215 has similar equations for calculating the dynamic modulus of elasticity using resonance frequency. The difference between ASTM C 215 and ASTM E 1876 is in the calculation of a correction factor. The correction factor in ASTM C 215 is specific to concrete while the correction factor in ASTM E 1876 is more general and can be used with higher values of Poisson's ratio. In fact, using the properties of the concrete prism, and the correction factor from ASTM E 1876 yields a similar result to following the procedure in ASTM C 215.

6.2.3 Attachment Method for Accelerometer

Alternative attachment techniques have been explored in an effort to improve robustness of the NIRAS technique. Casting a screw attachment into the sample was investigated to test if improvements in consistency could be achieved. The very reactive Las Placitas aggregate was used in this assessment. The casting of the screw attachment was achieved using a bracket, which held the attachment during the casting, as shown in Figure 6.21. The quality of the cast attachment for the three samples varied as shown in Figure 6.22. Consequently the results were also varied. Figure 6.23 shows both the FFT and frequency shift for sample 1 at an early age, where the standard deviation is about 18% from the mean, but for a later age, shown in Figure 6.24, the standard deviation from the mean is only about 2%. Also, note that the accelerometer could not be attached using an adhesive in the same spot as the cast attachment and this can also be a source of variability between the attachment methods.

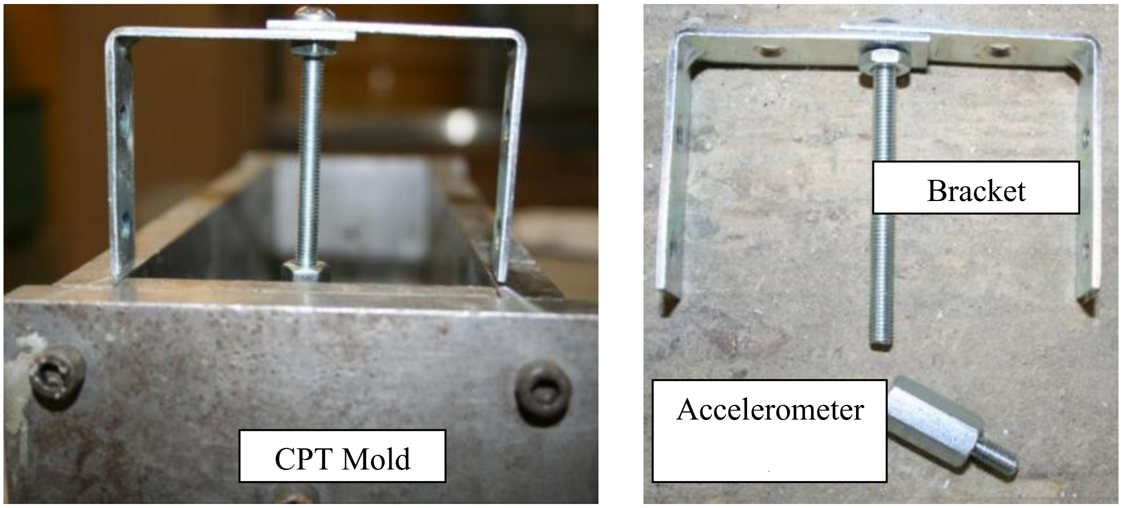

Figure 6.21. Bracket used for casting accelerometer attachment.

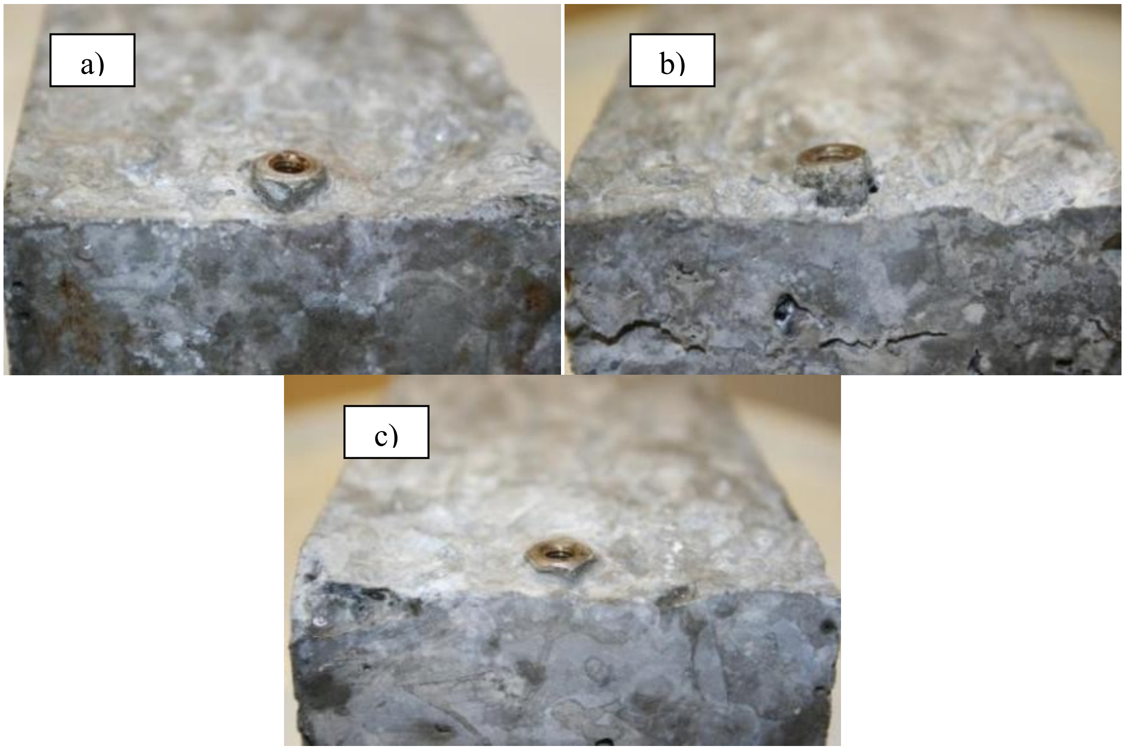

Figure 6.22. Cast accelerometer attachment for a) Sample 1, b) Sample 2, and c) Sample 3.

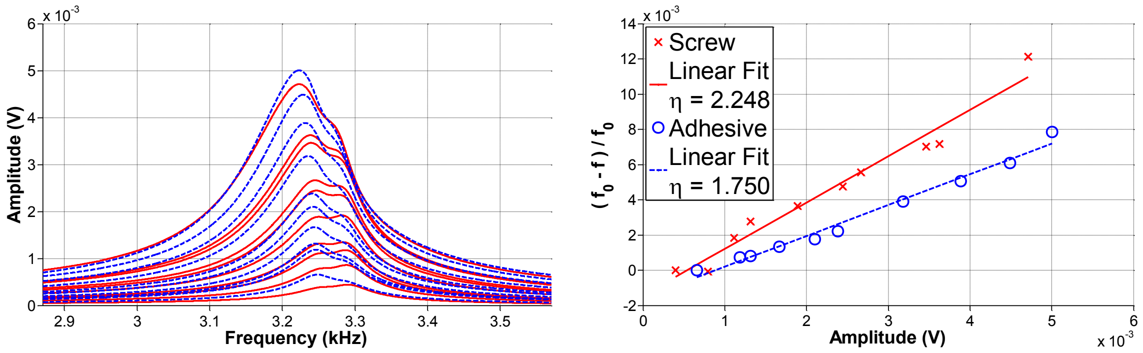

Figure 6.23. FFT and frequency shift for Sample 1 at 23 days.

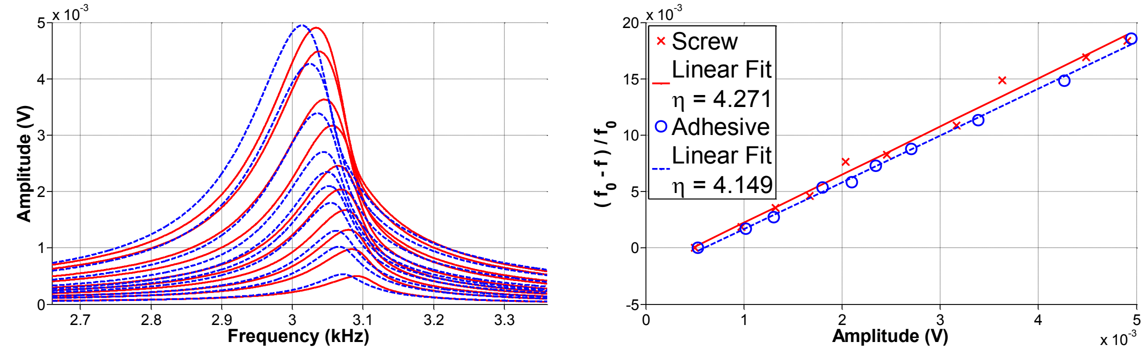

Figure 6.24. FFT and frequency shift for Sample 1 at 30 days.

Since the screw attachment was steel and could also be used as an attachment for a magnet, this coupling technique was also investigated. Figure 6.25, Figure 6.26, and Figure 6.27 show the results at 65 days for all three samples with all three coupling techniques. The standard deviations for Figure 6.25-Figure 6.27 are 27%, 20%, and 20%, respectively.

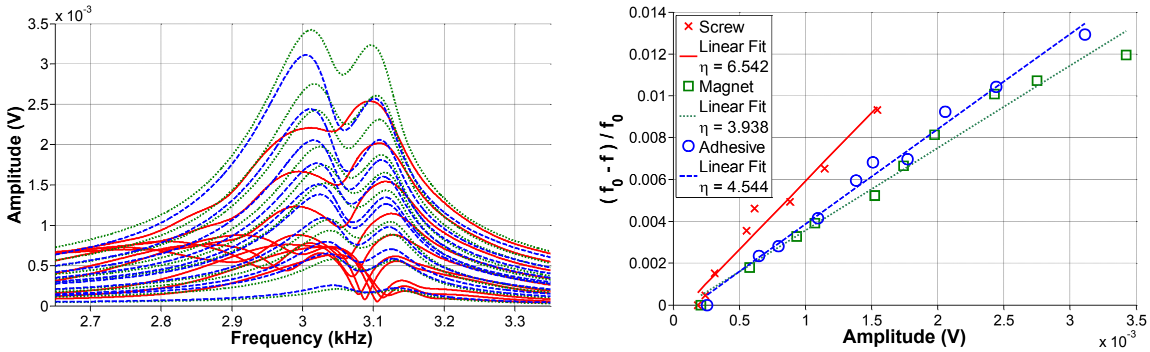

Figure 6.25. FFT and frequency shift for Sample 1 at 65 days.

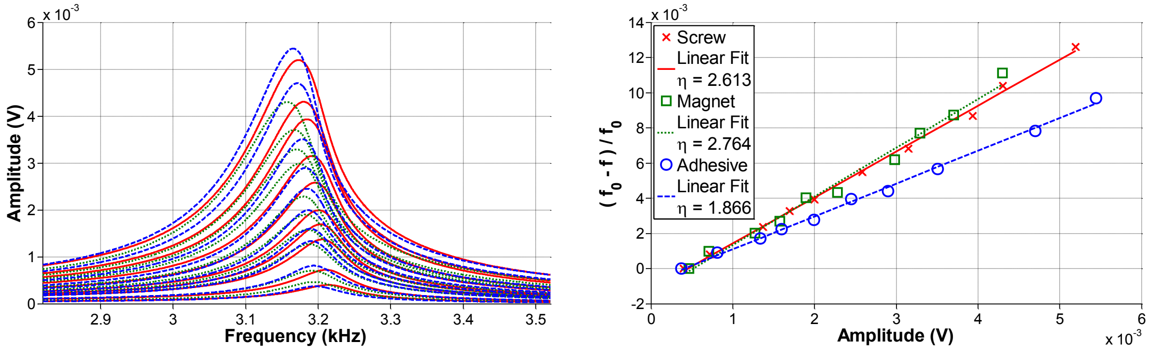

Figure 6.26. FFT and frequency shift for Sample 2 at 65 days.

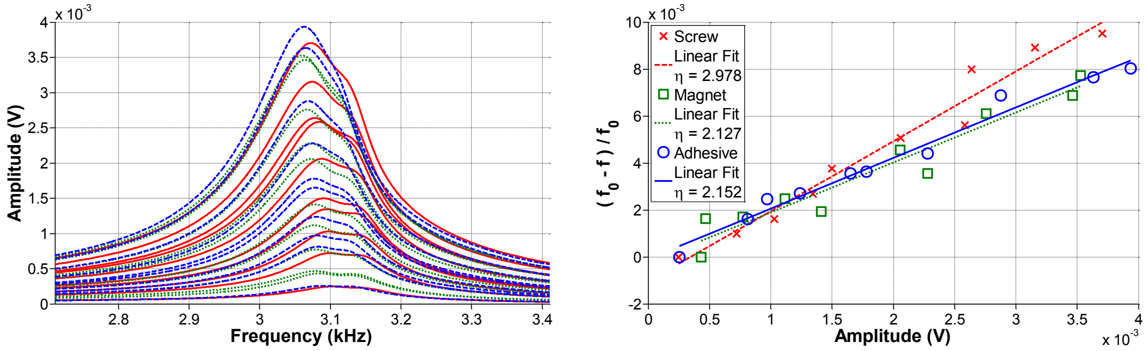

Figure 6.27. FFT and frequency shift for Sample 3 at 65 days.

Based on these results, there does not seem to be an apparent advantage to casting a screw/magnet attachment into the specimens. In fact, looking at Figure 6.25, some irregularities in the FFT signal are noticeable for the screw attachment that are not seen for the magnet or adhesive attachment. Consequently a focus is placed on increasing the robustness of using an adhesive attachment; the adhesive attachment also has the advantage of being a semi-permanent attachment that can be readily applied to concrete cores or other concrete specimens.

6.2.4 Robustness of NIRAS Test Setup

The consistency of the NIRAS setup was tested by repeating measurements on the same sample ten times, each time removing the accelerometer and re-gluing. Each time the slope, which represents nonlinearity, was recorded. The sample tested was one of the Mix 1 reference samples. The result is shown in Figure 6.28, which demonstrates about 10% standard deviation (SD) from the mean nonlinearity (AVG).

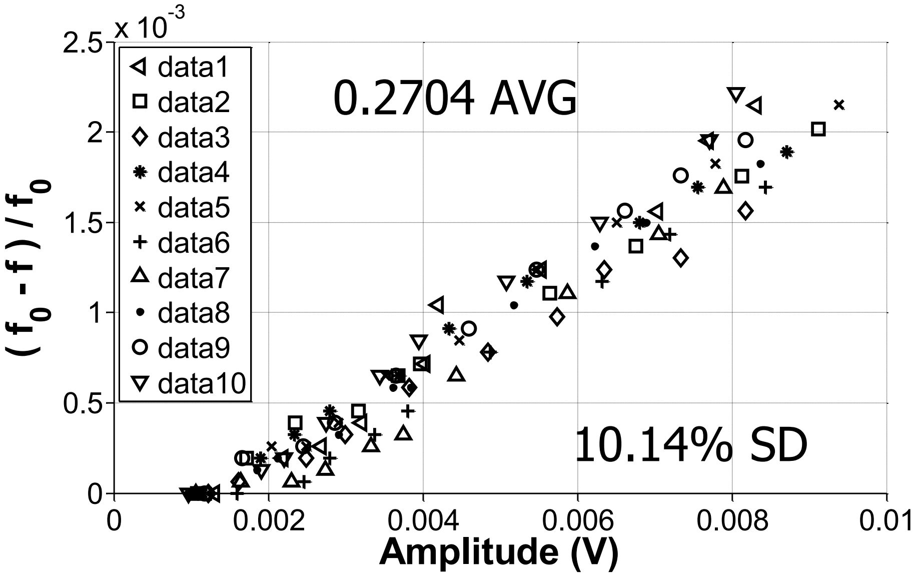

AVG = mean
SD = standard deviation

Figure 6.28. Variability of NIRAS measurements.

This procedure was repeated on a second sample from the Mix 1 reference batch at four positions; a schematic is shown in Figure 6.29. The results for positions 1 and 2 are shown in Figure 6.30 and Figure 6.31 and the results for positions 3 and 4 are shown in Figure 6.32 and Figure 6.33, respectively.

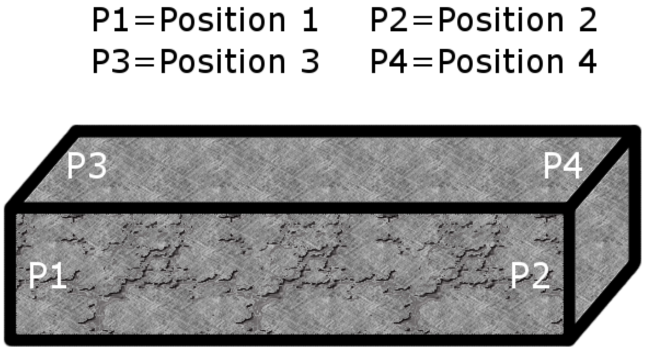

Figure 6.29. Schematic showing tested position.

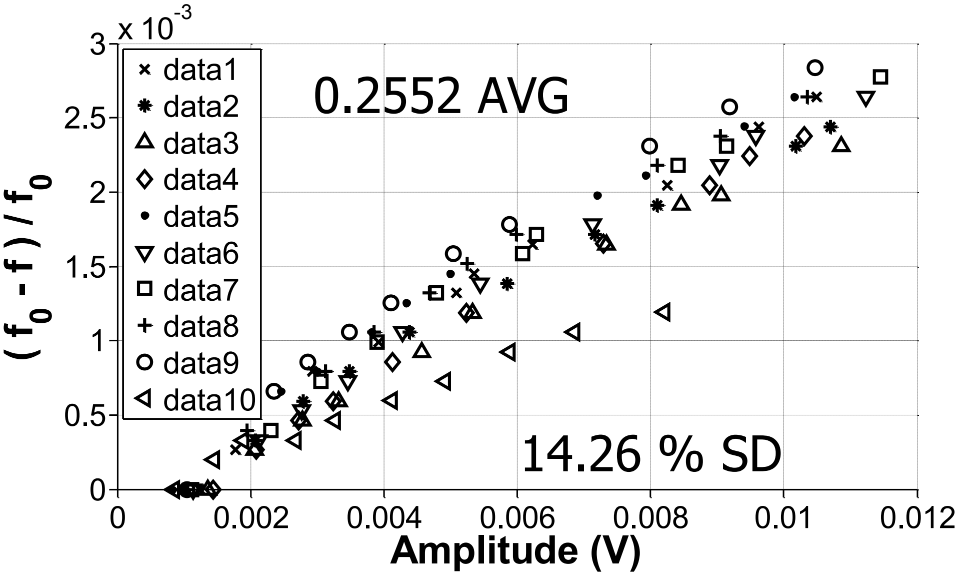

AVG = mean
SD = standard deviation

Figure 6.30. Variability for Position 1.

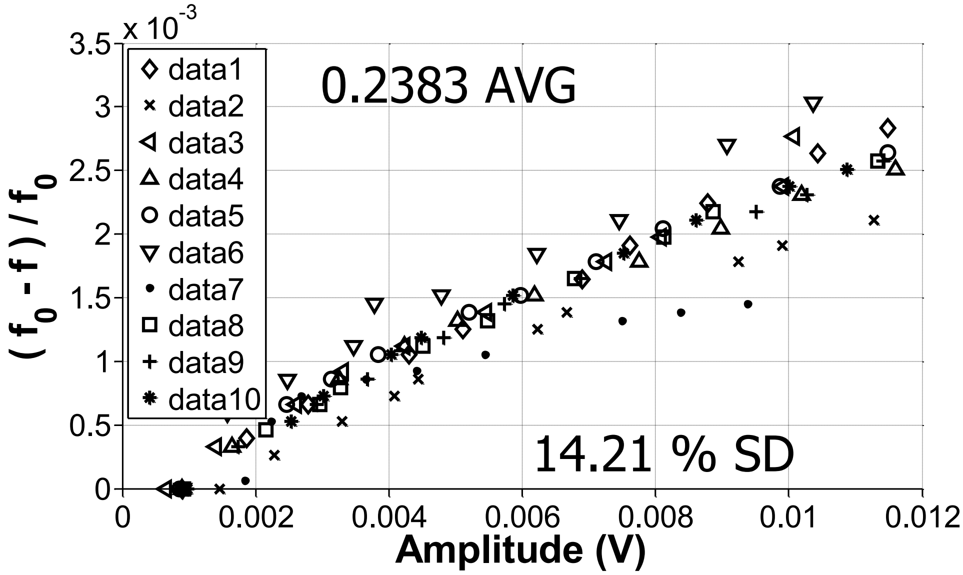

AVG = mean
SD = standard deviation

Figure 6.31. Variability for Position 2.

Note that the mean values for positions 1 and 2 are very close together. This makes sense since these positions are on the same prism surface but at opposite ends, so the same vibration mode is being measured. The standard deviation for these positions is also practically the same. However, this standard deviation is higher than the result of 10% shown in Figure 6.28. This may be due to the fact that these positions had been previously tested very frequently and a debonder for the adhesive was not always used. This resulted in a deteriorated surface at those positions, which may explain the higher standard deviation. Positions 3 and 4 were tested for the first time, so the surface condition was relatively smooth, and the results show a markedly improved standard deviation. Also, as before, the mean value is very close for both positions since they are on the same surface of the prism. The average nonlinearity for the ten data sets for positions 3 and 4 is different from the nonlinearity for positions 1 and 2. This result is expected since the material is not perfectly isotropic. Excitation of a different surface results in the vibration of a different cross-section which can result in the measurement of a different nonlinearity.

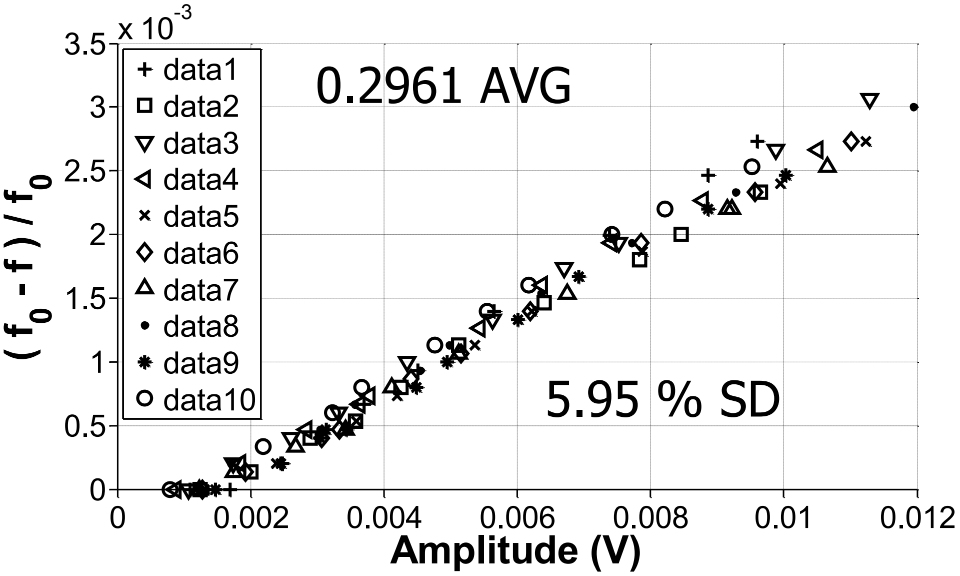

AVG = mean
SD = standard deviation

Figure 6.32. Variability for Position 3.

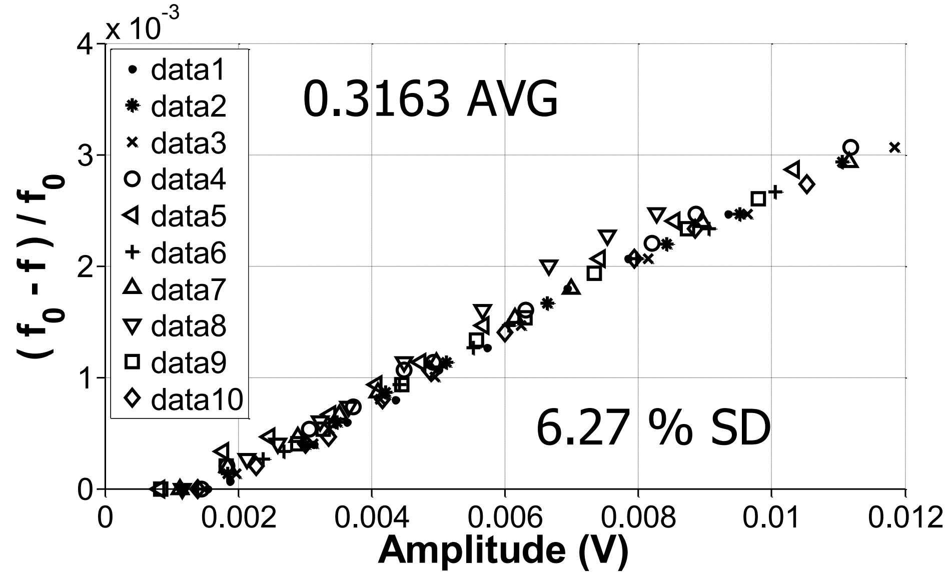

AVG = mean
SD = standard deviation

Figure 6.33. Variability for Position 4.

The samples used for these measurement variability experiments were undamaged samples with relatively low nonlinearity; therefore, a set of measurements was also made on a damaged sample with relatively high nonlinearity. The result, shown in Figure 6.34, is comparable to results for the sample with low nonlinearity.

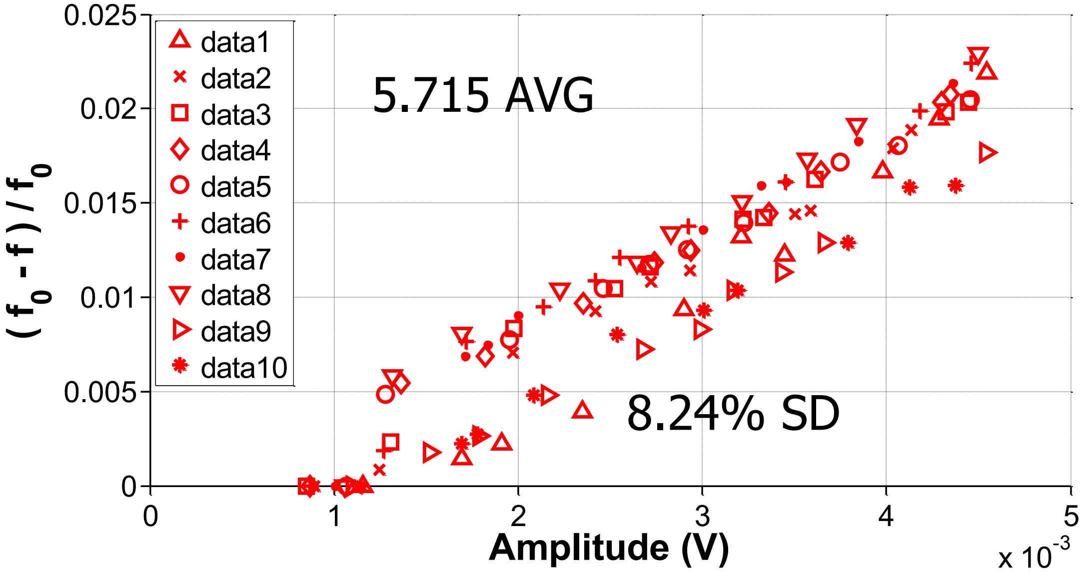

AVG = mean
SD = standard deviation

Figure 6.34. Variability for damaged sample.

6.2.5 Validation of Linear Assumption

As mentioned in the theoretical background, the nonlinear parameter used in this study is extracted by assuming a linear relationship between frequency shift and strain amplitude. This is thought to hold true for low levels of strain amplitude. The question that arises from that assumption concerns the limit to which that statement holds true. This limit was tested on samples with relatively high (ASR6) and low nonlinearity (Reference Mix 4). The results demonstrate that the limit is not the same for both samples. The highly nonlinear sample shown in Figure 6.35 deviates from the linear relation at a relatively low amplitude but there is no deviation for the sample with low nonlinearity, shown in Figure 6.36. Note that both samples were excited to about the same level of impact excitation (roughly the same strength of impact) but the response of a highly nonlinear specimen has lower amplitude than that of one with low nonlinearity due to peak broadening (greater damping). These results demonstrate that for a highly nonlinear sample, the relation between frequency shift and amplitude is linear for amplitudes lower than $5 \times 10^{-3} V$ (This is the magnitude from the FFT). The relation remained linear for all levels of excitation for the sample with low nonlinearity. In all other measurements in this project the impact excitation was kept low enough to avoid a nonlinear relation between frequency shift and amplitude.

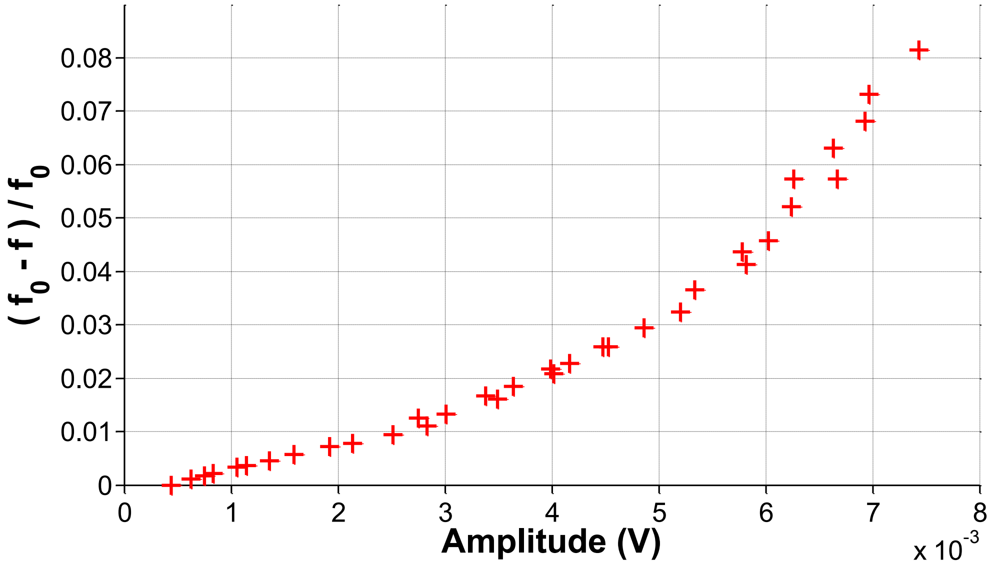

Figure 6.35. Results for higher amplitude excitation for ASR6.

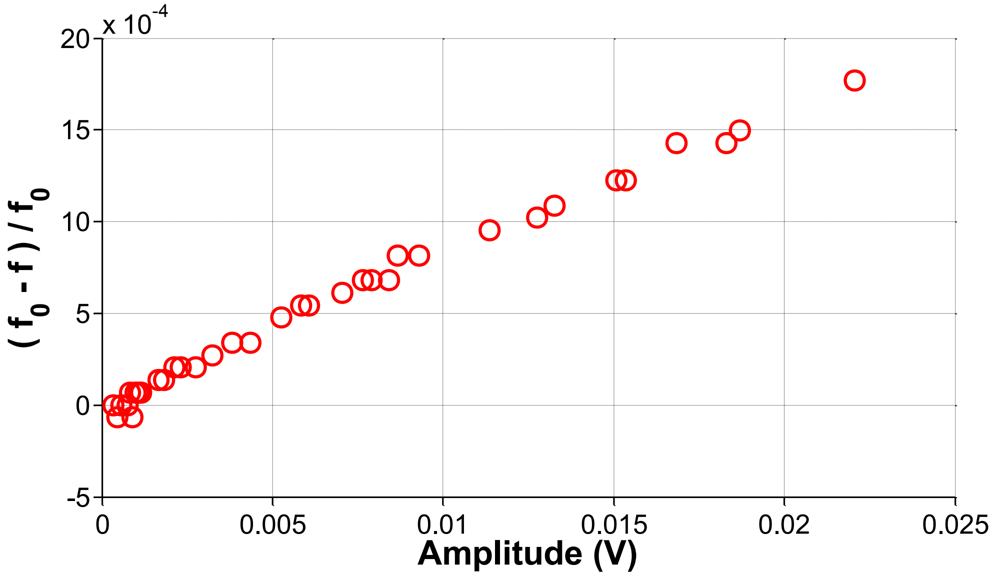

Figure 6.36. Results for higher amplitude excitation for reference Mix 4.

6.3 Setup Summary

Overall, these results show the ability of the nonlinear resonance techniques to distinguish the less damaged sample from the highly damaged samples and suggest the potential of this approach for damage assessment in concrete. Since the results of NIRAS are clear and consistent as well as easier to implement, the NIRAS technique has been applied to all the mixtures listed in Table 3.1

6.4 Nonlinear Damping Parameter

6.4.1 Envelope Fitting

Another technique for measuring a sample's nonlinearity involves tracking changes in damping of the specimen with increased strain excitation. A convenient technique for measuring damping involves using the Hilbert Transform. The transform creates an analytic signal from real valued input data. Since the magnitude of the transformed signal gives the instantaneous amplitude, it can be used to approximate the envelope of a curve. The acquired signals in this research are all exponentially decaying sinusoids; therefore, the damping of the specimen can be measured by measuring the decay rate of the exponential curve. To approximate the decay rate (γ), the magnitude of the Hilbert Transform, is fitted to an exponential,

$$e^{\gamma(t-0.04)} \tag{6.5}$$

This is graphically illustrated in Figure 6.37.

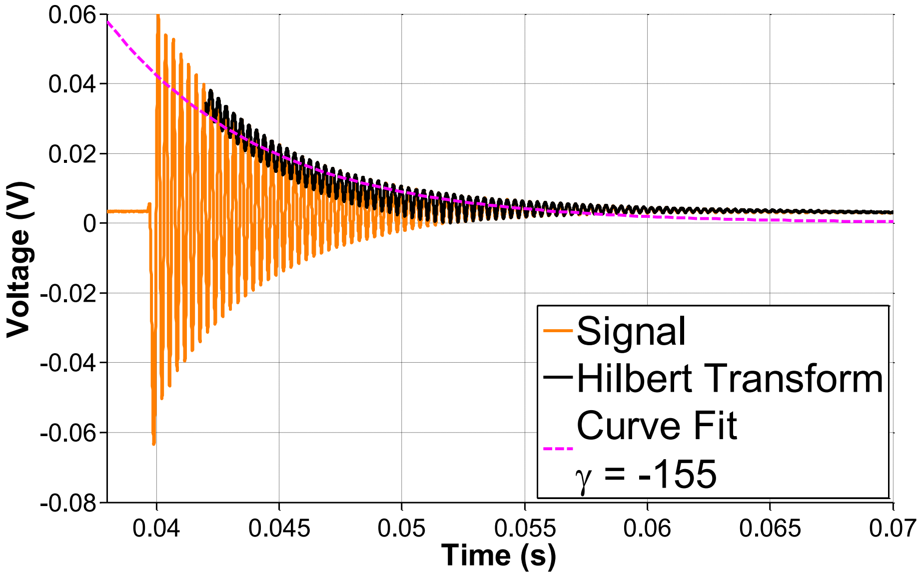

Figure 6.37. Hilbert Transform of recorded signal.

Notice that the recorded data shown in Figure 6.37, exemplifies a problem with the Hilbert transform in approximations of the envelope of a curve. The sampled data not only has a DC offset but there is an additional low frequency vibration, most likely from support mat, corrupting the signal. Both of these destroy the symmetry about the time axis which results in an incorrect envelope approximation. However, since the frequency range of interest is relatively high, a high pass filter can be applied to the signal to get rid of the low frequency content. Specifically a 4th order Butterworth high pass filter is applied with a cutoff frequency of 80 Hz, resulting in a significantly improved envelope approximation, shown in Figure 6.38,

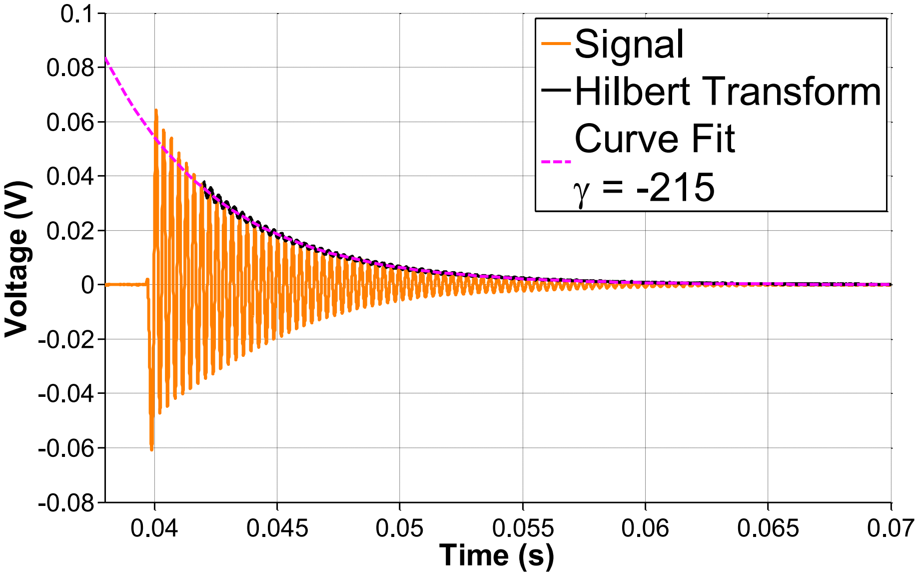

Figure 6.38. Hilbert Transform of recorded signal with high pass filter.

Also, notice that the Hilbert transform is applied with a 0.002 second delay in order to avoid transient effects from the hammer impact.

However, the decay rate (γ) is not purely a function of the damping ratio (ξ). As shown in Chapter 4, assuming the simple model, the decay rate approximated using the exponential fit of the envelope is also a function of the natural frequency ω_{nat},

$$\gamma = -\xi\omega_{nat} \tag{6.6}$$

The changes in the natural frequency (resonance frequency) are also incorporated into the decay rate measured. If this decay rate is used in Eq. (4.5) instead of the damping ratio, the alternate nonlinear damping parameter (Ω') can be calculated in much the same way as nonlinearity parameter. The normalized change in decay rate, from the lowest amplitude impact, is plotted against the same amplitude found from the FFT. The slope of this plot is the alternate nonlinear damping parameter, as shown in Figure 6.39.

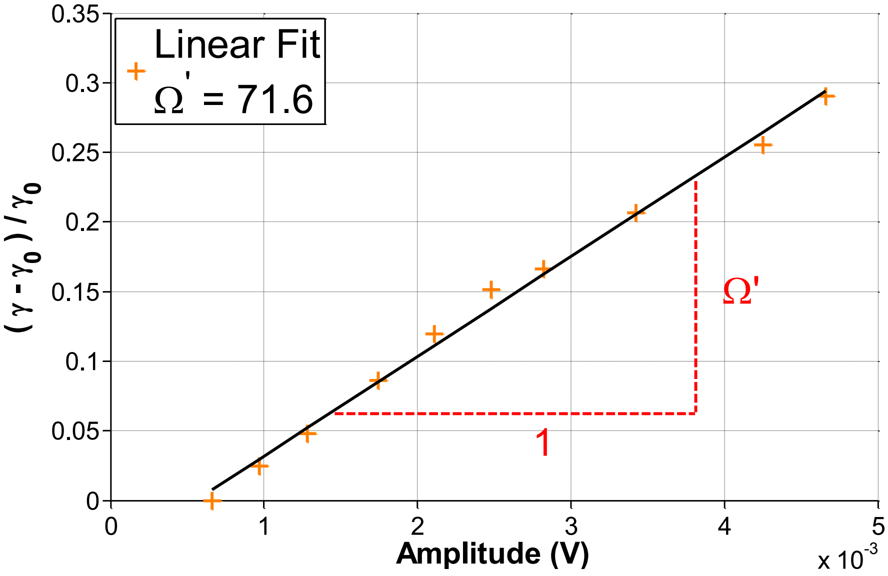

Figure 6.39. Normalized decay rate change vs. amplitude.

However, the natural frequency can be factored out of the damping rate by using the frequency of the maximum peak from the FFT. The result is a plot of the normalized change in damping ratio vs. amplitude of the peak where the slope is the nonlinear damping parameter, show in Figure 6.40, as dictated by Eq. (4.5).

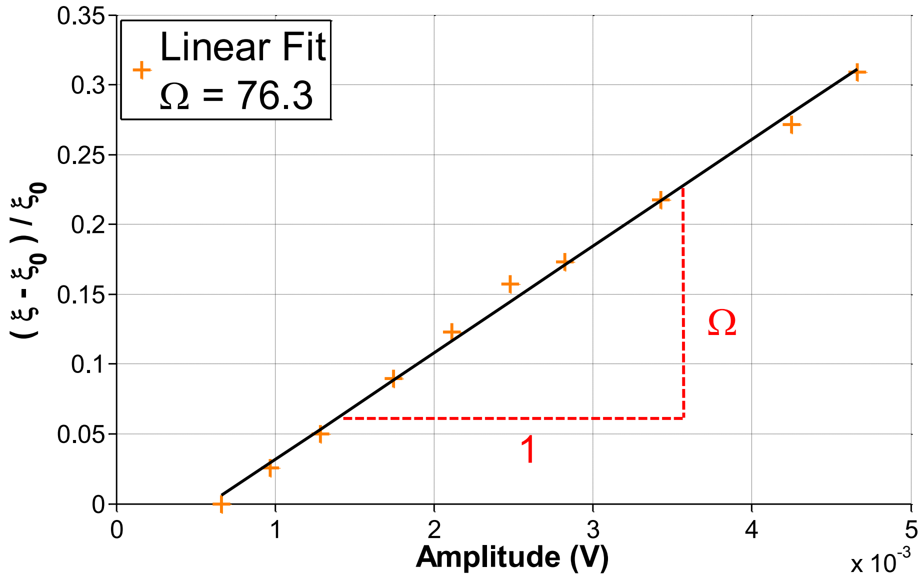

Figure 6.40. Normalized damping ratio change vs. amplitude.

Since both the damping ratio and the resonance frequency depend on the hysteresis parameter, there is not much difference between using the decay rate and damping ratio. This procedure for extracting the nonlinear damping parameter is followed for the reactive Mix 2 and the results are discussed in Chapter 8. The subsequent sections show the results of using the alternate approaches for approximation of the damping ratio which yield similar results to using the envelope approximation.

6.4.2 Using Quality Factor for Damping Ratio

Alternatively, the Quality Factor can be used to approximate the damping ratio. Assuming the simple mass-spring-damper system described in Chapter 4, the quality factor only depends on the damping ratio as discussed in Chapter 5.2. Using the signal in Figure 6.38 as an example, when the damping rate is normalized by the resonance frequency found from the FFT, the result is an estimate of the damping rate, shown in

Figure 6.41. The result of the envelope fitting yields a damping rate of approximately 0.0106 which is reasonable for a lightly damped system.

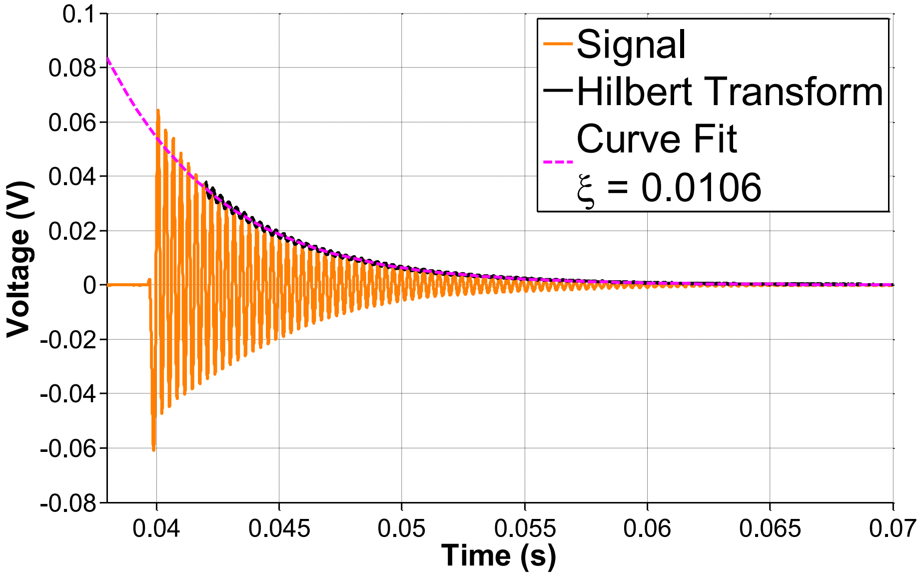

Figure 6.41. Recorded signal with high pass filter (showing damping ratio).

Transforming this signal to the frequency domain, shown in Figure 6.42, the damping ratio can be found by using the half power points and Eq. (5.18). The result is a damping ratio of about 0.0105, which is very close to the value found using the envelope approximation.

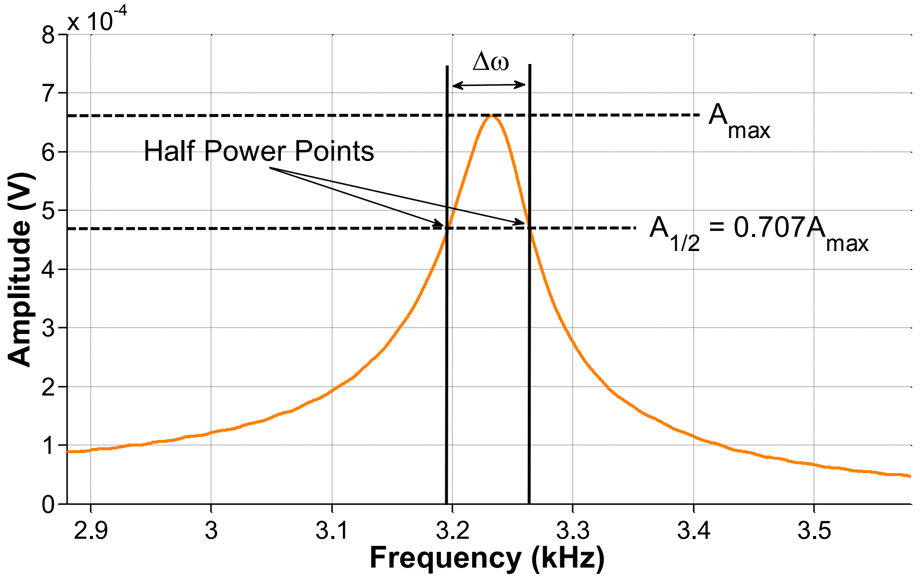

Figure 6.42. Extraction of quality factor.

6.4.3 Using Log Decrement for Damping Ratio

A third option is to use the log decrement approach to extract damping information, as discussed in Chapter 5.2 and illustrated in Figure 6.43. Using Eqs. (5.21) and (5.22), where the maxima used is 25 cycles from the chosen starting peak, the result is a damping ratio of about 0.0102 which is close to the values found with the other techniques.

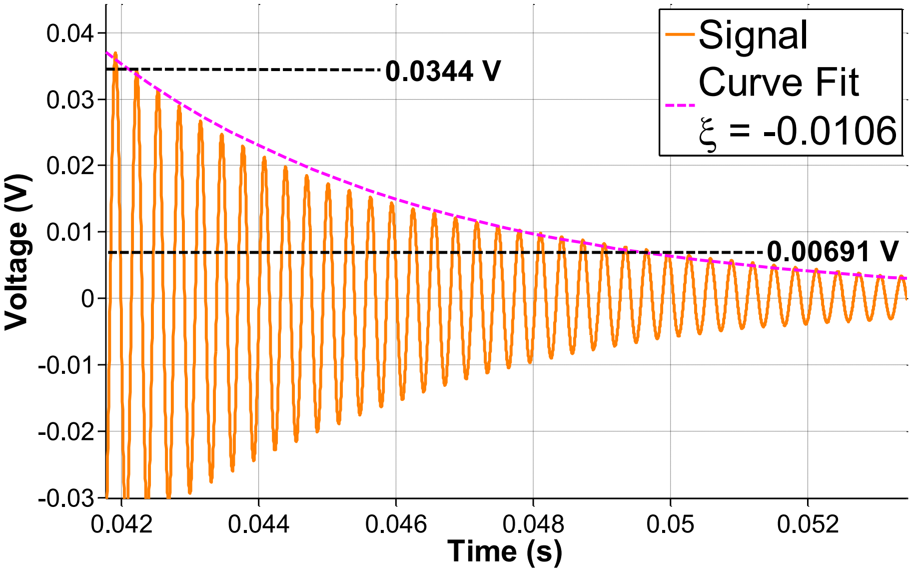

Figure 6.43. Application of log decrement approach.

CHAPTER 7

SAMPLE CHARACTERIZATION

7.1 Staining Technique

In addition to expansion measurements, a limited petrographic analysis is performed on companion CPT samples as a complementary assessment of the progression of damage. Petrography is a time consuming process which requires considerable experience to extract useful information from collected images. Additionally, subsequent testing is often required to confirm the composition of questionable features. Since ASR gel is described as “white, yellowish, or colorless; viscous, fluid, waxy, rubbery, hard; in voids, fractures, exudations, aggregate”, it can be extremely challenging to confirm its presence for a novice [48]. Therefore, the sample characterization in this examination relies on the use of a fluorescent stain which can be used to quickly identify the presence of ASR gel. The uranyl acetate staining technique was introduced by Natesaiyer and Hover and it has also been appended to ASTM C 856 *Standard practice for the petrographic examination of hardened concrete* [48, 49]. From previous studies it has been determined that silica gel possesses the capability of adsorption of ions as well as ion exchange. When the ASR gel is formed in concrete, the cations present may include calcium, sodium, and potassium. Due to the capability of ion exchange, the uranyl ion, in uranyl acetate stain solution, can replace the cations present in the gel. Since the uranyl ion fluoresces green when excited by ultraviolet radiation at 254 nm (UV-C light), the silica gel in concrete can be easily identified with a UV-C light source after staining. However, it has been found that siliceous, not necessarily reactive, aggregates also fluoresce because the silica surface always contains free OH^- groups with adsorbed cations, which can be replaced by the uranyl ion [49]. This can cause complications with the analysis of the images since the fluorescence of the aggregate can make it difficult to distinguish between the aggregate and reaction rims. Despite this limitation, the technique is still useful for tagging possibly relevant features in the microstructure, which simplifies the sample characterization.

7.2 Sample Preparation

From the concrete prism, a 1 in. thick rectangular sample is cut, using a table saw. The sample is then rinsed briefly with de-ionized water and placed in a fume hood, as a safety precaution. The 0.11 N uranyl acetate solution is applied to the freshly cut surface using a pipette and allowed to rest for one minute. Next, the surface is thoroughly rinsed with de-ionized water and the sample is then placed under a microscope. A heavy tarp is placed over the microscope instead of using a dark room. A UV lamp is used to illuminate the surface of the sample and a built in camera (SPOT Insight Color Camera) is used to capture the image from the microscope (Leica MZ6 stereomicroscope), shown in Figure 7.1

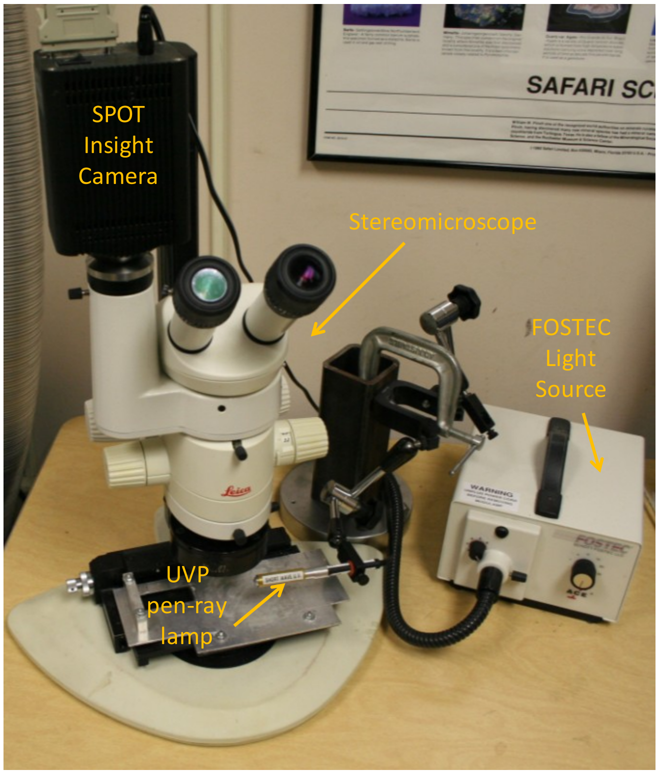

Figure 7.1. Microscope setup for petrographic examination.

The initial characterization was conducted using a handheld UV lamp (UVP Model UVSL-14P), shown in Figure 7.2, and, in an effort to improve image quality, a higher intensity pen-ray lamp (UVP Model 11SC-1), with short wavelength filter, has been used in the later stages of examination, shown in Figure 7.3.

Figure 7.2. Handheld UV lamp.

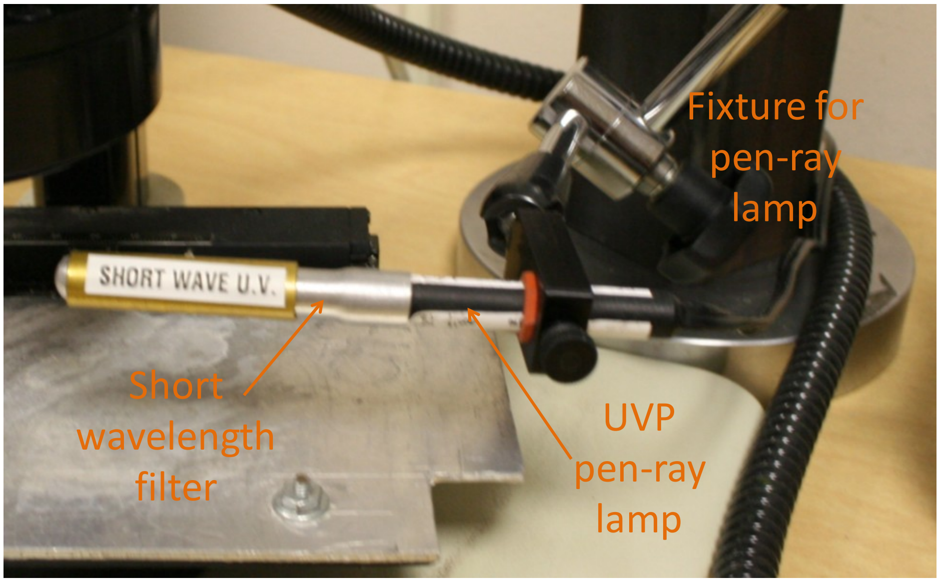

Figure 7.3. Pen-ray UV lamp.

Note that the results for the initial petrographic examinations were done on unpolished sections. The loss of the gel was a concern at the start of the petrographic examination and it was decided to forego polishing to limit this.

7.3 Comparison of Polished and Unpolished Sections

However, in an effort to improve image quality, polishing was tried on an ASR damaged Las Placitas sample. The samples were only polished for ~2 minutes with a 60 grit size on a rotating polishing table. Observation of fluorescing ASR gel suggests that the sample preparation methods used are appropriate for these types of samples. Figure 7.4a shows a representative unpolished stained section for a concrete prism with a reactive aggregate and Figure 7.4b shows a polished section for the same concrete prism (different section) with and without UV-C illumination. The concrete prism is a recast version of Mix 2. Comparing the images in Figure 7.4 there does not appear to be any evidence of loss of ASR gel. In fact Figure 7.4b shows a relatively large crack which still stained after polishing. Comparing the quality of the images, the unpolished section does not appear as clear as the polished section. For the unpolished section, is difficult to achieve good focus, especially at higher magnifications, resulting in diminished image quality. For the polished section, the image is not only in focus but the stained features are more distinct. In the polished section it is even possible to distinguish microcracks at the edge of the macrocrack.

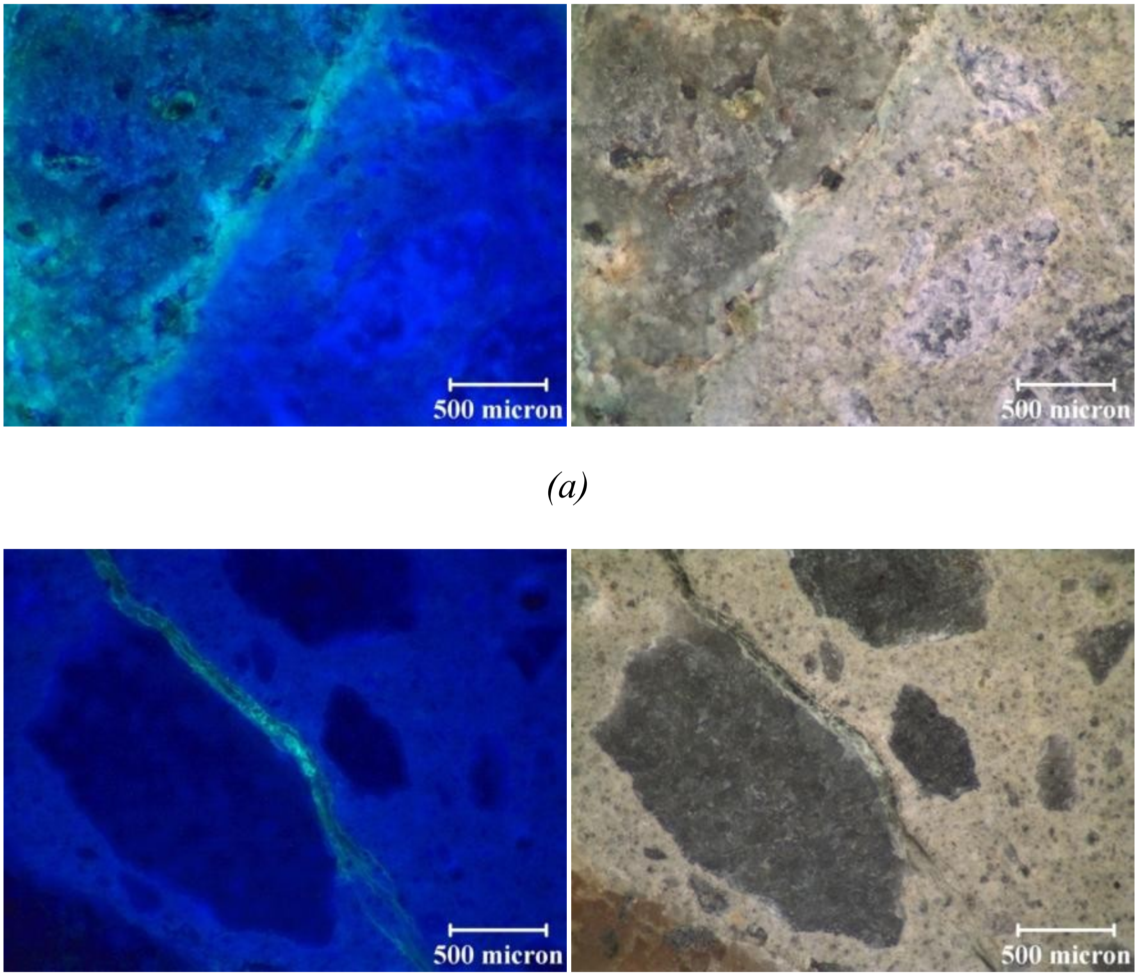

(a)

(b)

Figure 7.4. (a) Unpolished stained section and (b) polished stained section.

Figure 7.5 shows another example of the improvement of image quality through polishing of sections. In Figure 7.5a, due to the rough surface, both images do not have good clarity and staining appears to be smeared, which can be attributed to the cutting process. In Figure 7.5b, the images are much clearer and the staining is focused.

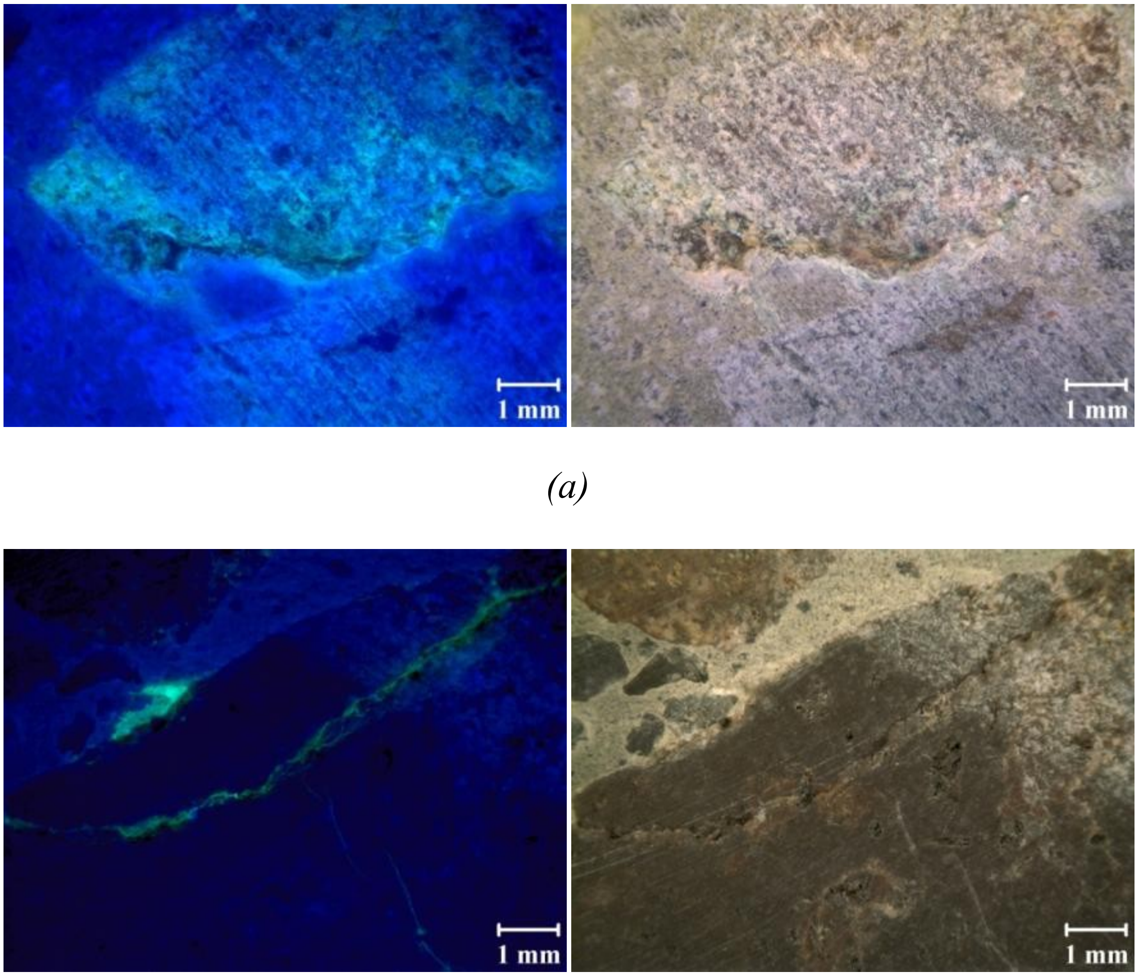

(a)

(b)

Figure 7.5. (a) Unpolished stained section and (b) polished stained section.

Based on these results, polishing is recommended as part of the sample perpetration for sample characterization using the uranyl acetate staining technique.

CHAPTER 8

RESULTS AND DISCUSSION

8.1 Expansion Results

This section presents the current expansion measurement results for the concrete mixtures described in Table 3.1. Note that in this study the expansion measurements are taken more frequently than in the ASTM C 1293 standard. Results of the expansion measurements for the highly reactive mixtures are shown in Figure 8.1. Comparing the results from ASTM C 1260 (Table 3.1) and the measured expansions in Figure 8.1, it is evident that there is good agreement for the classification of reactive mixtures. Figure 8.1b shows results up to 100 days to facilitate identification of the specimen age at which the 0.04% expansion limit is crossed. The mixes that cross this limit are classified as reactive and include Mixes 2-5. Mixes 2 and 3 can further be classified as highly reactive due to the rapid expansion rate. There also appears to be a trend of more rapid and larger expansion when the reactive aggregate is crushed and used as the fine in the mixture. This is demonstrated when comparing Mixes 2 and 3 as well as Mixes 4 and 5. However, Mix 4 has been recast, to better evaluate the early expansion behavior, and has uncharacteristically high rate of expansion compared to previous results. Currently there is no explanation for this difference in behavior between the two sample sets; it may simply be related to the variability inherent in concrete and in reactive aggregates in particular.

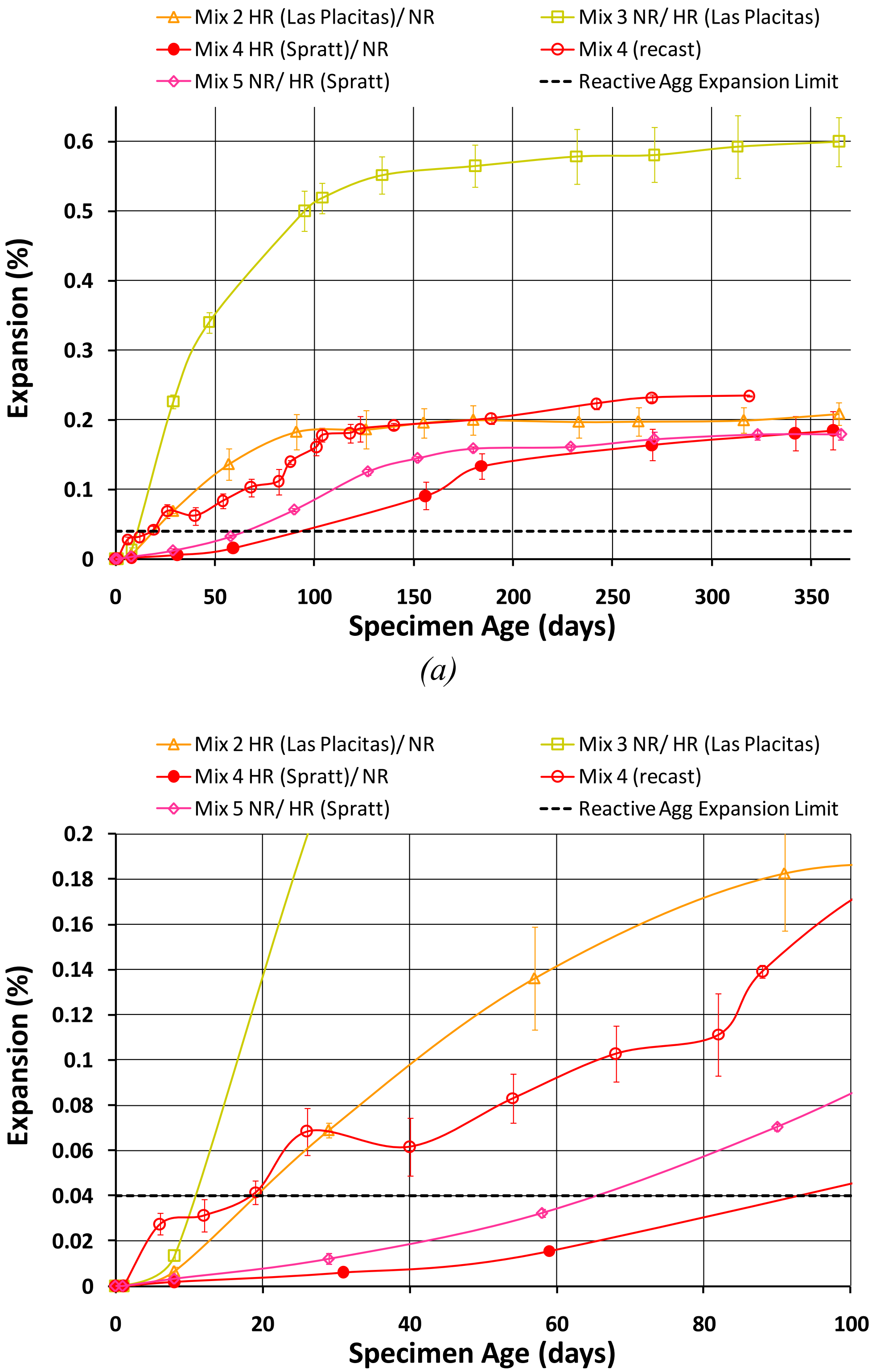

(a)

(b)

Figure 8.1. (a) ASTM C 1293 expansion results up to 370 days. (b) ASTM C 1293 expansion results up to 100 days.

Current results for the nonreactive Mix 1, the moderately reactive Mixes 6 and 7, and SCM-containing Mixes 8 and 9, are presented in Figure 8.2. The average expansion of Mixes 1 and 6 has not crossed the expansion limit at one year; therefore these are classified as nonreactive by the standard. Mix 6 was initially expected to be moderately reactive, since according to ASTM C 1260 it was classified as potentially reactive. According to these results, the mixture is nonreactive but it does come very close to the expansion limit. The 25% addition of fly ash appears to be effective since the expansion limit has not been crossed, while Mixes 4 and 5, using the same aggregate, crossed the limit in less than 100 days. Mix 7 has crossed the limit at about 150 days and can be classified as reactive using the standard, but it is has remained close to the expansion limit since crossing the threshold.

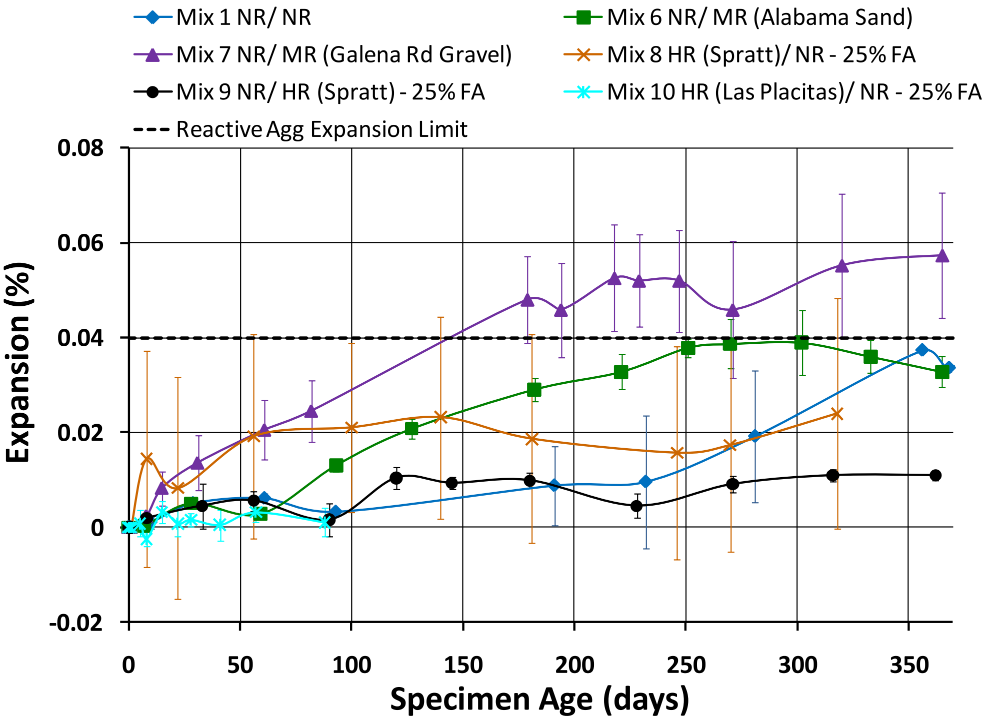

Figure 8.2. ASTM C 1293 expansion results up to 370 days for moderately reactive, nonreactive, and SCM mixes.

8.2 NIRAS Results

NIRAS results are presented in a similar manner as the expansion measurements. The measured nonlinearity parameter, for the same three specimens as expansion measurements, is averaged and plotted at each test date. With this representation the nonlinearity parameter is shown as a function of time that samples have been exposed to ASTM C 1293 testing conditions. It is important to note that since the NIRAS measurements did not start on Mix 4 until after the expansion was greater than 0.04%, this mixture has been recast in order to gather early age data for that mix.

As an example, consider Mix 3 at 47 days. The results for one of the samples are shown in Figure 8.3. The impact response for 10 separate hits is recorded and converted to the frequency domain as described previously. The frequency shift is then normalized and plotted against the excitation, as shown in Figure 8.3.

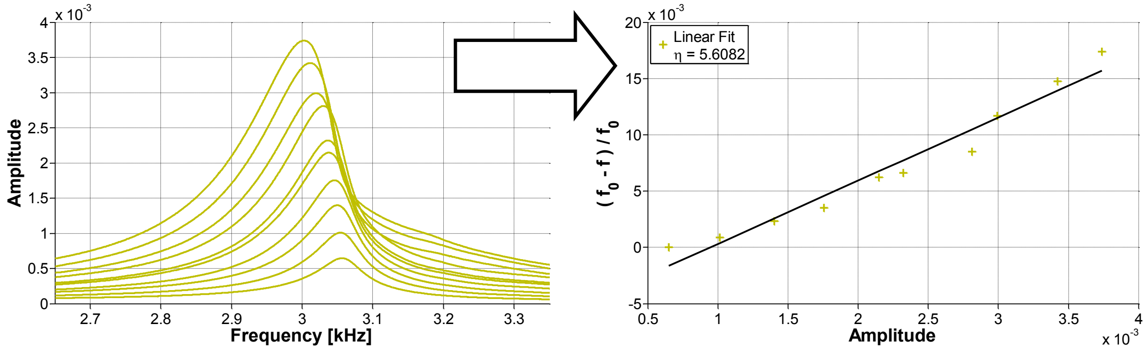

Figure 8.3. Example of extraction of nonlinearity parameter.

The nonlinearity parameter (η) is the slope of the data on this plot; in this case, η is found to be 5.61. For the other samples the nonlinearity parameters were measured to be 7.28 and 5.69. The average of these nonlinearity parameters is then 6.19. This average nonlinear parameter, along with standard deviation, is then plotted in Figure 8.4. The average nonlinearity parameter of 6.19 at 47 days can be seen in Figure 8.4 and corresponds to the maximum nonlinearity measured for Mix 3. Figure 8.4a shows the current results up to one year while Figure 8.4b shows a more detailed view, only up to 100 days, to show early age behavior.

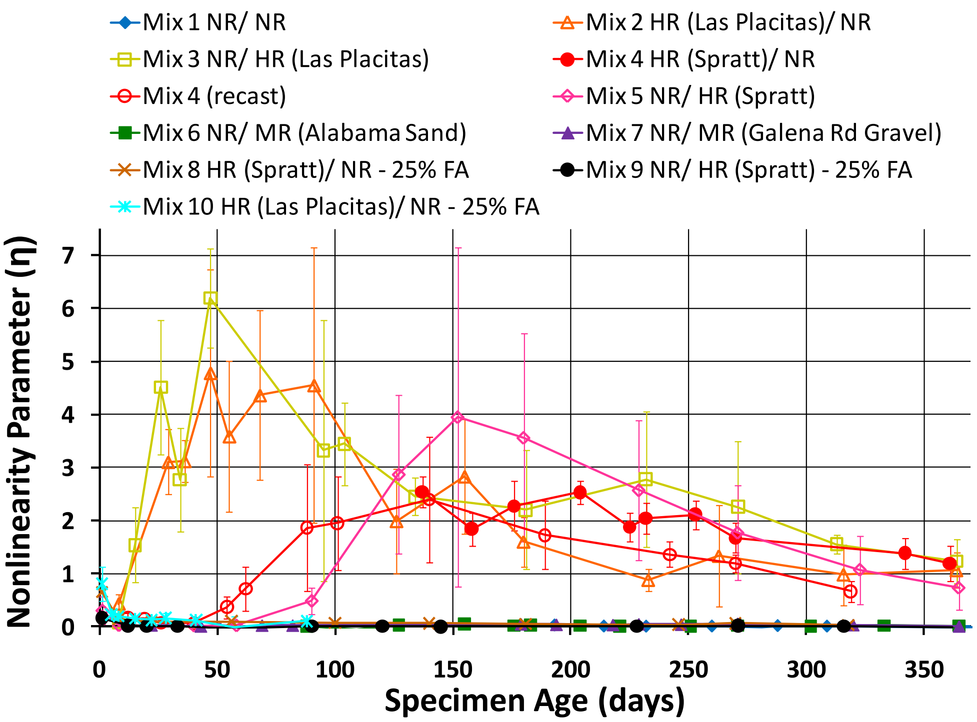

(a)

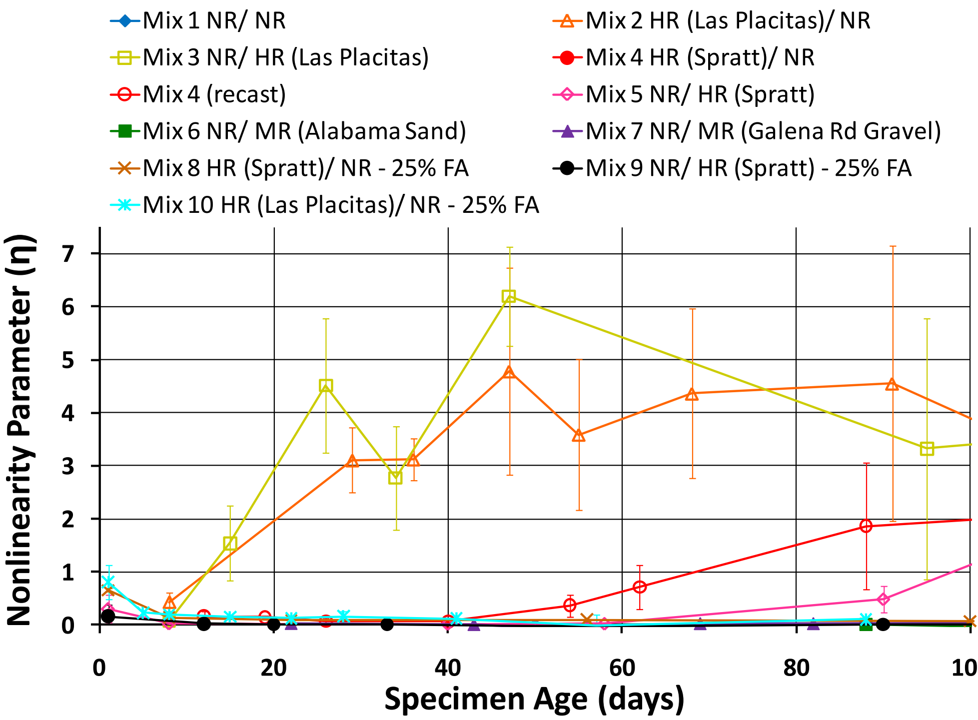

(b)

Figure 8.4. (a) NIRAS results up to 370 days. (b) NIRAS results up to 100 days.

The results show that the NIRAS technique confirms the ASTM C 1293 reactivity classification based on expansion results for the nonreactive and highly reactive mixtures. For both Mix 1 and Mix 6, the average expansion of the specimens has not crossed the 0.04% limit, indicating a nonreactive aggregate. The nonlinearity of those specimens has remained very close to zero throughout the year of testing, also indicating a nonreactive aggregate. While the expansion for any concrete sample including the nonreactive mixes increases as the duration of the test increases, the nonlinearity does not change for a nonreactive aggregate, providing a more definitive and accurate result. Additionally notice that the expansions for Mixes 1 and 6 come very close to the expansion limit; a result for which it can be difficult to extract a definitive conclusion from. For aggregates initially classified as highly reactive, once again measures of expansion and nonlinearity are in agreement. In some cases, there is an indication of earlier detection of reactivity using nonlinearity. Comparing Mix 2 in Figure 8.1b and Figure 8.4b, it can be seen that the NIRAS technique is capable of identifying ASR slightly sooner than the expansion measurements; nonlinearity is detected at 8 days while the expansion limit is crossed at about 25 days. However, further investigations is clearly needed in this area in order to determine what kind of microstructural changes cause nonlinearity as well as what level of nonlinearity can be considered detrimental. These investigations will enable us to tell about the damage in concrete in a more quantitative manner and to give a definitive criterion for reactivity of an aggregate, consdering its microstructure and chemical properties. The only mix for which the nonlinearity measurements are contrary to expansion results is for Mix 7. The expansion limit has been crossed for that mix but to date nonlinearity still remains negligible. Petrography has been performed on this mix in an attempt to validate the results and the results are presented in Section 8.5 of this chapter. Table 8.1 presents a summary of the reactivity classifications based on expansion and nonlinearity for the mixtures without SCMs because the testing for Mixes 8, 9, and 10 is still ongoing and the only conclusion that can be made is that a 25% fly ash is effective at supressing the reaction.

Table 8.1. Summary of reactivity classification.

Sample	Reactivity based on Expansion	Reactivity based on Nonlinearity
Mix 1	Nonreactive*	Nonreactive
Mix 2	Reactive	Reactive
Mix 3	Reactive	Reactive
Mix 4	Reactive	Reactive
Mix 5	Reactive	Reactive
Mix 6	Nonreactive*	Nonreactive
Mix 7	**Reactive****	**Nonreactive**

* Classified as nonreactive but close to expansion limit at end of test.
**Classified as reactive but remained close to expansion limit after crossing.

Further, Mixes 2 and 3 can also be labeled as *highly* reactive by both expansion and nonlinearity resutls due to early detection of reactivity by both methods.

8.2.1 NIRAS Results for Reference Samples

The reference samples held at laboratory conditions were also tested for nonlinearity, where the resutls are shown in Figure 8.5. All the values of nonlinearity for reference mixtures are considerably lower than what is measured for reactive mixtures that have undergone CPT testing. The reference mixtures are made from the same batch as the samples subjected to CPT, the only difference being the environmental conditions. The reference mixtures are stored in an environment lacking in moisture, which is necessary for ASR and lower temperature (higher temperatures accelerate the reaction). For example, the results for Mix 4, for both CPT and reference samples are shown in

Figure 8.6 and Figure 8.7. Notice that in addition to a negligible frequency shift the reference sample has a sharper resonance at a higher frequency due to lower attenuation.

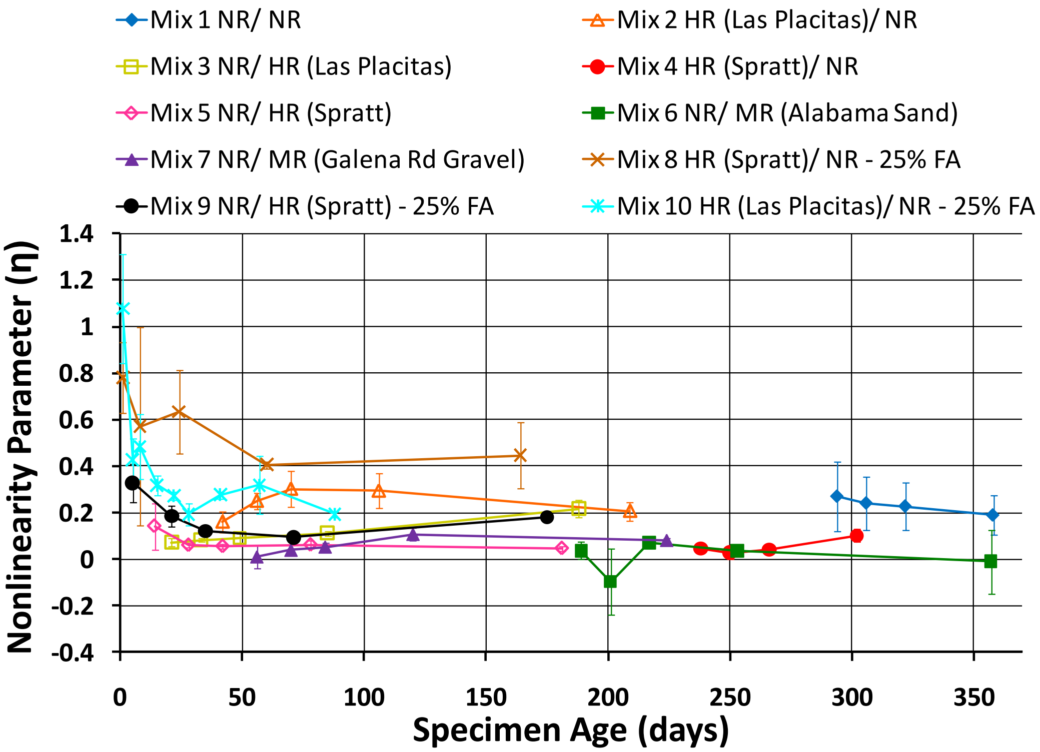

Figure 8.5. NIRAS results for reference mixes.

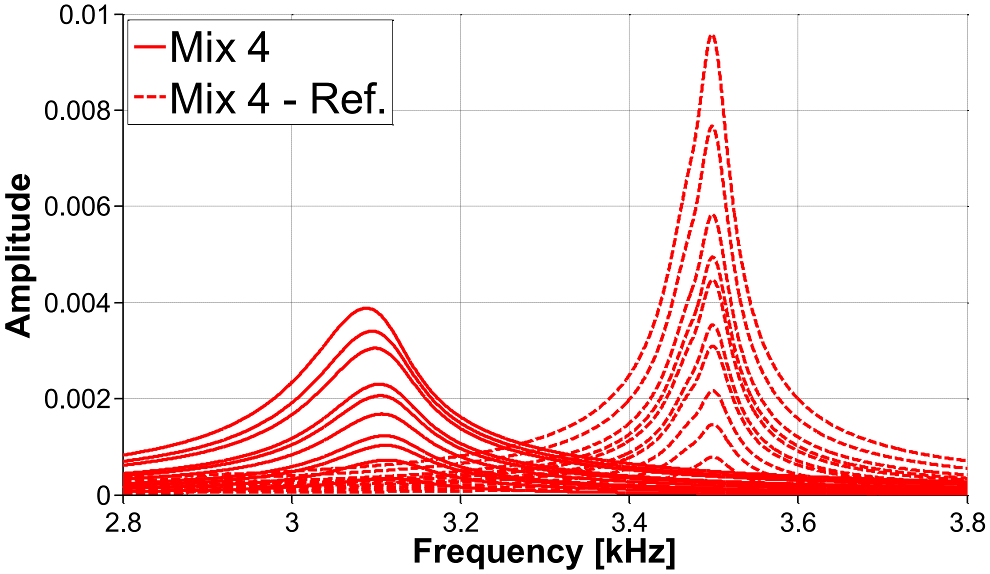

Figure 8.6. Nonlinearity comparison between reference and tested samples for reactive Mix 4 250 days.

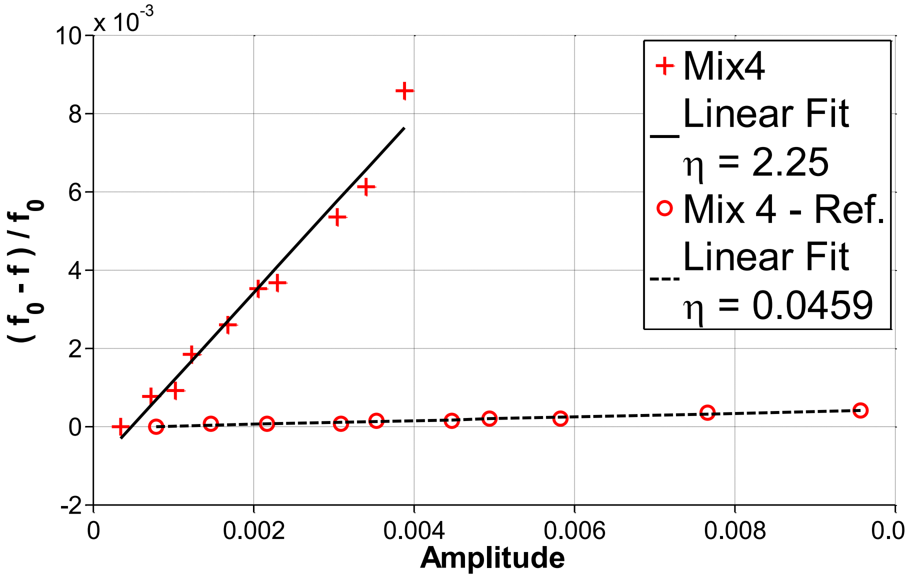

Figure 8.7. Comparison between reference and tested samples for reactive Mix 4 at 250 days in the frequency domain.

It is interesting to note that in Figure 8.4b and Figure 8.5, mixtures tested at the first day show some nonlinearity which then decreases down to zero though subsequent testing. This can be caused by the continued hydration of the cement after demolding, which decreases the inherent material nonlinearity by eliminating defects present before the material nonlinearity due to ASR becomes dominant. (Hydration is a complicated chemical reaction which occurs between water and cement to form reaction products responsible for hardening and setting properties of concrete [29]) The results for the reference mixes are surprising for the nonreactive mixtures, since slightly lower nonlinearity is detected for the specimens subjected to CPT. The reason for this anomaly could be related to variations in inherent defects between the two sample groups or by limitations of hydration caused by the drier storage environment. Since the CPT sample group has abundant moisture available and is exposed to warmer temperatures, nonreactive mixtures can achieve better hydration and hence lower nonlinearity than the reference sample group. Since the reference samples undergo only one day of curing, it is possible that the inadequate hydration can be the cause of the slight nonlinearity in the nonreactive reference mixtures. The results indicate that it may be possible to use this technique to investigate the cement hydration process, as well as self-healing in cementitious systems. Additionally, after demolding there is shrinkage in the dry environment. For Mix 10, the expansion of the reference group was also recorded and currently the shrinkage is about 0.02%, about half the expansion limit. This significant shrinkage can also be responsible for a small amount of microcracking and as a result some nonlinearity.

8.2.2 Decrease in Nonlinearity Parameter and Cumulative Nonlinearity

In addition, a decrease in nonlinearity parameter has been observed for reactive mixes at later ages. This decrease is not yet fully understood. It is feasible that at early ages there is some competition between hydration of cement paste and accumulation of damage as a result of ASR, which can cause variations in the nonlinearity measurements. It is also postulated that a decrease in nonlinearity can be accompanied by cracks growing to larger sizes. The measured nonlinearity comes from the nonlinear behavior of cracks, through the interaction of crack surfaces. When a crack becomes too large or perhaps fills with gel, the crack faces may no longer interact and, as a result, no longer contribute to nonlinearity. It is thought that this is the reason for an eventual decrease in nonlinearity at later ages. It is important to notice that this decrease in nonlinearity appears to occur at about the same time the expansion rate starts to decrease and level off. Perhaps the same phenomenon is responsible for the eventual decrease in expansion rate and decrease in nonlinearity observed in the results. However, taking the measured nonlinearity as an instantaneous measure the data is integrated, as described in Chapter 4, to find the accumulated damage. The results, shown in Figure 8.8, demonstrate an even greater distinction between reactive and nonreactive mixtures. Figure 8.9 shows a detailed view of the cumulative nonlinearity for the low/moderately reacting mixtures. Using the cumulative nonlinearity for these low/moderately reacting mixtures there is some distinction that can be seen between the mixtures that could not be seen from the instantaneous nonlinearity from Figure 8.4. One important observation from these results is that about same level of nonlinearity has developed in the reactive Mix 4. This result can be seen in both Figure 8.4 and Figure 8.8. The expansion measurements, Figure 8.1, show completely different results for the recast Mix 4 than were recorded for the initially cast batch. Although the cause of this discrepancy is unknown, it is evident that nonlinearity measurements remain largely unaffected.

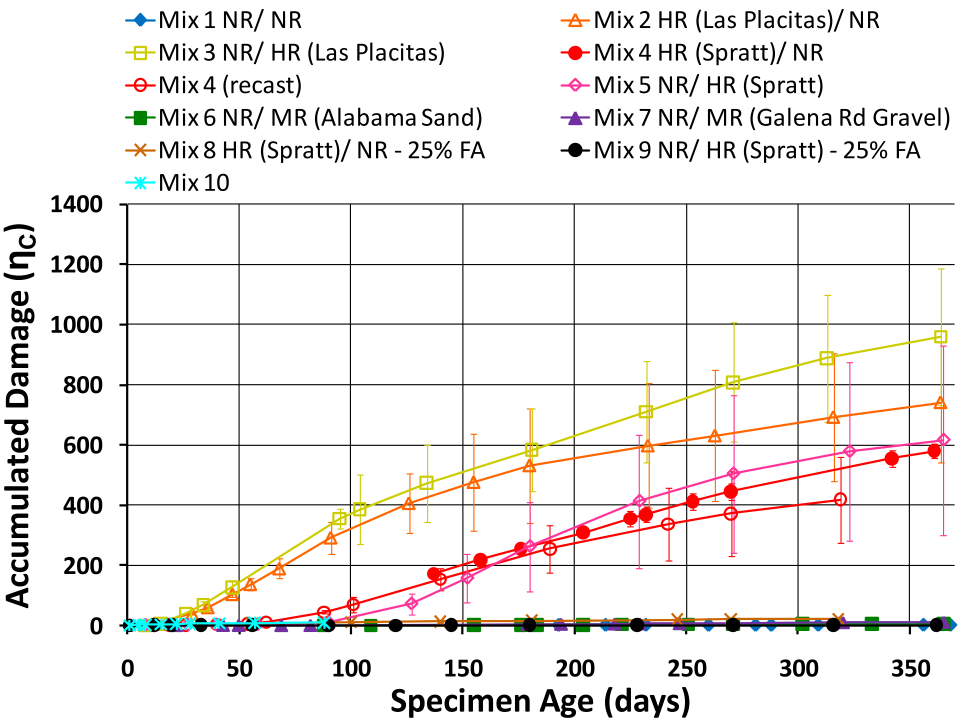

Figure 8.8. Cumulative nonlinearity.

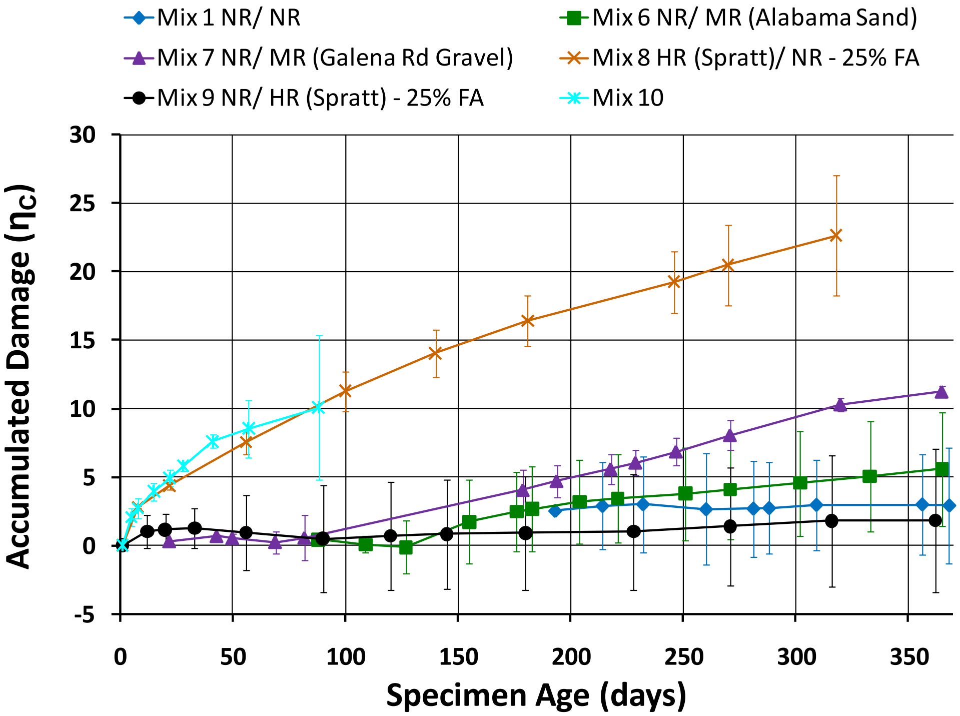

Figure 8.9. Cumulative nonlinearity for low/moderately reactive aggregates.

As mentioned earlier, the expansion measurements seem to indicate a faster rate of reaction when the reactive aggregate is used as a fine instead of a coarse, except for the case of the recast Mix 4. With the NIRAS measurements, there is no observable trend with the size of the reactive aggregate. This can be beneficial in laboratory testing since there is no effect of gradation on the results of reactivity classifications.

The standard deviation, represented by error bars, shows the variability in the three samples tested for each mix. Both the expansion measurements and measurements of η have a general trend of increasing standard deviation with increased expansion, or nonlinearity. Due to inherent heterogeneities, the cast prisms are not identical to each other, even within the same mix. As a result, each sample represents a different material system which can accumulate damage in different ways. Due to the high sensitivity of NIRAS, the standard deviation is larger for reactive mixes.

8.2.3 Changes in “Linear” Resonance Frequency

Since the lowest amplitude impact is assumed to be the approximate linear resonance frequency, this measure can also be used to track changes to the specimens. In general this data, shown in Figure 8.10, complements the nonlinearity measurements. Looking at data for Mixes 5, 8, and 9 from Figure 8.4 and Figure 8.10 we can see that theses mixes start with a low linear resonance frequency and relatively high nonlinearity after de-molding. Subsequently the linear resonance frequency increases (increase in elastic modulus due to hydration) and nonlinearity decreases. These data support the postulated explanation for relatively high initial nonlinearity and slightly higher nonlinearity for nonreactive reference mixes. Overall, an observed decrease in linear resonance frequency also has an increase in nonlinearity, demonstrating an inverse relationship between changes in linear resonance frequency and nonlinearity parameter. However, the changes in nonlinearity are significantly larger than the changes in the linear resonance frequency and can be used to more accurately assess changes in the specimens.

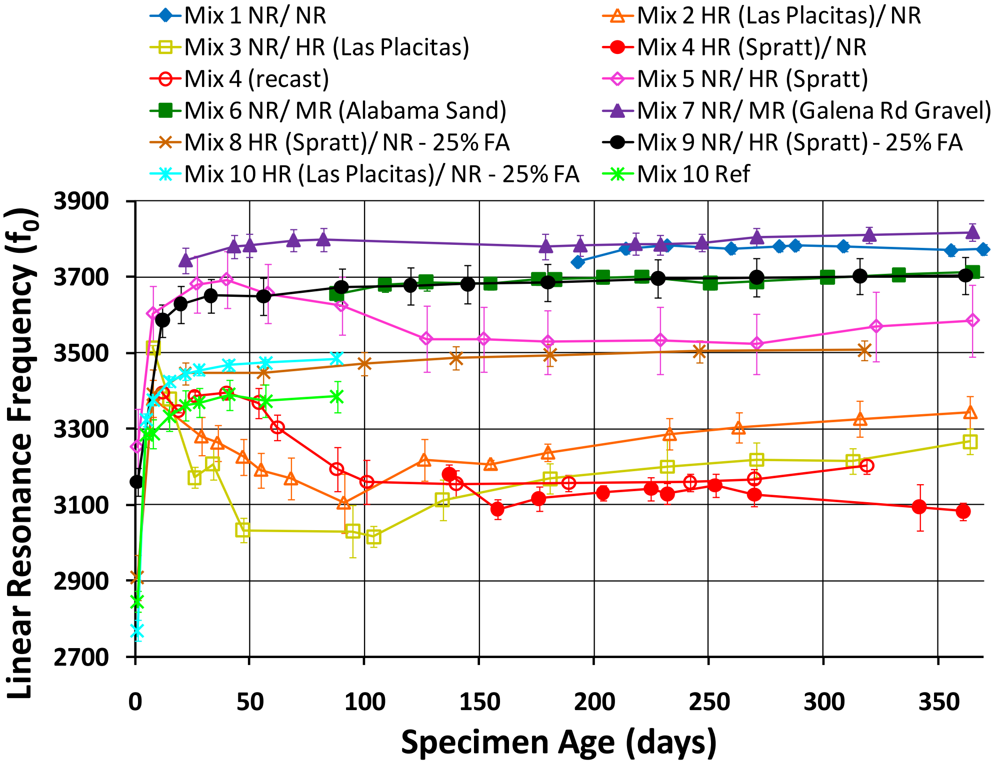

Figure 8.10. Changes in linear resonance frequency.

8.3 Nonlinear Damping Results

Data collected throughout the project was re-analyzed using the Hilbert transform. The changes in damping ratio with increasing excitation were calculated at each specimen age in the same manner as in the calculations for resonance frequency were made, using Eq. (4.5). The results of this analysis are compared to the measures of resonance frequency changes for the highly reactive Mix 2, shown in Figure 8.11 and Figure 8.12, where the normalization is with respect to the first data set.

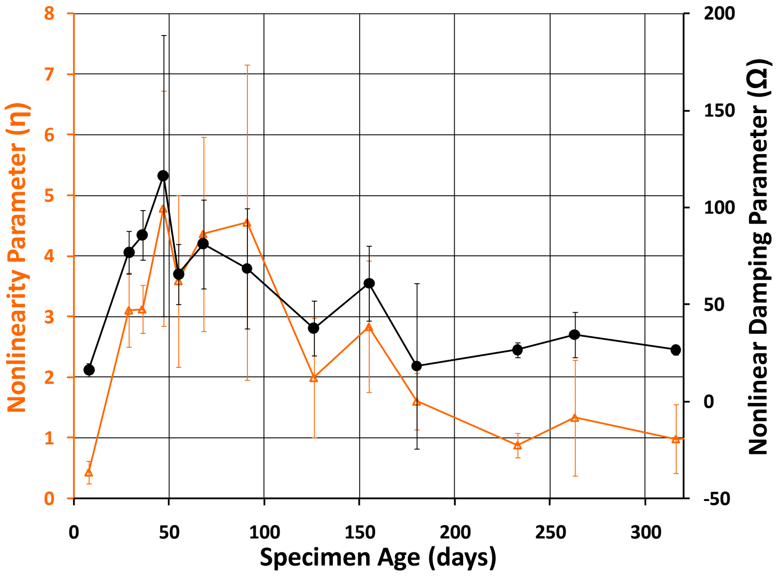

Figure 8.11. Comparison between nonlinearity parameter and nonlinear damping parameter.

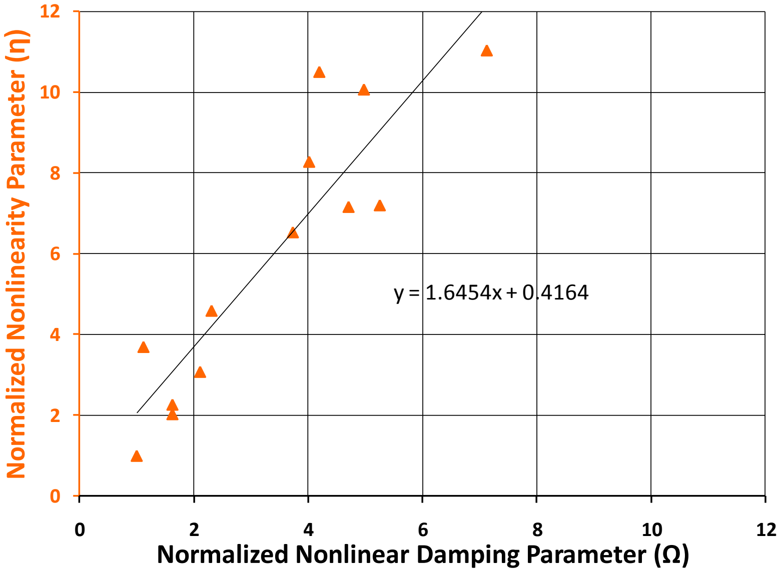

Figure 8.12. Direct comparison between nonlinearity parameter and nonlinear damping parameter.

As expected, these results clearly show that both methods have the same fluctuations since they are both related to the same hysteresis parameter. The results using the quality factor are also comparable, shown in Figure 8.13 and Figure 8.14.

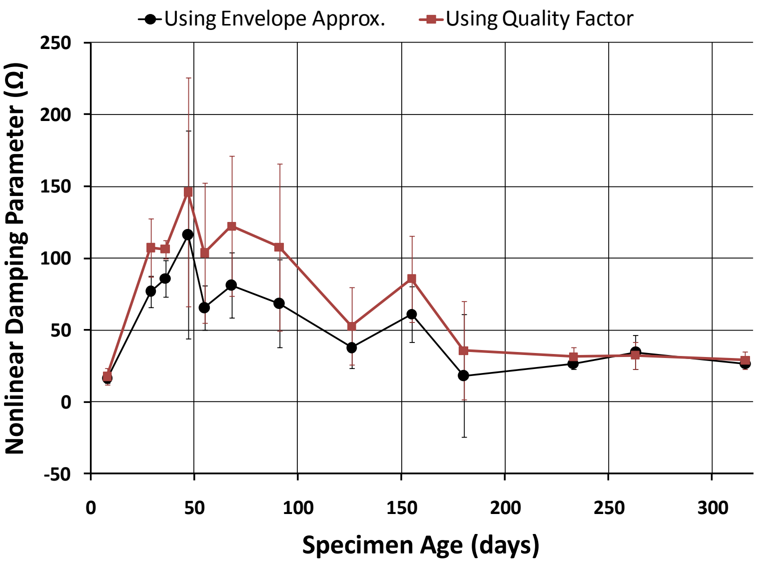

Figure 8.13. Comparison between using envelope and quality factor for nonlinear damping parameter.

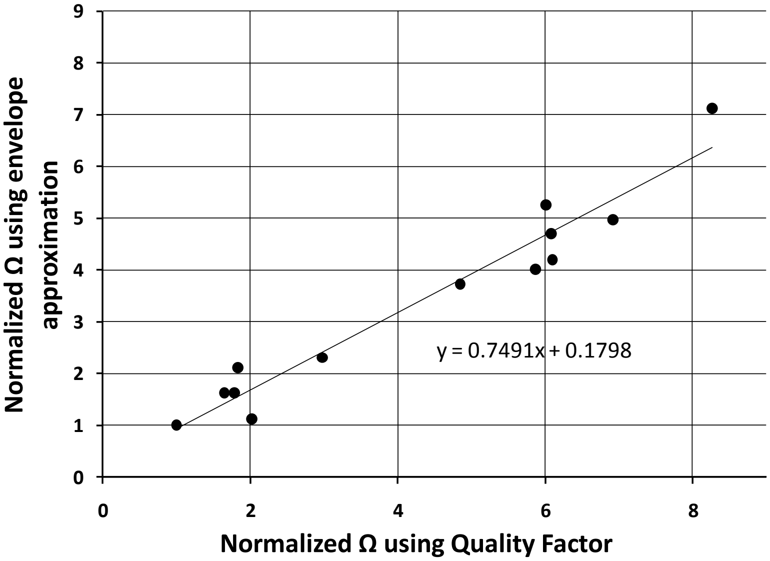

Figure 8.14. Comparison of nonlinear damping results.

This makes sense since both the nonlinearity parameter and nonlinear damping parameter are proportional to the material hysteresis, which is assumed to be dominant in this type of damage. While the nonlinear damping parameter has proven to be a viable method for characterization of material nonlinearity, the technique requires a more careful analysis and is considerably harder to implement. Additionally, the damping parameter is found assuming a very simple mass-spring-damper system model; therefore, the recommended approach is to use the nonlinear parameter found using resonance analysis.

8.4 Cored Sample Results

To assess whether the NIRAS technique might be used to examine ASR damage in the field, cored samples obtained from two different pavements were also tested. The cores were supplied by the Georgia Department of Transportation (GDOT). One core was taken from I-75 and another was taken from HWY 316. The concrete from HWY 316 is suspected to have ASR damage, while that from I-75 was not expected to have ASR. The cores were tested in the same manner and with the same setup described in Chapter 6. The results for I-75 and HWY 316 are shown in Figure 8.15 and Figure 8.16, respectively.

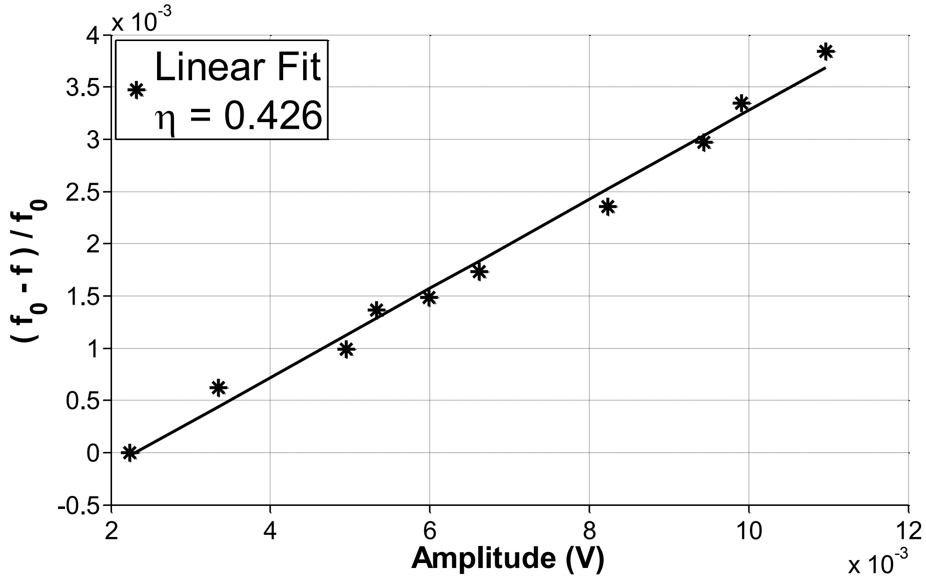

Figure 8.15. Nonlinear measurement results on I75 core.

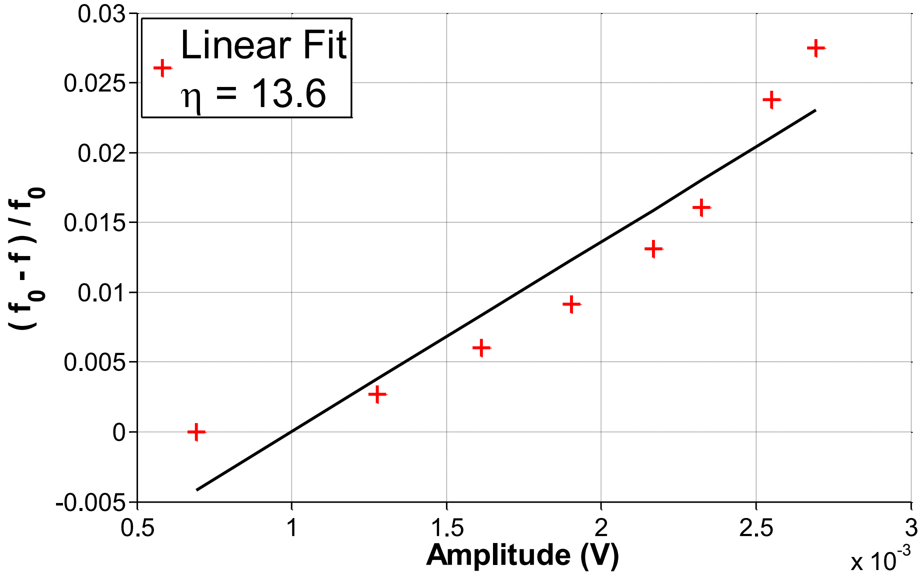

Figure 8.16. Nonlinear measurement results on HWY 316 core.

These results clearly show that HWY 316 has a significantly higher nonlinear parameter indicating that it has damage. While the cause of damage is unclear, the measurements suggest that the result is an extensively microcracked road. This technique offers an extremely rapid and non-subjective evaluation of cores which can be used assessment of structures in the field.

8.5 Sample Characterization Results

Preliminary petrographic examination was done on recast batches of Mixes 2-5. For the petrographic examinations, five samples were cast; three were used for expansion measurements and two for petrography.

8.5.1 Sample Characterization for Mix 2

The results of the examination, using the uranyl acetate stain on a recast Mix 2, are shown in Figure 8.17. Figure 8.18 shows the expansion measurements for the originally cast Mix 2 samples as well as the results for the batch cast for petrography.

Additionally, the nonlinearity of the original Mix 2 samples is plotted on the secondary axis for comparison.

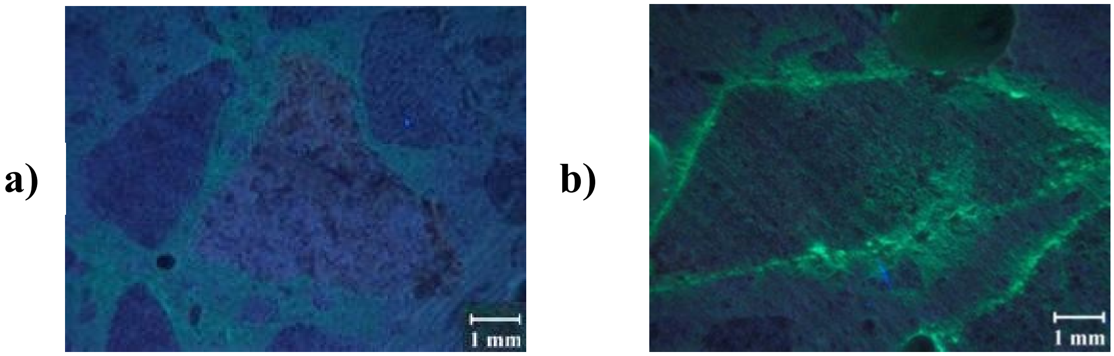

Figure 8.17. a) Petrographic image for Mix 2 at 1 day. b) Petrographic image for Mix 2 at 9 days.

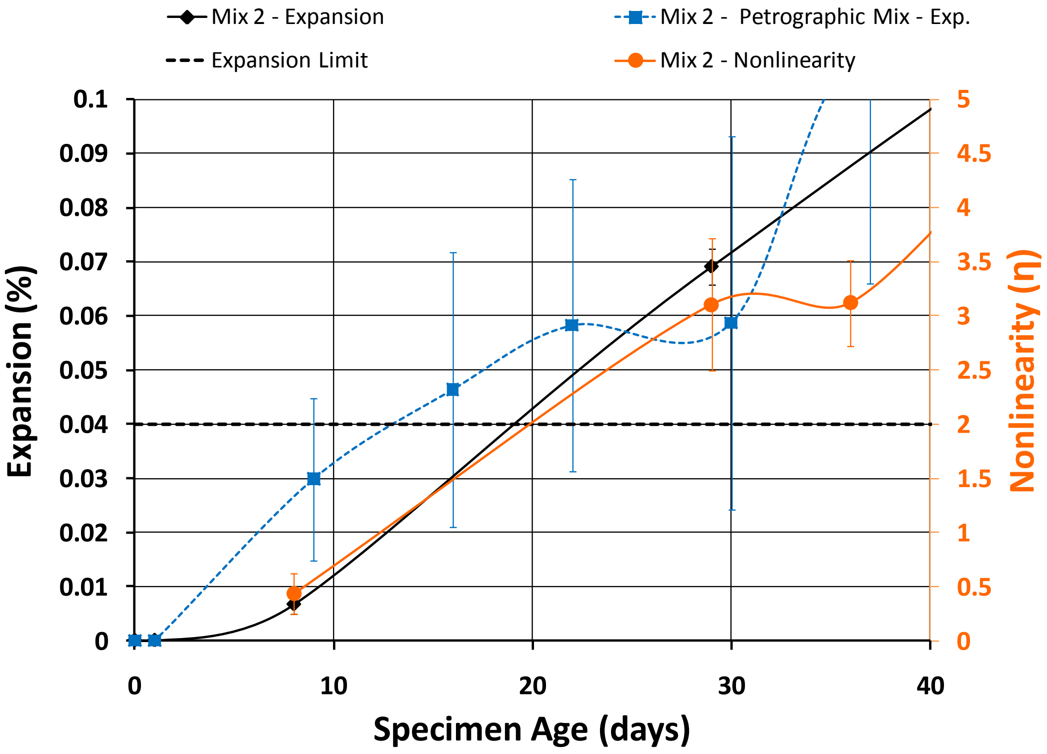

Figure 8.18. Comparison of expansion and nonlinearity results for Mix 2.

Comparing Figure 8.17a and Figure 8.17b, there is a clear difference in the staining at different specimen ages. At one day, the representative cross-section in Figure

8.17a shows only a light staining of the paste but no signs of bright staining of reaction rims around aggregates. At nine days, Figure 8.17b, there is clear evidence, due to preferential staining of reaction rims forming around certain aggregates, of ASR activity. These results are consistent with the nonlinearity results for Mix 2, where the measurements show a detectable nonlinearity at the first measurement at 8 days. These results show that nonlinearity measurements lead the expansion results since the expansion limit is not crossed until about 20 days for the original Mix 2 sample. (However, the expansion limit is crossed earlier, about 13 days, for the recast petrographic mix. Since nonlinearity was not measured for that set, it is not known if the nonlinearity measurement would lead the expansion measurement in that case.) At later ages the petrographic results show substantial staining throughout the concrete matrix and it is difficult to determine what microstructural changes are affecting the nonlinearity measurements.

8.5.2 Sample Characterization for Mix 3

The results for the recast Mix 3 are shown in Figure 8.19. Mix 3 has a mixture of reactive fine aggregate and the expansion is faster than Mix 2, which contains reactive coarse instead. The results of both expansion and nonlinearity are in agreement and indicate reactivity at around the same age.

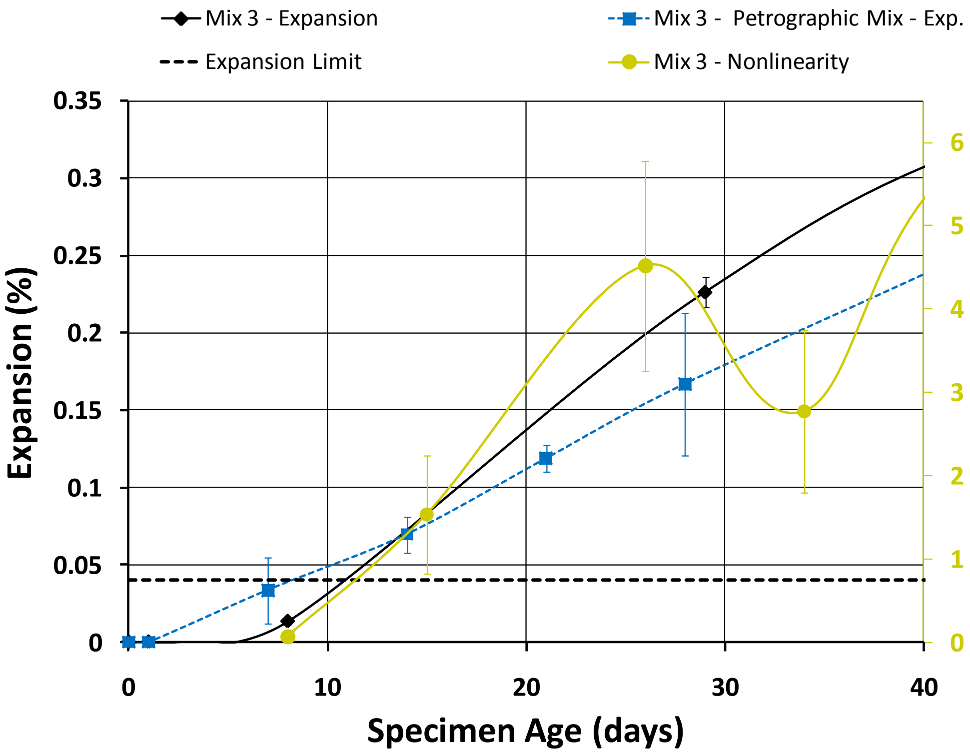

Figure 8.19. Comparison of expansion and nonlinearity results for Mix 3.

The first petrographic images for the recast Mix 3 samples were taken at seven days and the results showed a small amount of staining around some fine aggregates (Las Placitas is used as the fine aggregate), shown in Figure 8.20, but overall little fluorescence.

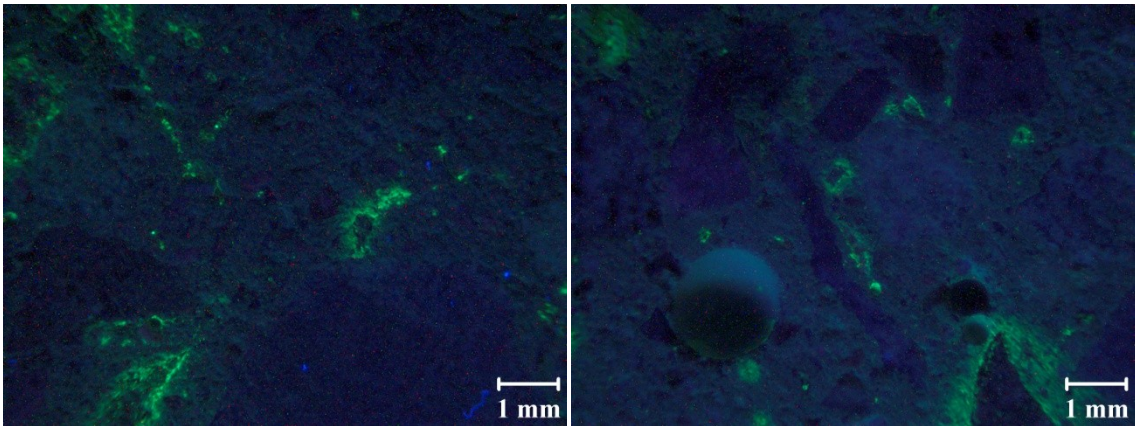

Figure 8.20. Petrographic images for Mix 3 at 7 days.

At later ages there is a general progression of more common fluorescence and development of microcracks in the sample. Figure 8.21 shows the results at 14 days, where generally there is more fluorescence. Figure 8.22 shows the results at 35 days where the fluorescence is frequent and gel filled microcracks are highlighted by the stain.

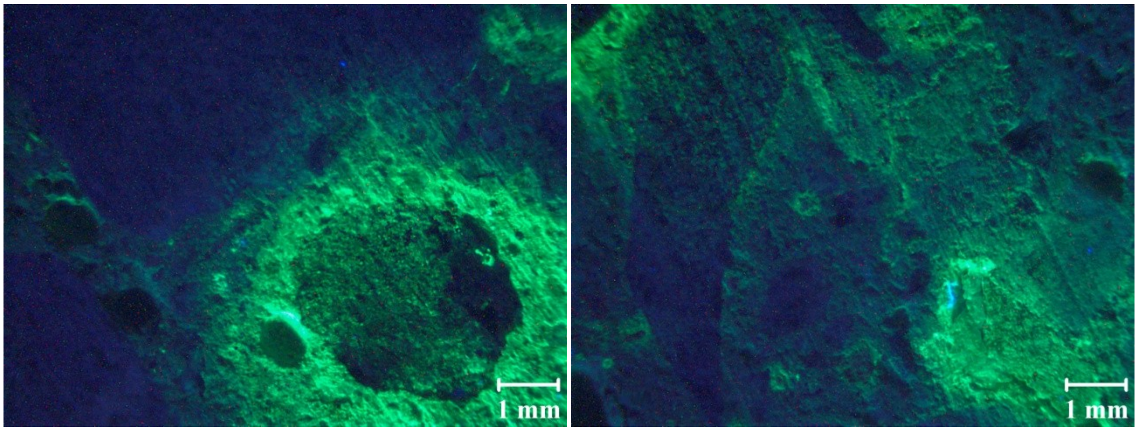

Figure 8.21. Petrographic images for Mix 3 at 14 days.

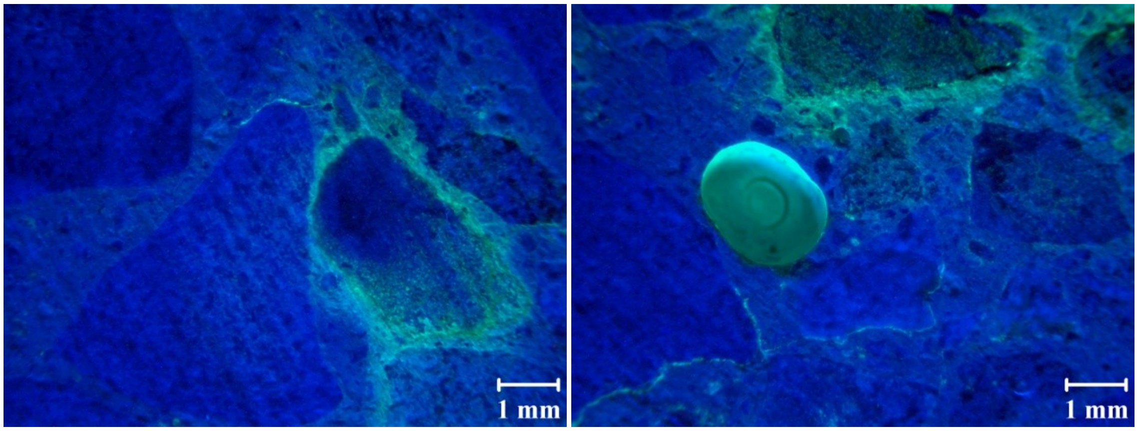

Figure 8.22. Petrographic images for Mix 3 at 35 days.

8.5.3 Sample Characterization for Mix 4

As mentioned earlier, Mix 4 had been recast to gather nonlinearity data for the early ages since this mixture had been originally cast before the development of a nonlinear measurement setup. In addition to gathering nonlinear data, expansion measurements were also collected for these samples and petrography was performed regularly. The expansion and nonlinearity results for the petrographic mix are shown together in Figure 8.23 along with the expansion results from the originally cast Mix 4.

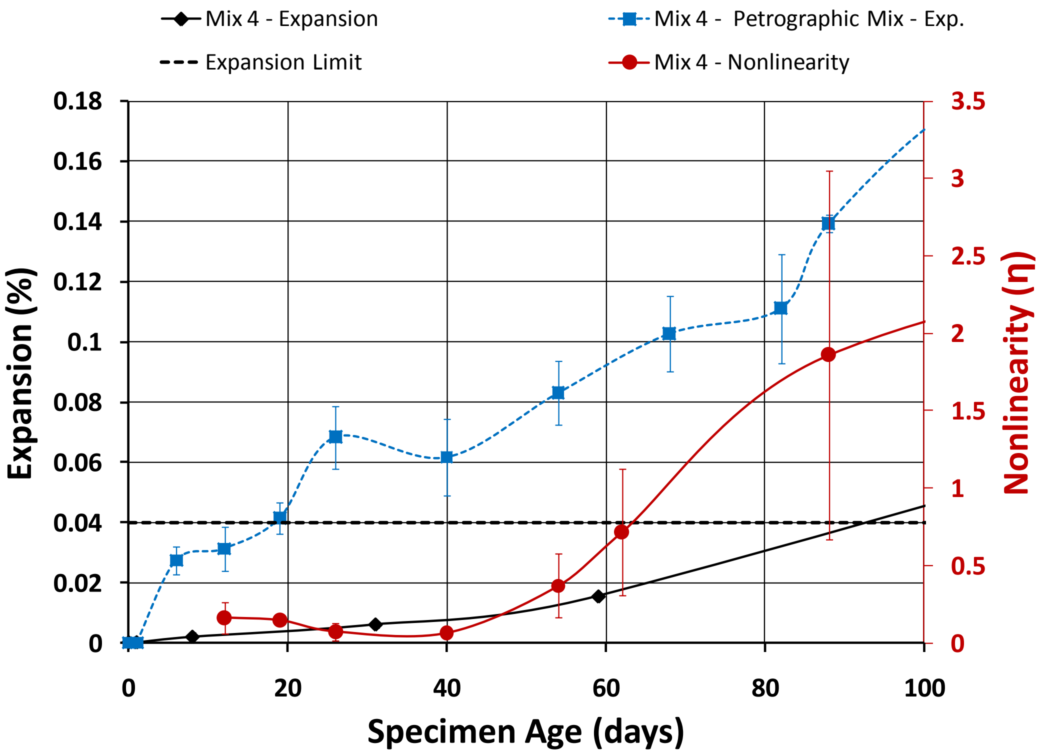

Figure 8.23. Comparison of expansion and nonlinearity results for Mix 4.

The results show that the recast Mix 4 has considerably higher expansion rate, crossing the limit at only 20 days while the originally cast mixture crossed at about 95 days. For the nonlinearity measurements, the nonlinearity starts to develop at around 50 days. At 12 days, besides a small amount of light staining of the paste, there is no fluorescence, shown in Figure 8.24. At 19 and 26 days, overall there is little fluorescence but there are a few instance of fluorescence shown in Figure 8.25.

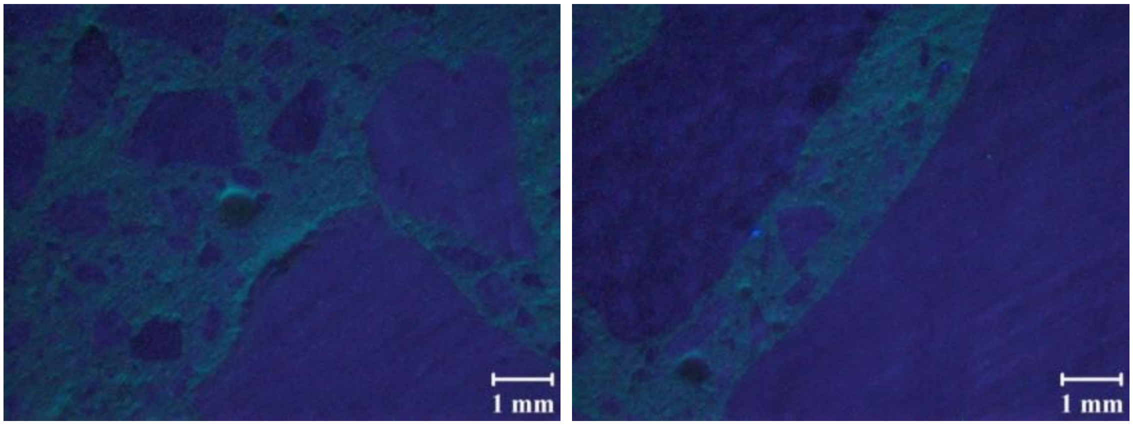

Figure 8.24. Representative images for recast Mix 4 at 12 days.

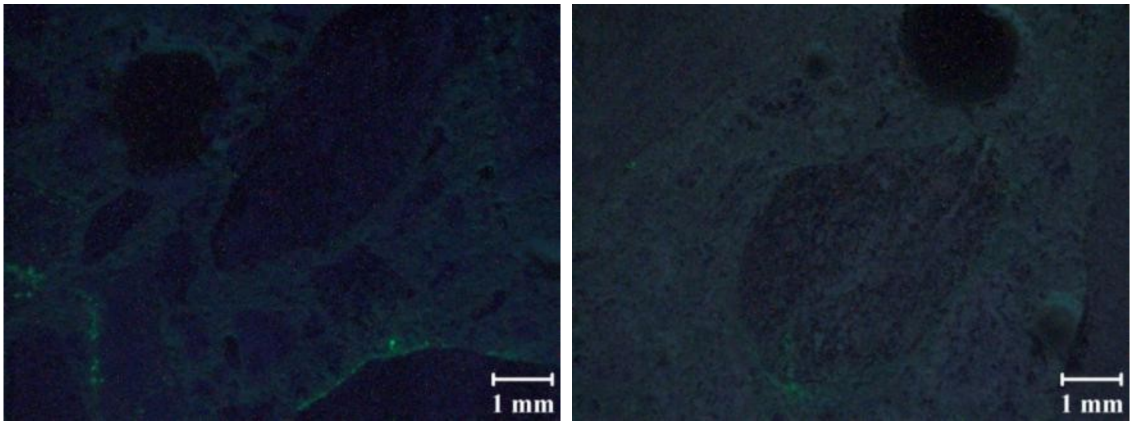

Figure 8.25. Representative images for recast Mix 4 at 26 days.

At 40 days there is still little fluorescence in the sample and only a few instances are found, shown in Figure 8.26. These results are not consistent with expansion results since much larger amount of fluorescence is expected once the expansion limit is crossed. Note the nonlinearity remains low for these ages. At 54 days there is significantly more fluorescence but the fluorescence appears inside the aggregates, which was not observed in other aggregates previously tested. It is around this time that nonlinearity starts to increase. At 62 days the fluorescence is even more common and consistent with the increase in nonlinearity.

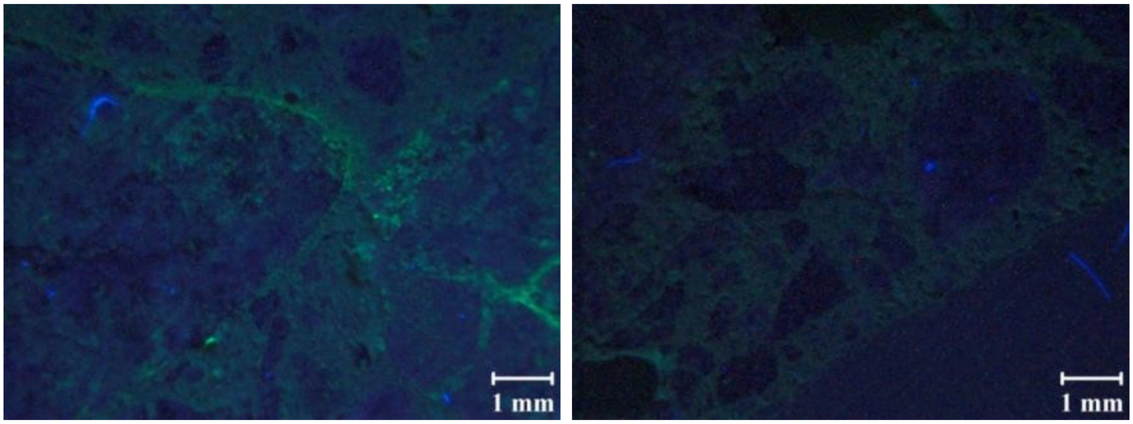

Figure 8.26. Representative images for recast Mix 4 at 40 days.

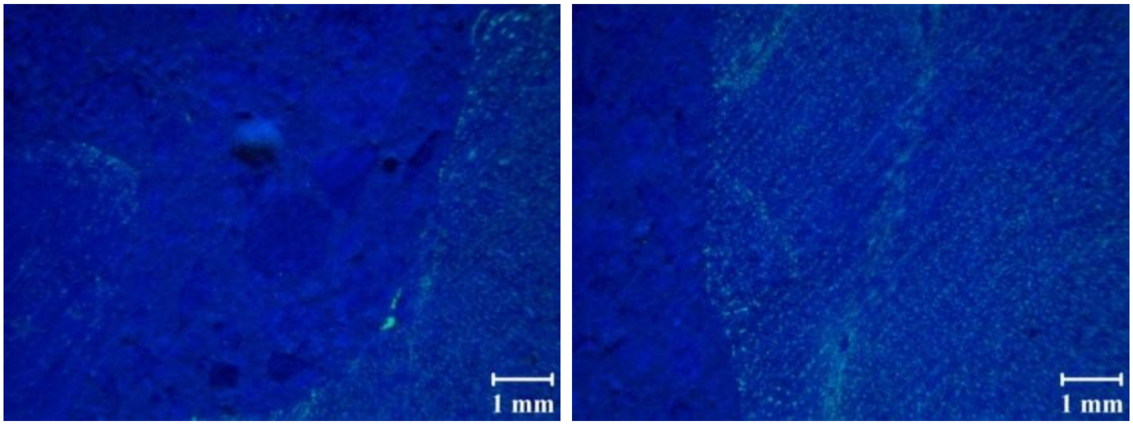

Figure 8.27. Representative images for recast Mix 4 at 54 days.

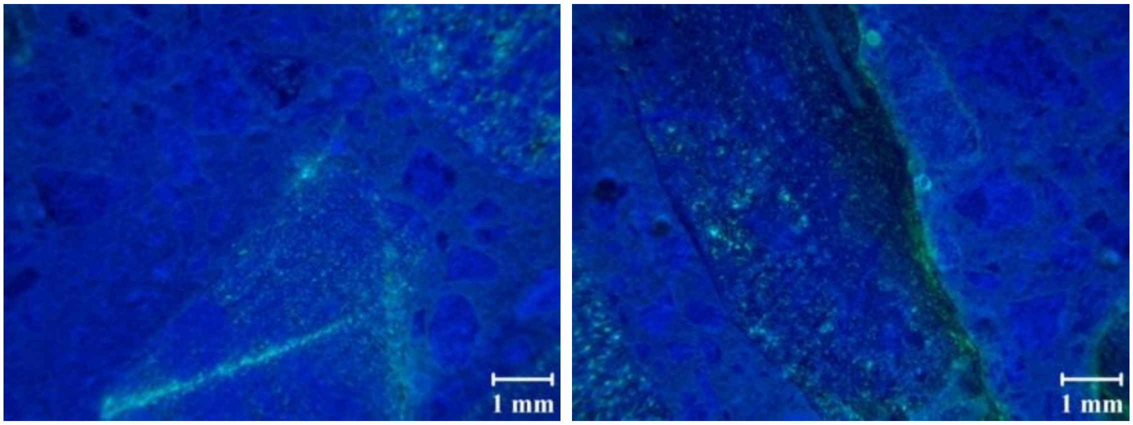

Figure 8.28. Representative images for recast Mix 4 at 62 days.

The results for the recast Mix 4 are not consistent with the expansion trend previously recorded and the staining does not illuminate clear reaction rims as seen with the Las Placitas aggregate.

8.5.4 Sample Characterization for Mix 5

The results for the petrographic Mix 5 batch are also strange, shown in Figure 8.29. The nonlinearity and expansion for the original Mix 5 batch are in general agreement, where the expansion limit is crossed as the nonlinearity starts to increase. The expansion for the petrographic batch does not cross the expansion limit during the entire test duration and the petrography shows some fluorescence, first witnessed at about 30 days, which is largely on the interior of aggregates and no reaction rims.

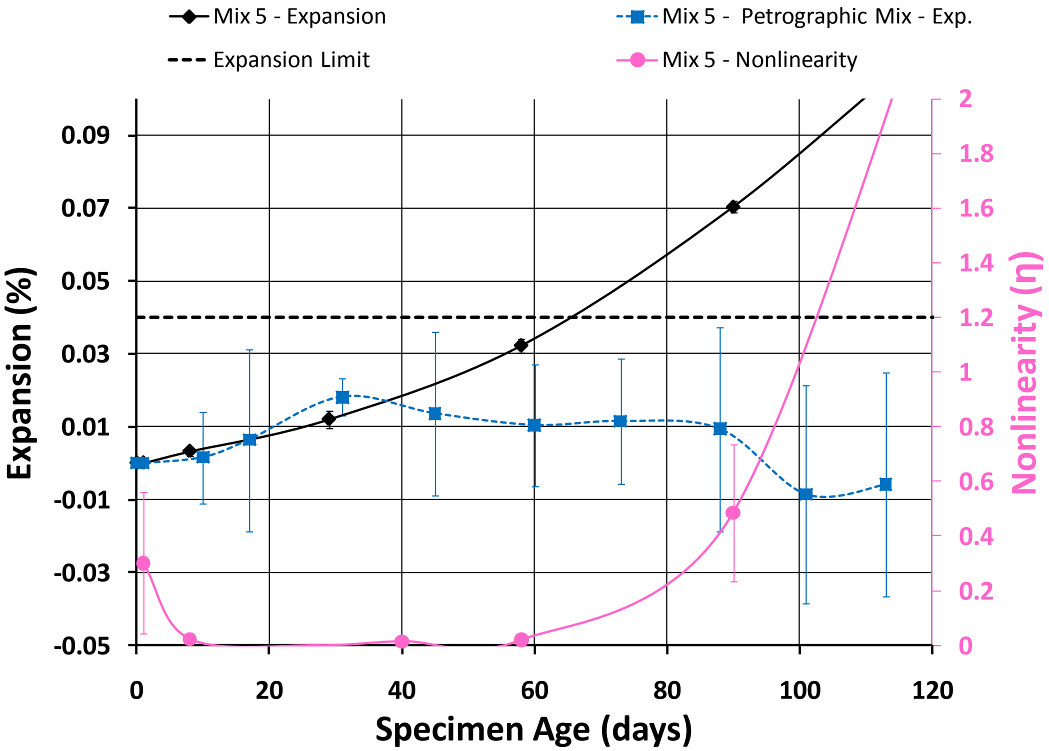

Figure 8.29. Comparison of expansion and nonlinearity results for Mix 5.

Figure 8.30 shows the small amount of staining encountered at 30 days and Figure 8.31 shows a similar result at 59 days.

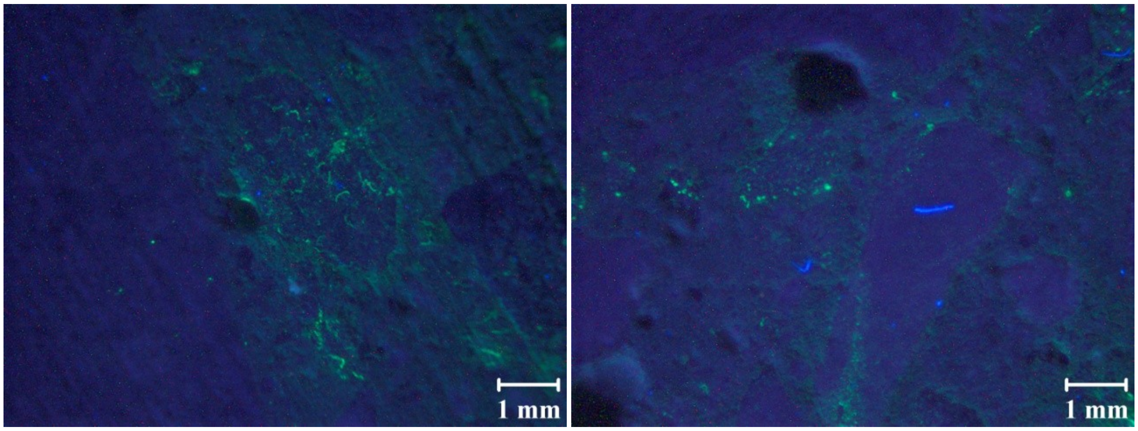

Figure 8.30. Petrographic images for Mix 5 at 30 days.

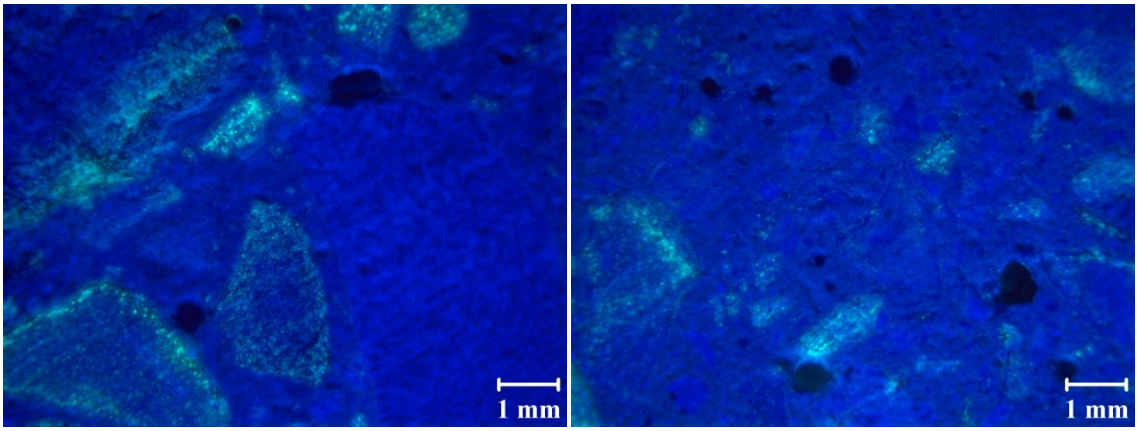

Figure 8.31. Petrographic images for Mix 5 at 59 days.

8.5.5 Sample Characterization for Mix 7

Petrography was also performed on Mix 7 at 218 days, after the expansion limit has been crossed. The results, shown in Figure 8.32, show some staining of certain aggregates but there is no evidence of reaction rims or cracks in the representative slice. This technique was also applied to the reference Mix 7 to compare results. The results for the reference mix are shown in Figure 8.33 and when compared to Figure 8.32 there is not much difference. This petrographic examination does not provide evidence of ASR, which confirms the nonlinearity results but contradicts expansion results. Although further investigation is still necessary, these results suggest that measures of nonlinearity are more accurate for assessing propensity for ASR in aggregates than the traditional expansion measurements, which capture dimensional change under aggressive conditions regardless of source. Even though there is agreement in both techniques for the nonreactive mixtures, Mixes 1 and 6, further investigation may be warranted since the results are close to the limit. While the average value for Mix 6 does not cross the limit, the standard deviation shows that the expansion of at least one sample did cross the limit. There is no such ambiguity in the nonlinearity results; the nonlinearity has remained very close to zero throughout the entire test duration.

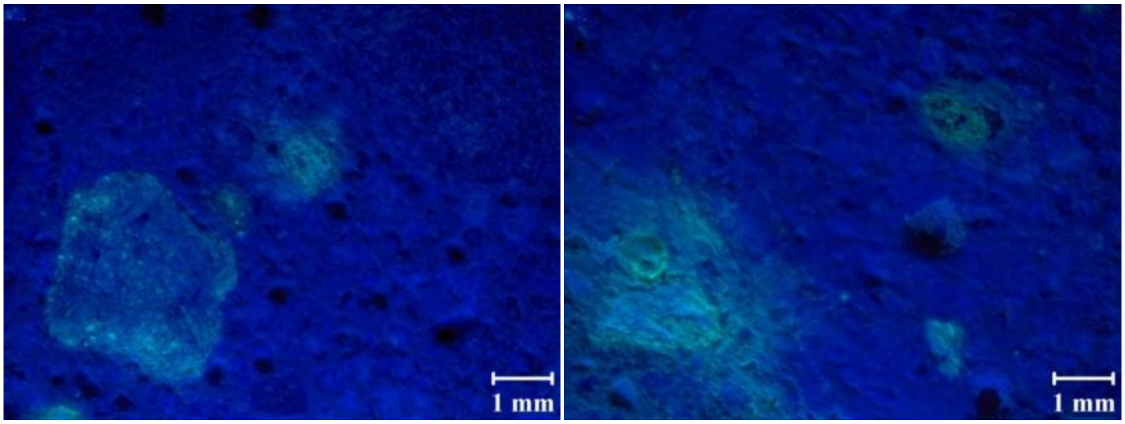

Figure 8.32. Representative images for Mix 7 at 218 days.

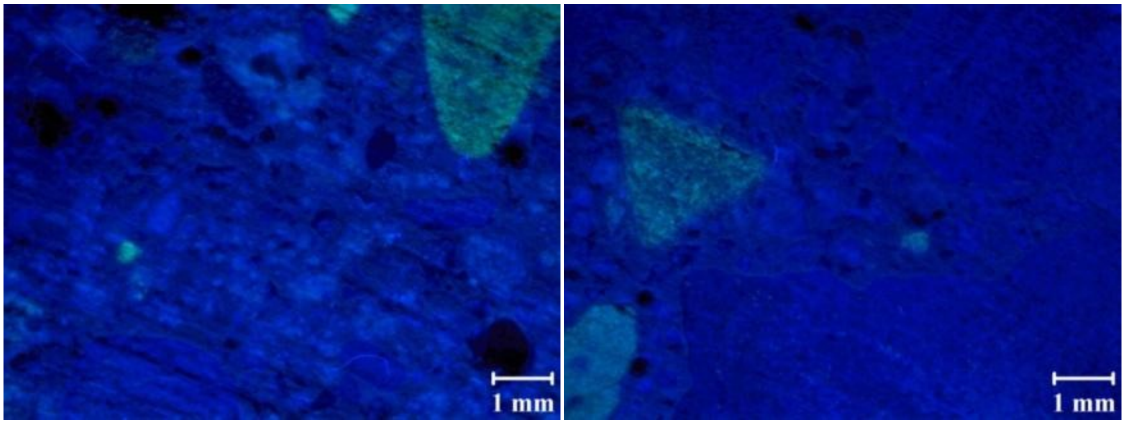

Figure 8.33. Representative images for reference Mix 7 at 218 days.

8.5.6 Sample Characterization Conclusions

These results illustrate the utility of the staining method for identifying ASR gel within a sample. The technique can highlight features within the sample not readily apparent with standard optical examination. Cracking, reaction rims, and ASR gel is clearly illuminated with the uranyl acetate. However, the results are not conclusive in all cases. For mixtures containing aggregate from Las Placitas, NM, stained reaction rims are clearly observed. For Spratt samples the results are not that clear and it appears that mineralogy plays a role in the applicability of this staining technique. The results of this limited study are presented in Table 8.2. The approximate age of detection for expansion is the time expansion crosses the threshold of 0.04% and for nonlinearity when the value first exceeds 0.2 (ignoring nonlinearity measured after demolding if applicable).

Table 8.2. Sample characterization summary.

Mix #	**Reactivity**		**Approximate Age of Detection**		**Sample Characterization**
	Based on Expansion	**Based on Nonlinearity**	**Expansion (Days)**	**Nonlinearity (Days)**	
2	Reactive	Reactive	19	8	N/A
2 recast	Reactive	N/A	13	N/A	• Clear reaction rims at 9 days for certain aggregates • More frequent and larger rims at later ages
3	Reactive	Reactive	11	9	N/A
3 recast	Reactive	N/A	8	N/A	• Some staining at 7 days, overall little fluorescence • More common staining at 14 days • Progression of ASR seen at 35 days with frequency staining and stained microcracks
4	Reactive	Reactive	93	137*	N/A
4 recast	Reactive	Reactive	19	48	• Small amount if fluorescence first seen at 26 and later at 40 days • Significantly more fluorescence at 54 days and more frequent at 60 days • No clear reaction rims • Most fluorescence inside aggregate
5	Reactive	Reactive	65	78	N/A
5 recast	Nonreactive**	N/A	--	N/A	• Some fluorescence at 30 days with similar result at 59 days • No clear reaction rims • Most fluorescence inside aggregate
7	Reactive	Nonreactive	145	--	• No indication of ASR activity • No reaction rims • Light surface staining of certain aggregates for both CPT and reference samples

*Data before this age is unavailable

**Based on available data

CHAPTER 9

CONCLUSIONS AND RECOMMENDATIONS

This research has shown that the nonlinear measurement technique is a viable method for damage characterization in concrete specimens. NIRAS measurements have shown a clear distinction between highly reactive and nonreactive concrete mixtures. For highly reactive mixtures, there is some evidence of possibly earlier detection of ASR related damage using this technique. In addition, there are indications that the technique is sensitive to other changes within the concrete caused by hydration. Additionally, the NIRAS measurement setup has proven to be a robust and accurate measurement technique. The variability between successive measurements has been shown to be less than 20 percent and even less than 10 percent with a prepared adhesion surface. NIRAS has proven to be a powerful NDT tool to rapidly detect microcrack-type damage (regardless of the cause) in concrete in an early stage of the material degradation.

In general, expansion measurements had shown a higher rate of expansion with highly reactive fine aggregate than with coarse aggregate. The nonlinearity measurements, however, did not appear to be affected by the gradation and can be used to evaluate aggregates as-received, eliminating the need for the time consuming grading process. While the expansion measurements can be used to identify a highly reactive aggregate, results close to the expansion limit are ambiguous and a conclusive statement cannot be made about their level of reactivity. In contrast, the nonlinearity measurements for the samples near the expansion limit have shown negligible nonlinearity, indicating no presence of ASR damage. For example, Mix 7 crossed the expansion limit but remained close to the limit for the duration of the test, while nonlinearity has remained close to zero and sample characterization did not provide evidence of ASR. Also, Mix 1 and Mix 6 have come close to the expansion limit without crossing it, while nonlinearity has remained negligible throughout the entire test. While it remains to be proven that measures of nonlinearity are an accurate indication of damage, the results have been more consistent than measures of expansion. Specifically Mix 4, when recast, showed a completely different expansion but the level of nonlinearity was similar to what was measured previously.

Staining of the concrete samples with uranyl acetate was used in order to attempt to confirm the presence of ASR gel and cracking within the samples. These experiments have shown that formation of characteristic reaction rims around aggregates did correlate with increases in both expansion and nonlinearity. However, spurious and anomalous staining complicates the interpretation of results. For Mix 7, which has crossed the expansion limit but nonlinearity has remained close to zero, both the CPT sample and reference sample have staining but nothing that resembles reaction rims, suggesting that the expansion may not be an accurate measure of reactivity. Further work needs to be done with this technique in order to assess the relation between microstructural changes and changes in nonlinearity, but this research has shown that the technique has potential to be a powerful NDE technique.

Based on the results presented in this research it is recommended to apply this technique more broadly across a wide variety of materials to gain further understanding of the significance of the nonlinearity parameter, since the developed technique is conducive to laboratory specimens. The test setup is relatively simple and inexpensive which can facilitate its application across various research laboratories for comparison of results. Finally, in addition to answering many questions, this research has raised questions which leave opportunities for future work with this topic, discussed in the closing chapter.

CHAPTER 10

QUESTIONS AND FUTURE WORK

10.1 Slow Dynamics

An area not addressed in this research concerns the additional phenomena of slow dynamics. In addition to amplitude dependent resonance frequency shifts, hysteretic media has also been known to exhibit a memory effect. In other words, the response of the specimen is dependent on the loading history of the material. Previous research has shown that hysteretic materials have decreased elastic modulus after excitation and require time to recover to the original state before testing [50-54]. In this research it has been observed that this effect is also seen for nonlinear parameter measurements. Testing of the samples with a permanent screw attachment consistently shows that the first measurement always yields a higher nonlinear parameter. Also, the subsequent measurements have very small variability as shown in Figure 10.1,

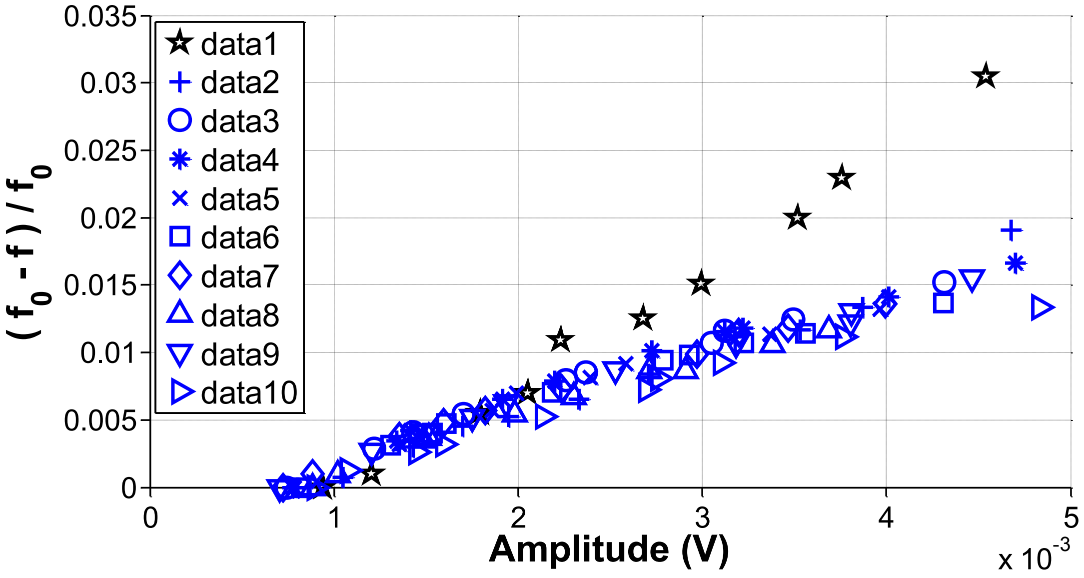

Figure 10.1. Slow dynamics in nonlinear parameter measurements.

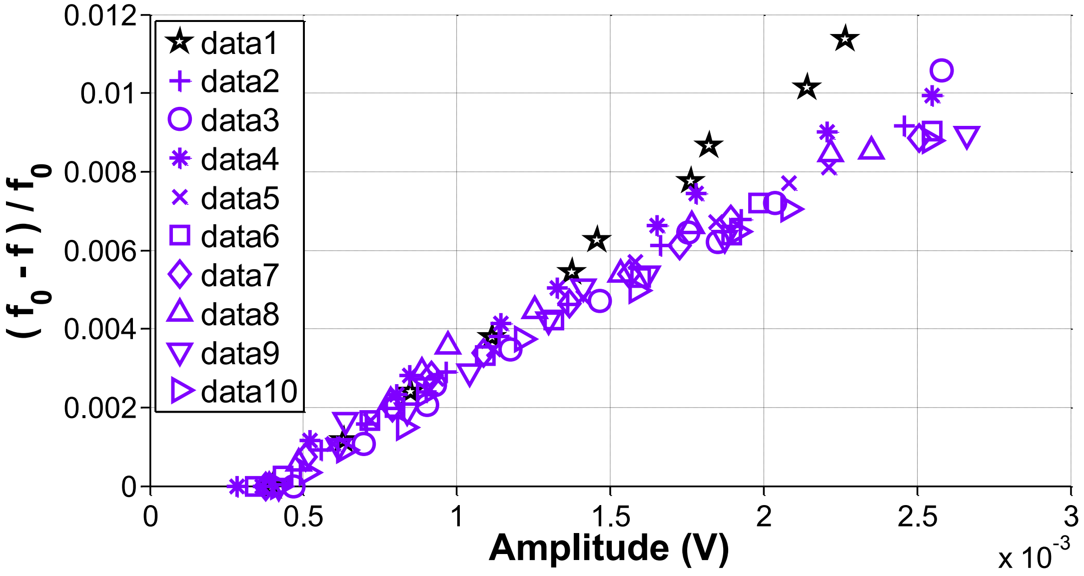

Figure 10.2. Smaller slow dynamics effect for lower amplitudes.

When the maximum amplitude of excitation is decreased, this effect is significantly smaller, as seen in Figure 10.2. This is consistent with previous research which has shown that slow dynamics can be avoided with low amplitude excitation. Further research is still necessary to establish the significance of this phenomenon and the results show that great care must be taken with nonlinearity measurements as other attributes of hysteretic material behavior can affect results.

10.2 Application of NIRAS to Other Forms of Damage

NIRAS has proven to be an effective testing technique to discern ASR potential in aggregates but it also holds potential for examining other forms of damage as well as examining effects of other reactions within concrete. The results have shown that NIRAS is sensitive to nonlinearity present in concrete after one day of curing which continually decreases with time. This effect has been attributed to the hydration process in concrete which is associated with strength gain in concrete. Research could be conducted using this technique to study the impact of different mixture designs on the hydration process of concrete. Further, since NIRAS appears to be sensitive to hydration, self-healing in cementitious systems could also be studied.

Due to the simplicity of the test setup and equipment, NIRAS can be readily applied to a wide variety of materials which exhibit hysteresis. The complicated nature of ASR makes it difficult to relate changes in nonlinearity to specific microstructural changes and it may be useful to apply NIRAS to a sample which has damaged induced in a more controlled manner.

10.3 Thorough Petrographic Survey

Further understanding of the alkali-silica reaction and the nonlinearity parameter can be achieved by continuing the work using experienced petrographers and a thorough survey of aggregate sources of varying mineralogy. A question that remains to be answered is the eventual decrease of the nonlinearity parameter at later stages of the CPT test, since the models used are phenomenological and have not yet been directly related to microstructural features. Thorough petrographic investigation could prove the postulated explanation of this phenomenon (the growth of cracks past a certain critical size contribute less to nonlinearity). In this petrographic examination, other techniques for gel identification could also be explored in order to simplify the examination.

Image analysis could also be performed in order to estimate crack density and determine if there is a relation with the easily measurable nonlinearity parameter. There are various image analysis techniques that can be investigated. Different weightings for certain features can be used to determine what features are most influential in determining nonlinearity and the impacting the nonlinearity parameter.

10.4 Finite Element Simulation

Development of a finite element model for simulation could prove useful in determining the type of features that affect the magnitude of nonlinearity. This would however require modeling the highly complex and statistically variable microstructure of concrete. The simulation results can then be compared to petrographic work to test the model. If there is convergence between the model and simulation, the effects of crack sizes can be easily tested using the simulation. However, this type of modeling may be too complex. Some alternatives include assuming the concrete is homogenous and using nonlinear equations of wave motion or modeling cracks as a unique element which behaves differently based on the amplitude of excitation, similar to the Preisach-Mayergoysz (PM) approach [11, 55].

10.5 Structural Health Monitoring

While the developed techniques work well in laboratory settings and can be effectively used for preventive screenings, future work could expand this technique to be applied to real structures for eventual structural health monitoring. For real structures, the current technique could still be used to examine concrete cores, which are routinely examined by petrography to determine the state of the structure. However, petrographic analysis of cores can be very time consuming, expensive, and often subjective. NIRAS offers rapid and non-subjective results.

Structures in the field are continually excited by complex loading cycles. Despite the possible complexity of the excitation it may be possible to isolate and measure one or more of these modes. Since the loading changes in intensity, the change in frequency of the isolated mode with changing intensity can be used as a parameter that relates to the damage state of the structure. Since it is difficult and can be dangerous to excite large civil structures in resonance, exploiting the natural vibration of the structure to determine its health state would be ideal. With this in mind, using instantaneous frequency may be the optimal approach for structural health monitoring.

10.6 Further Work with Instantaneous Frequency Analysis

The results in this research have not shown that there is a frequency change within a single recorded impact signal, as described in Appendix B. However the results do not completely rule out this possibility. Additionally, research has been done by other investigators demonstrating this effect in other materials. Van Den Abeele et al. have developed a technique termed Nonlinear Reverberation Spectroscopy (NRS) and have shown very small changes in frequency for composite laminate samples (less than 1 Hz) [56]. In this technique the sample is excited at a single frequency near resonance for a sufficiently long period of time to reach steady state. After steady state is reached, the excitation is stopped and the reverberation signal is recorded. This signal is averaged and a complicated signal processing technique is applied. At its core, this technique relies on successive fitting of an exponentially decaying sinusoid function to small time intervals of the reverberation signal. However, Van Den Abeele et al. warn that this technique can only be applied to materials with low attenuation (which would not include concrete) [56]. Van Den Abeele et al. have also applied a similar technique to reinforced concrete beams [22]. The "nonlinear time domain method" has the same sort of excitation as NRS but the function is only fitted to the initial portion of the signal, down to 90% (to avoid nonlinear and slow dynamics effects), and changes in frequency are examined as excitation amplitude is increased [22]. This technique is actually more similar to NRUS and NIRAS and does not look at instantaneous frequency but the results showed that the different methods do not yield the same results quantitatively [22].

Since the impact response of the samples in this research are similar to the reverberation signals, an instantaneous frequency analysis using fitting tools built into Matlab ® was attempted. Two separate fitting methods were applied to signals from a highly nonlinear sample (based on NIRAS results). The first technique applied fitting of an exponentially decaying sinusoid to a moving window along the signal. The second technique applies fitting of the entire signal to a more complicated function,

$$\exp\left(\left(a_0 + a_1 t + a_2 t^2 + \ldots\right)\cdot t\right)\cos\left(\left(b_0 + b_1 t + b_2 t^2 + \ldots\right)\cdot t + \phi\right) \qquad (10.1)$$

When applied to a simulated chirp signal both techniques convey accurate results. When applied to the experimental signals, the results from both techniques are qualitatively similar but do not show the same dependence on of frequency with time. The fitting using windows appears to be dependent on the size of the window, which was not the case with the simulated signal. Figure 10.3 shows the frequency change with time and Figure 10.4

shows the frequency change with amplitude (where the amplitude is the maximum amplitude of the windowed portion of the signal in the frequency domain).

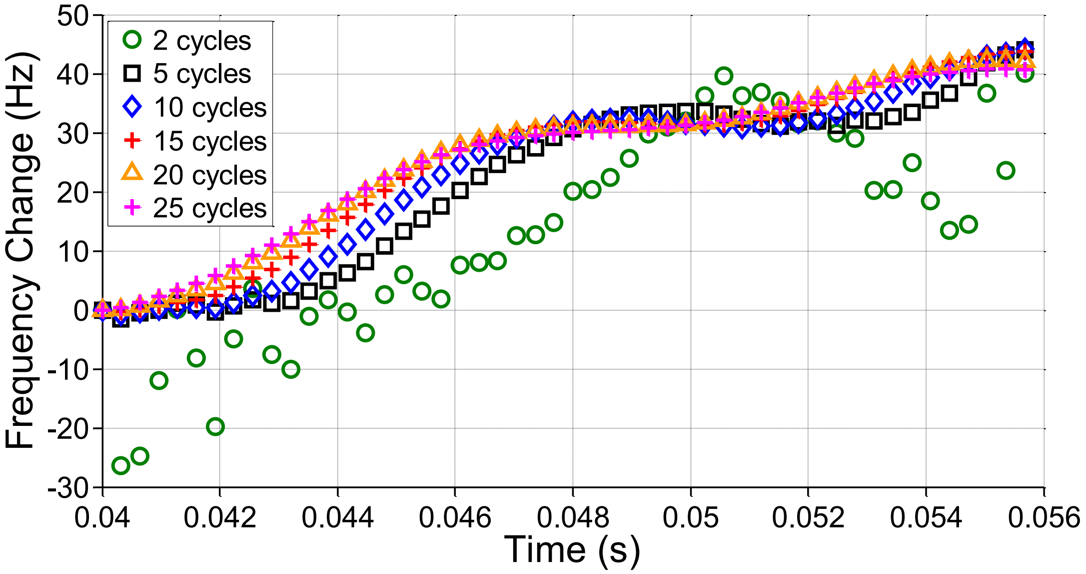

Figure 10.3. Frequency change with time using window fitting.

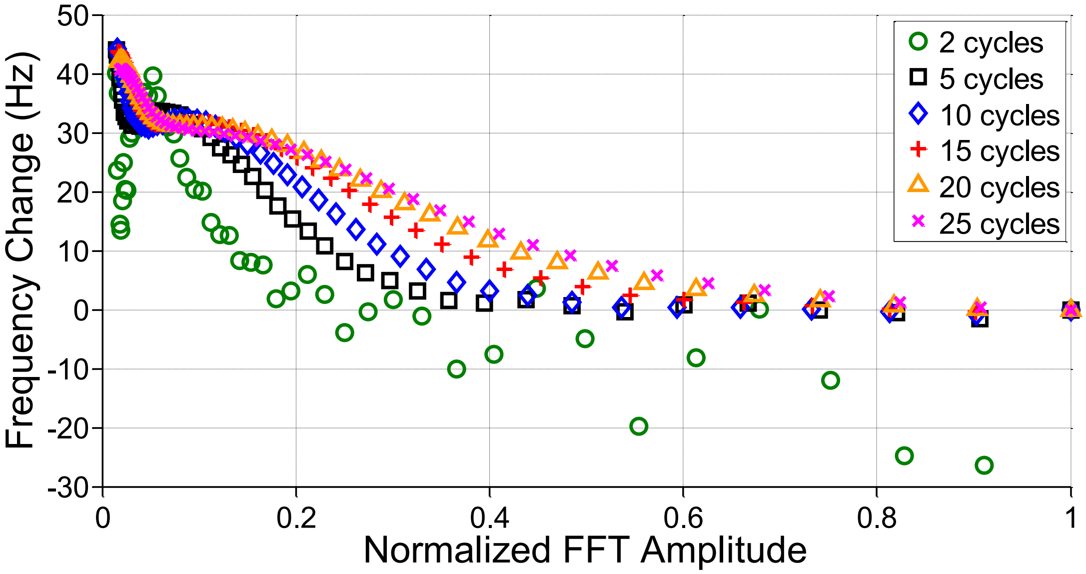

Figure 10.4. Frequency change with amplitude using window fitting.

The results show a complicated relation between instantaneous frequency change and amplitude.

The second technique applies fitting of one function to the entire signal. Figure 10.5 shows the results when the overall function is fitted to the following function,

$$\exp\left(\xi(t)\cdot t\right)\cos\left(2\pi\cdot f(t)\cdot t+\phi\right) \tag{10.2}$$

where

$$\begin{aligned} \xi(t) &= \xi_0+\xi_1 t \\ f(t) &= f_0+f_1 t \end{aligned} \tag{10.3}$$

is termed a linear relation,

$$\begin{aligned} \xi(t) &= \xi_0+\xi_1 t+\xi_2 t^2 \\ f(t) &= f_0+f_1 t+f_2 t^2 \end{aligned} \tag{10.4}$$

is termed a quadratic relation,

$$\begin{aligned} \xi(t) &= \xi_0+\xi_1 t+\xi_2 t^2+\xi_3 t^3 \\ f(t) &= f_0+f_1 t+f_2 t^2+f_3 t^{3\,4} \end{aligned} \tag{10.5}$$

is termed a cubic relation and,

$$\begin{aligned} \xi(t) &= \xi_0+\xi_1 t+\xi_2 t^2+\xi_3 t^3+\xi_4 t^4 \\ f(t) &= f_0+f_1 t+f_2 t^2+f_3 t^3+f_4 t^4 \end{aligned} \tag{10.6}$$

is termed a 4th order relation. Figure 10.5 shows that the results do not converge after the 4th order relation but are nonetheless close to linear. The amount of frequency shift is also comparable to the results shown in Figure 10.3.

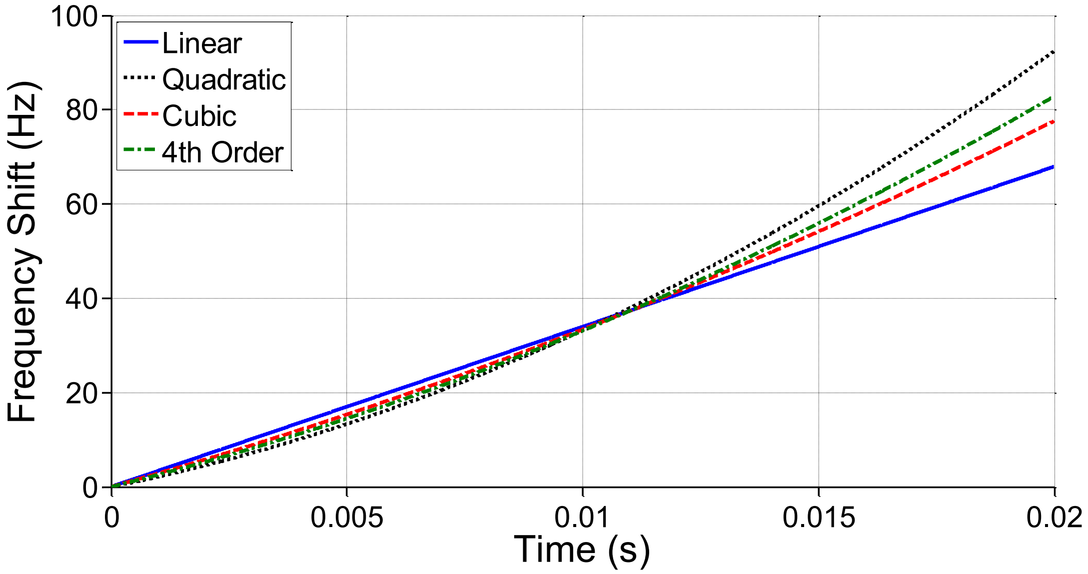

Figure 10.5. Frequency change with time using overall fitting.

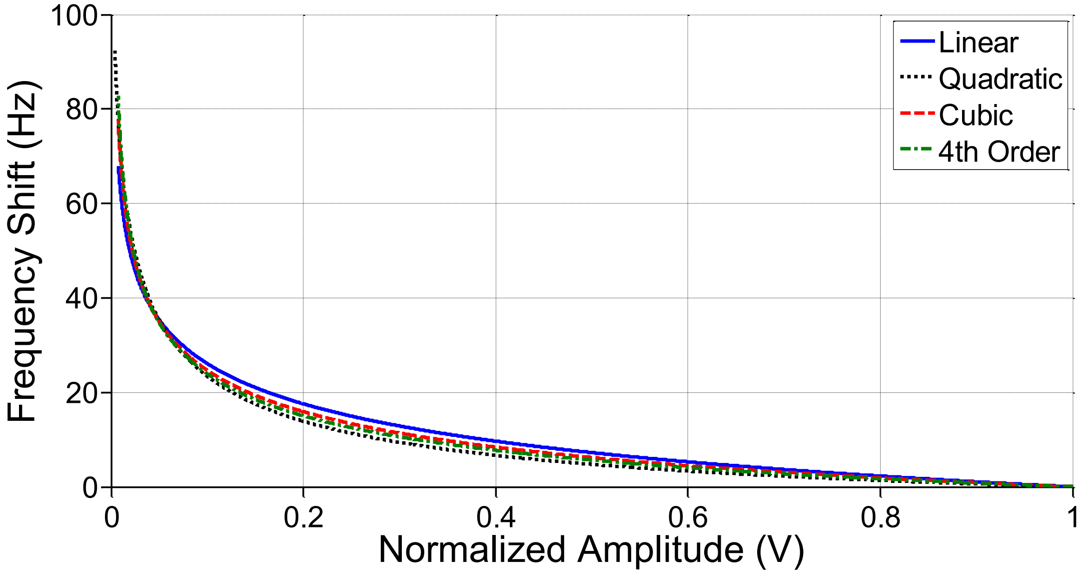

Figure 10.6. Frequency change with amplitude using overall fitting.

The results shown in Figure 10.5 and Figure 10.6 are for the highest amplitude impact signal. Figure 10.7 shows that the results converge on a linear dependence of frequency with time for lower amplitude impact signals and, since the amplitude decays exponentially, an exponential relation of frequency change with amplitude. Also, notice that the maximum instantaneous frequency change is also smaller for a smaller impact excitation.

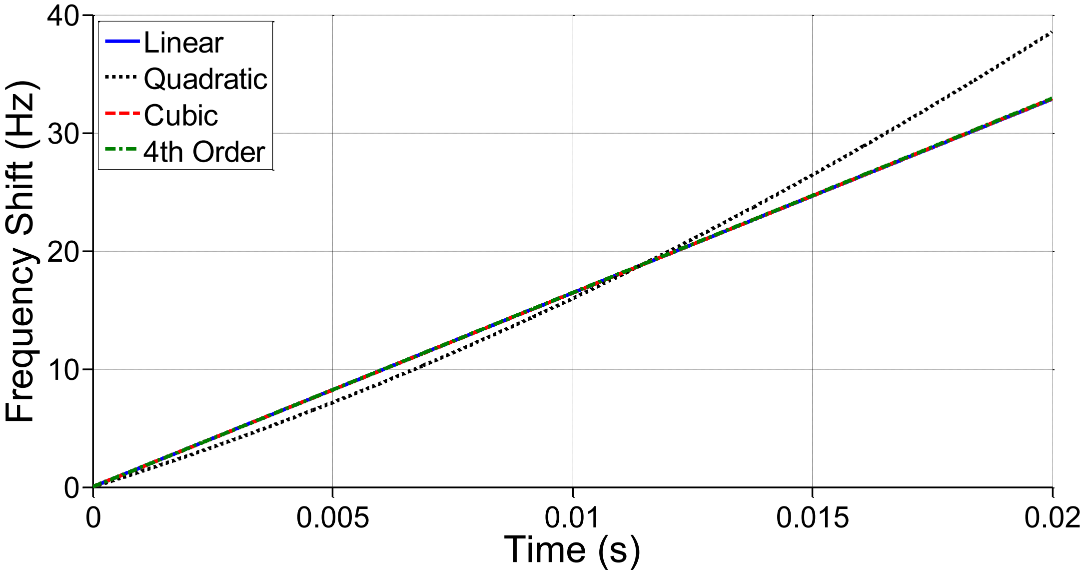

Figure 10.7. Frequency change with time using overall fitting for lower amplitude excitation.

These preliminary results show that there is some indication of measurable instantaneous frequency change within a single impact response signal. Qualitatively both techniques have yielded similar results but the quantitative discrepancy has not been resolved. It is speculated that noise carried in an experimental signal and transient impact effects have a more profound effect on the windowing technique. This issue could be resolved by averaging several impact signals before analysis. Of course, this would require the development of a test setup that can consistently deliver the same impact load. It may be worthwhile to build on these techniques to develop this measurement technique since it holds potential for faster testing. Further, this technique could potentially be used to exploit natural vibrations of structures for structural health monitoring.

APPENDIX A

BEATING SIGNALS

One interesting phenomenon encountered in the recorded experimental signals is that of a beating signal. This term is given to a signal which is a combination of harmonics with frequencies which are very close to each other [39]. Following the derivation of Ginsberg, the summation of harmonics with the same amplitude but different frequencies is given as [39],

$$u = 2A\cos(\Delta_\omega t - \Delta_\phi)\cos(\omega_{av} t - \phi_{av}) \tag{A.1}$$

where

$$\begin{aligned} \omega_{av} &= \frac{1}{2}(\omega_1 + \omega_2) \quad & \Delta_\omega &= \frac{1}{2}(\omega_1 - \omega_2) \\ \phi_{av} &= \frac{1}{2}(\phi_1 + \phi_2) \quad & \Delta_\phi &= \frac{1}{2}(\phi_1 - \phi_2) \end{aligned} \tag{A.2}$$

Since $\Delta_\omega < \omega_{av}$ the interpretation of the result is that the signal varies harmonically at the frequency ω_{av} with the amplitude of $2A\cos(\Delta_\omega t - \Delta_\phi)$. This causes a readily seen envelope of the signal which is seen in experimental data for certain specimens, for example in Figure A.1.

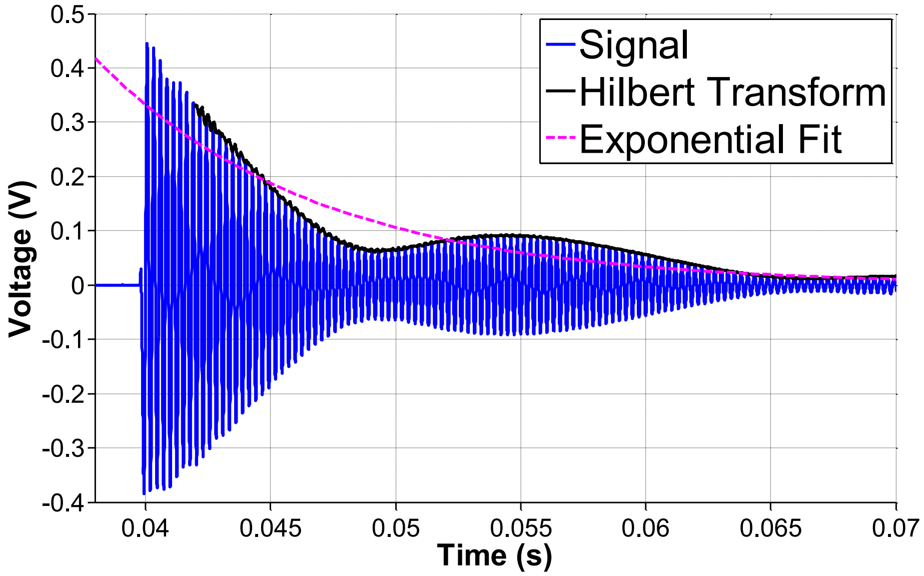

Figure A.1. Example of beating signal.

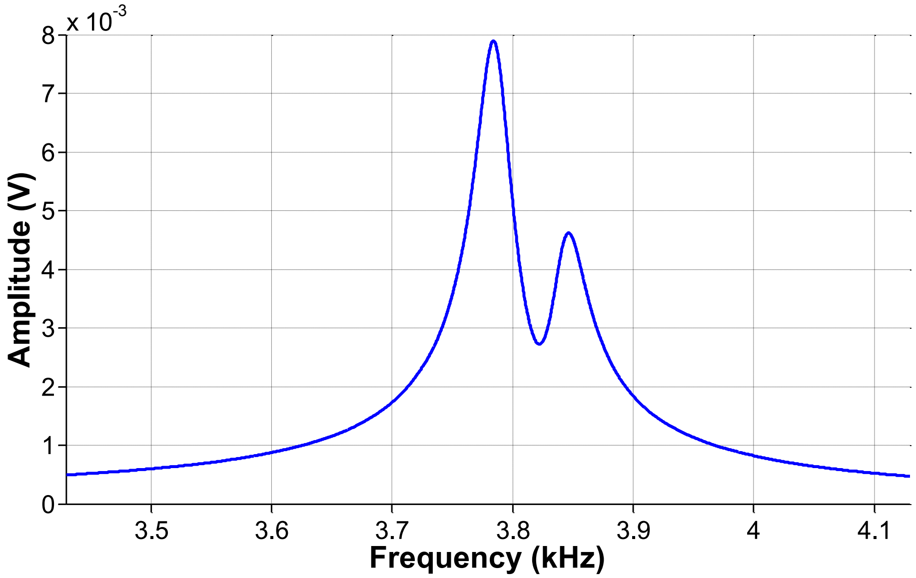

Figure A.2. Beating signal in frequency domain.

The frequency spectrum, Figure A.2, clearly shows two dominant frequencies very close to each other which results in the beating signal seen in Figure A.1. This presents a problem in approximating the envelope as well as determining the quality factor and as a result very difficult to extract the damping ratio from this type of data. The shift in resonance frequency however is relatively insensitive to this type of data since both peaks still shift in frequency when nonlinearity is present. While this appears to be similar to a resonance frequency peak splitting described in ASTM E 2001, two degenerate modes are not excited with the presented experimental setup [57]. It is postulated that this appears when there is rattling present in the specimen. This rattling could come from an aggregate which is fully debonded from the cement paste and vibrates close to the frequency of the specimen after impact excitation. This can actually be simulated by rattling of the accelerometer when there is bad coupling. When the magnet attachment is used it is possible to get rattling of the accelerometer which produces the same two peak phenomenon, Figure A.3 and Figure A.4. With the magnet attachment the two peaks can be eliminated by using vacuum grease as additional coupling between the washer and magnet (the washer is glued to the sample to provide a magnetic attachment).

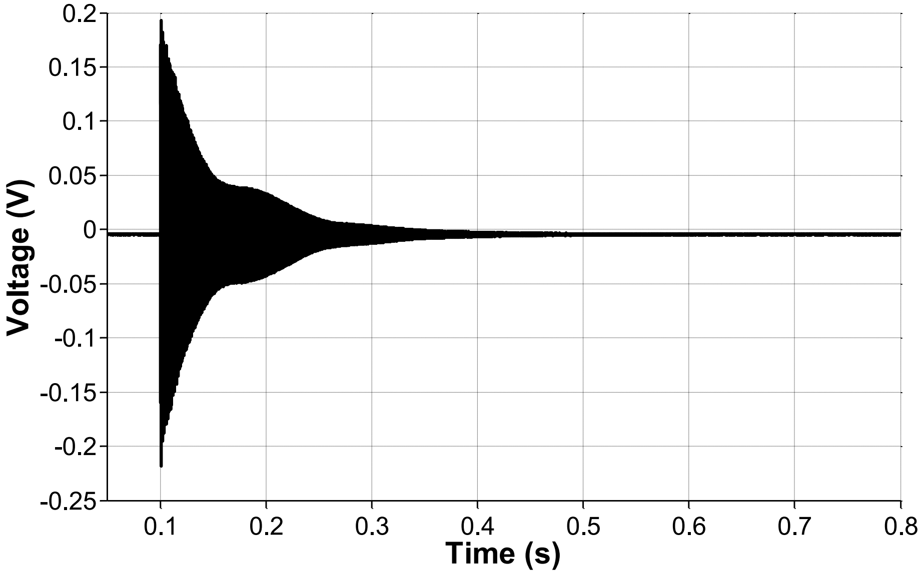

Figure A.3. Beating of signal for aluminum sample using magnet attachment.

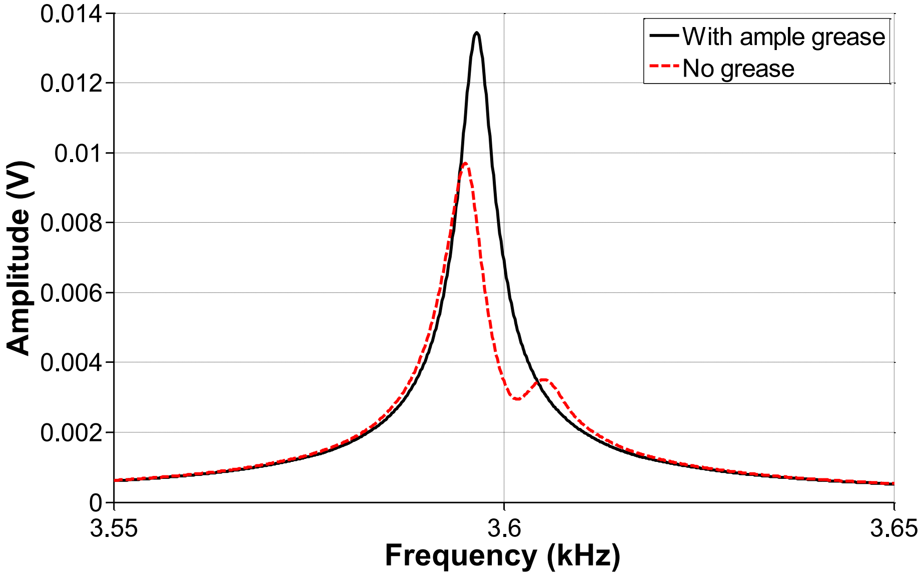

Figure A.4. Spectrum for vibration of aluminum using magnet attachment of accelerometer.

APPENDIX B

INSTANTANEOUS FREQUENCY

As described in Chapter 5 the Hilbert transform can also be used to calculate instantaneous frequency of a signal. This is accomplished by taking a derivative of the phase of the analytic signal at each time step. As an example, a linear chirp signal of 2 second duration was generated in Matlab that starts at 50 Hz and crosses 100 Hz at 1 seconds, shown in Figure B.1. The instantaneous frequency was calculated using the Hilbert transform and plotted as a function of time, shown in Figure B.2.

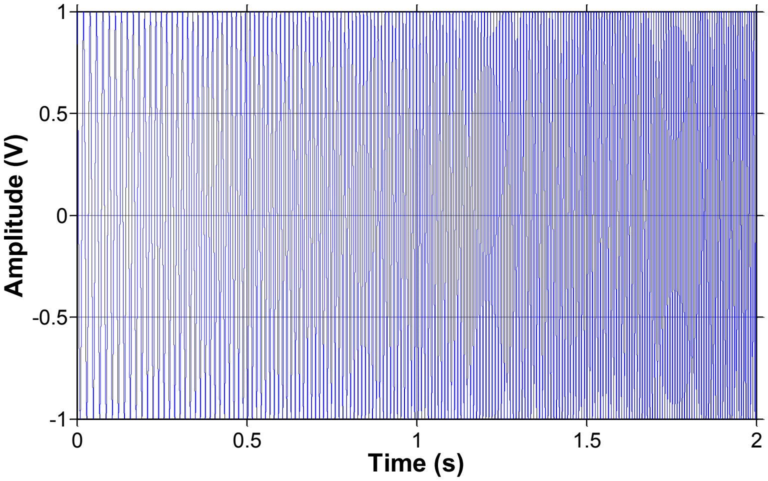

Figure B.1. Chirp signal created in Matlab.

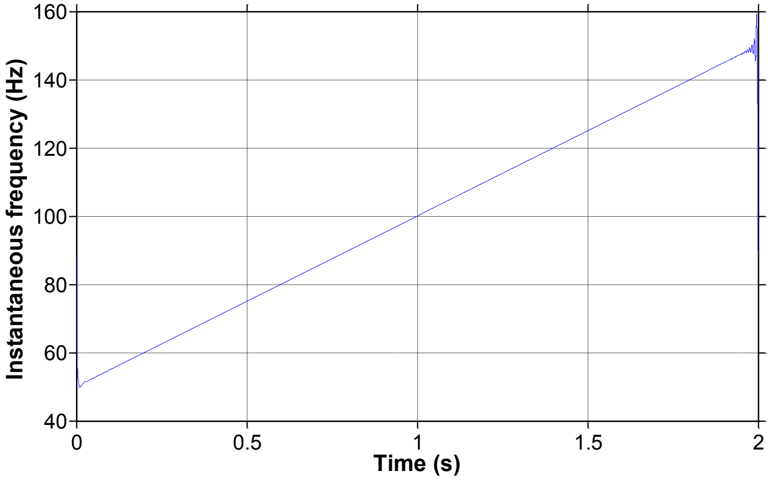

Figure B.2. Instantaneous frequency of chirp signal.

The instantaneous frequency calculated using the Hilbert transform clearly shows the linear change in frequency that starts at about 50 Hz and crosses 100 Hz at 1 second, as specified. Due to the exponential decay of the natural resonance vibration for the sample, it is conceivable that the instantaneous frequency changes in a nonlinear material as the oscillation is damped. For comparison to the results of a real signal, a simulated signal, similar to the real signal, was made in Matlab by creating a decaying chirp signal that linearly changes in frequency from 2900 to 3000 Hz from 0.04 to 0.08 seconds, shown in Figure B.3. The instantaneous frequency as a function of time for this signal is shown in Figure B.4.

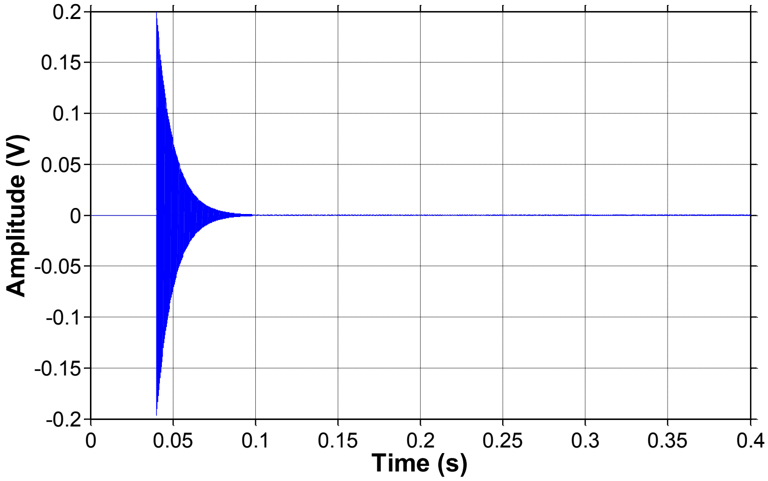

Figure B.3. Exponentially decaying chirp signal created in Matlab.

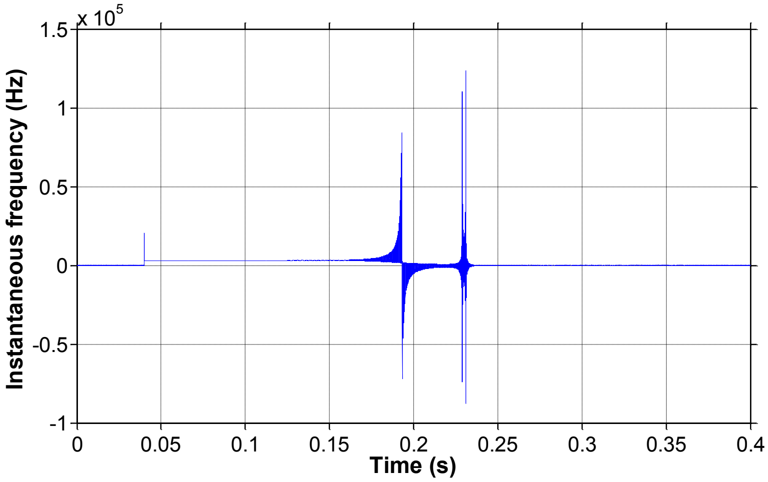

Figure B.4. Instantaneous frequency of simulated signal.

The estimation of instantaneous frequency using the Hilbert transform produces large frequencies after the signal decays; therefore, the analysis will focus on the region where the signal is concentrated (0.04 – 0.1s), shown in Figure B.5 and Figure B.6.

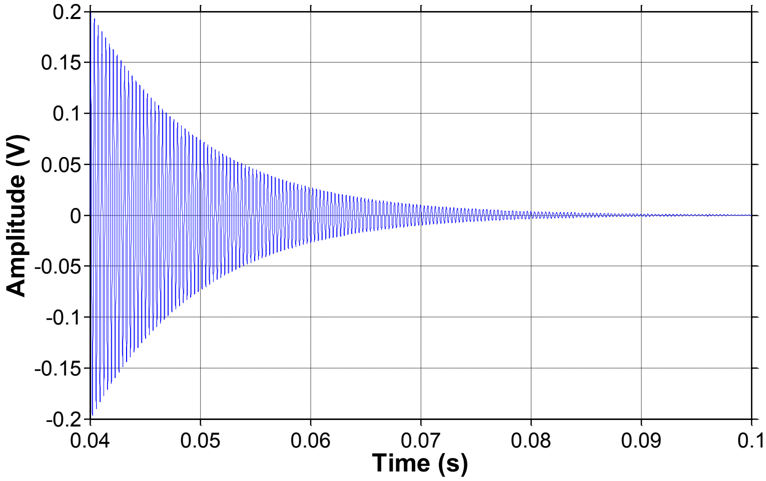

Figure B.5. Exponentially decaying chirp signal created in Matlab.

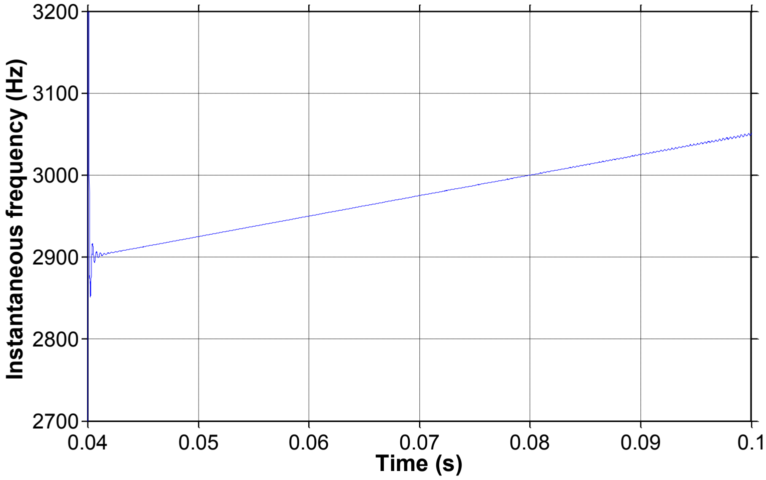

Figure B.6. Instantaneous frequency of simulated signal.

These results show that the Hilbert transform can be used to calculate instantaneous frequency for signals similar to ones produced by natural vibration of a specimen. As prescribed by the simulated signal, the instantaneous frequency changes from 2900 – 3000 Hz from 0.04-0.08s. For a simulated signal with increased damping, Figure B.7, the frequency change is also still visible, Figure B.8, but the oscillations in the approximate instantaneous frequency are much larger.

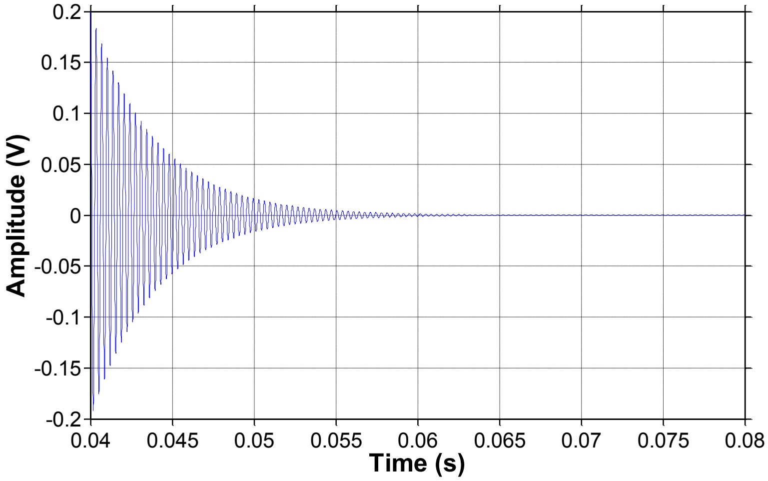

Figure B.7. Simulated signal with increased damping.

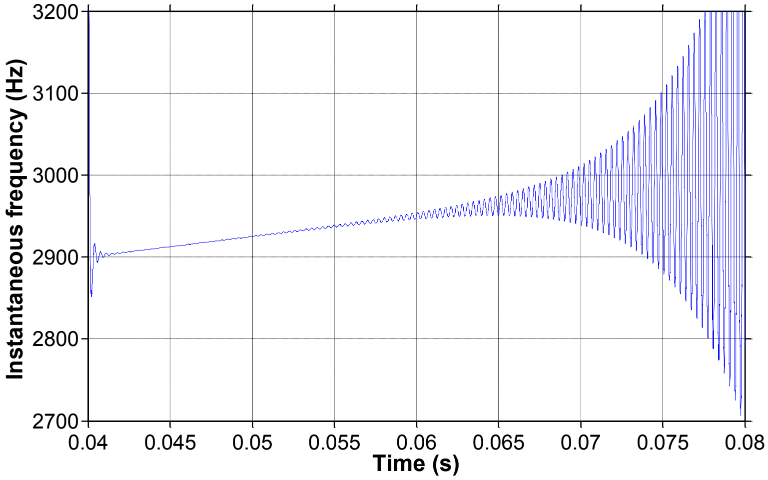

Figure B.8. Instantaneous frequency change with increased damping.

The result for an experimental signal, Figure B.9, however, does not produce the same result. Even though the overall signal is centered about the t-axis, the results do not yield any useful data, as shown in Figure B.10.

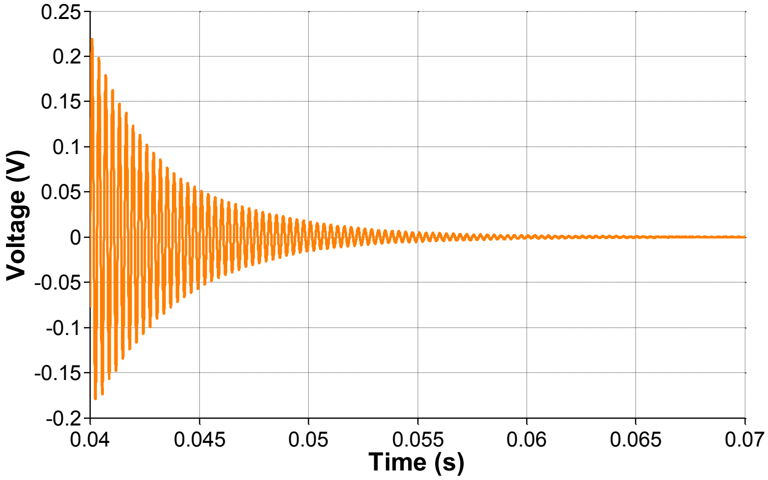

Figure B.9. Experimental signal.

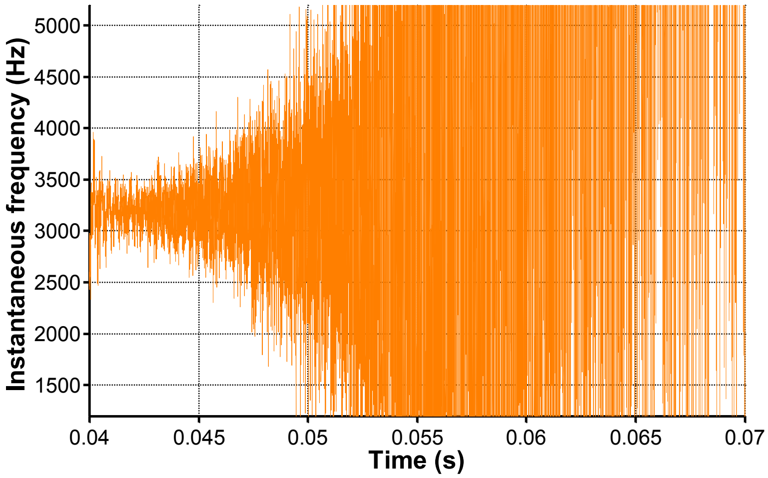

Figure B.10. Instantaneous frequency of real signal.

Applying the spectrogram, Figure B.11, also does not produce any useful data.

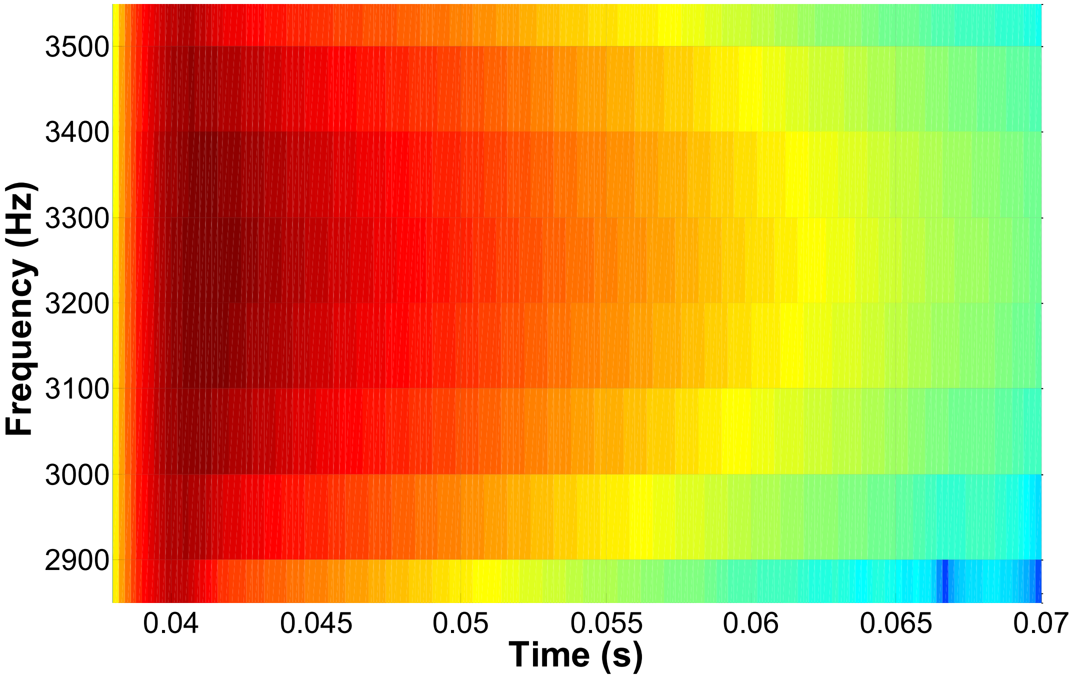

Figure B.11. Spectrogram of experimental signal.

From these results there is no indication of a change in resonance frequency as the signal amplitude decays.

REFERENCES

[1] B. Fournier, M.-A. Berube, K. J. Folliard, and M. Thomas, "Reoprt on the Diagnosis, Prognosis, and Mitigation of Alkali-Silica Reaction (ASR) in Transportation Structures," Fedral Highway Administration FHWA-HIF-09-004, 2010.

[2] K. Folliard, M. D. A. Thomas, and K. E. Kurtis, "Guidelines for the Use of Lithium to Mitigate or Prevent ASR in Concrete," Federal Highway Administration FHWA-RD-03-047, 2003.

[3] ASTM C 1293, "Standard Test method for Determination of Length Change of Concrete Due to Alkali-Silica Reaction." West Conshohocken, PA: ASTM International, 2008.

[4] ASTM C 1260, "Standard Test Method for Potential Alkali Reactivity of Aggregates (Mortar-Bar Method)." West Conshohocken, PA: ASTM International, 2007.

[5] ASTM C 1567, "Standard Test Method for Determining the Potential Alkali Reactivity of Combinations of Cementitious Materials and Aggregate (Accelerated Mortar-Bar Method)." West Conshohocken, PA: ASTM International, 2008.

[6] M. B. Haha, E. Gallucci, A. Guidoum, and K. L. Scrivener, "Relation of expansion due to alkali silica reaction to the degree of reaction measured by SEM image analysis," *Cement and Concrete Research,* vol. 37, pp. 1206-1214, 2007.

[7] P. B. Nagy, "Fatigue damage assessment by nonlinear ultrasonic materials characterization," *Ultrasonics,* vol. 36, pp. 375-381, 1998.

[8] L. A. Ostrovsky and P. A. Johnson, "Dynamic nonlinear elasticity in geomaterials," *Rivista del Nuovo Cimento,* vol. 24, pp. 1-46, 2001.

[9] M. Richardson, "Harmonic generation at an unbound interface. Part I: planar interface between semi-infinite media," *Int. J. Eng. Sci,* vol. 17, pp. 73–75, 1979.

[10] W. L. Morris, O. Buck, and R. V. Inman, "Acoustic harmonic generation due to fatigue damage in high-strength aluminum," *Journal of Applied Physics,* vol. 50, pp. 6737-6741, 1979.

[11] K. R. McCall and R. A. Guyer, "Equation of state and wave propagation in hysteretic nonlinear elastic materials," *Journal of Geophysical Research,* vol. 99, pp. 23887-97, 1994.

[12] J.-Y. Kim, J. Qu, L. J. Jacobs, J. W. Littles, and M. F. Savage, "Acoustic nonlinearity parameter due to microplasticity," *Journal of Nondestructive Evaluation,* vol. 25, pp. 28-36, 2006.

[13] J.-Y. Kim, L. J. Jacobs, J. Qu, and J. W. Littles, "Experimental characterization of fatigue damage in a nickel-base superalloy using nonlinear ultrasonic waves," *Journal of the Acoustical Society of America,* vol. 120, pp. 1266-1273, 2006.

[14] J. Herrmann, J.-Y. Kim, L. J. Jacobs, J. Qu, J. W. Littles, and M. F. Savage, "Assessment of material damage in a nickel-base superalloy using nonlinear Rayleigh surface waves," *Journal of Applied Physics,* vol. 99, 2006.

[15] K. E. A. Van Den Abeele, P. A. Johnson, and A. Sutin, "Nonlinear Elastic Wave Spectroscopy (NEWS) techniques to discern material damage, Part I: nonlinear wave modulation spectroscopy (NWMS)," *Research in Nondestructive Evaluation,* vol. 12, pp. 17-30, 2000.

[16] J. Chen, A. R. Jayapalan, J.-Y. Kim, K. E. Kurtis, and L. J. Jacobs, "Nonlinear wave modulation spectroscopy method for ultra-accelerated alkali-silica reaction assessment," *ACI Materials Journal,* vol. 106, pp. 340-348, 2009.

[17] X. J. Chen, J.-Y. Kim, K. E. Kurtis, J. Qu, C. W. Shen, and L. J. Jacobs, "Characterization of progressive microcracking in Portland cement mortar using nonlinear ultrasonics," *NDT and E International,* vol. 41, pp. 112-118, 2008.

[18] K. E. A. Van Den Abeele, J. Carmeliet, J. A. Ten Cate, and P. A. Johnson, "Nonlinear elastic wave spectroscopy (NEWS) techniques to discern material damage, Part II: single-mode nonlinear resonance acoustic spectroscopy," *Research in Nondestructive Evaluation,* vol. 12, pp. 31-42, 2000.

[19] C. Payan, V. Garnier, J. Moysan, and P. A. Johnson, "Applying nonlinear resonant ultrasound spectroscopy to improving thermal damage assessment in

concrete," *Journal of the Acoustical Society of America,* vol. 121, pp. EL125-EL130, 2007.

[20] M. Muller, A. Sutin, R. Guyer, M. Talmant, P. Laugier, and P. A. Johnson, "Nonlinear resonant ultrasound spectroscopy (NRUS) applied to damage assessment in bone," *Journal of the Acoustical Society of America,* vol. 118, pp. 3946-3952, 2005.

[21] P. A. Johnson, B. Zinszner, and P. N. J. Rasolofosaon, "Resonance and elastic nonlinear phenomena in rock," *Journal of Geophysical Research,* vol. 101, pp. 11553-64, 1996.

[22] K. Van Den Abeele and J. De Visscher, "Damage assessment in reinforced concrete using spectral and temporal nonlinear vibration techniques," *Cement and Concrete Research,* vol. 30, pp. 1453-1464, 2000.

[23] P. Antonaci, C. L. E. Bruno, A. S. Gliozzi, and M. Scalerandi, "Evolution of damage-induced nonlinearity in proximity of discontinuities in concrete," *International Journal of Solids and Structures,* vol. 47, pp. 1603-1610, 2010.

[24] C. L. E. Bruno, A. S. Gliozzi, M. Scalerandi, and P. Antonaci, "Analysis of elastic nonlinearity using the scaling subtraction method," *Physical Review B (Condensed Matter and Materials Physics),* vol. 79, p. 064108 (13 pp.), 2009.

[25] M. Scalerandi, A. S. Gliozzi, C. L. E. Bruno, and K. Van Den Abeele, "Nonlinear acoustic time reversal imaging using the scaling subtraction method," *Journal of Physics D: Applied Physics,* vol. 41, 2008.

[26] J. Chen, A. R. Jayapalan, J.-Y. Kim, K. E. Kurtis, and L. J. Jacobs, "Rapid evaluation of alkali-silica reactivity of aggregates using a nonlinear resonance spectroscopy technique," *Cement and Concrete Research,* vol. 40, pp. 914-923, 2010.

[27] K. J. Lesnicki, J.-Y. Kim, K. E. Kurtis, and L. J. Jacobs, "Characterization of alkali-silica reaction in concrete specimens using a nonlinear vibration technique," in *Reviews of Progress in Quantitative Nondestructive Evaluation*, San Diego, CA, 2010.

[28] J. A. Farny and S. H. Kosmatka, "Diagnosis and Control of Alkali-Aggregate Reactions in Concrete," Portland Cement Association IS413, 1997.

[29] P. K. Mehta and P. J. M. Montiero, *Concrete: Microstructure, Properties, and Materials*, 3 ed. New York: McGraw-Hill, 2006.

[30] Z. P. Bazant and A. Steffens, "Mathematical model for kinetics of alkali-silica reaction in concrete," *Cement and Concrete Research,* vol. 30, pp. 419-428, 2000.

[31] M. Thomas, B. Fournier, K. Folliard, J. Ideker, and M. Shehata, "Test methods for evaluating preventive measures for controlling expansion due to alkali-silica reaction in concrete," *Cement and Concrete Research,* vol. 36, pp. 1842-1856, 2006.

[32] ASTM C 490, "Standard Practice for Use of Apparatus for the Determination of Length Change of Hardened Cement Paste, Mortar, and Concrete." West Conshohocken, PA: ASTM International, 2009.

[33] AASHTO T-303-00, "Standard method of test for accelerated detection of potentially deleterious expansion of mortar bars due to alkali-silica reaction," in *Standard specifications for transportation materials and methods of sampling and testing Part 2B: Tests*, ed Washington D.C.: American Association of State Highway and Transportation Officials, 2006.

[34] I. Y. Solodov and B. A. Korshak, "Instability, chaos, and "memory" in acoustic-wave-crack interaction," *Physical Review Letters,* vol. 88, pp. 143031-143033, 2002.

[35] K. Van Den Abeele, "Multi-mode nonlinear resonance ultrasound spectroscopy for defect imaging: An analytical approach for the one-dimensional case," *Journal of the Acoustical Society of America,* vol. 122, pp. 73-90, 2007.

[36] R. A. Guyer, K. R. McCall, and K. Van Den Abeele, "Slow elastic dynamics in a resonant bar of rock," *Geophysical Research Letters,* vol. 25, pp. 1585-1588, 1998.

[37] J.-Y. Kim and J.-S. Lee, "A micromechanical model for nonlinear acoustic properties of interfaces between solids," *Journal of Applied Physics,* vol. 101, 2007.

[38] G. A. Gist, "Fluid effects on velocity and attenuation in sandstones," *Journal of the Acoustical Society of America,* vol. 96, pp. 1158-1158, 1994.

[39] J. H. Ginsberg, *Mechanical and Structural Vibrations: Theory and Applications*. New York: John Wiley & Sons, Inc., 2001.

[40] A. Ambardar, *Analog and digital signal processing*, 2 ed.: Brooks/Cole Publishing Company, 1999.

[41] L. Cohen, *Time-frequency Analysis*. Englewood Cliffs, New Jersey: Prentice Hall PTR, 1995.

[42] D. G. Zill and W. S. Wright, *Advanced Engineering Mathematics*, 4th ed. Sudbury, MA: Jones and Bartlett Publishers, LLC, 2011.

[43] E. Bedrosian, "A product theorem for Hilbert transforms," *Proceedings of the IEEE,* vol. 51, pp. 868-869, 1963.

[44] S. L. Marple Jr, "Computing the discrete-time `analytic' signal via FFT," *IEEE Transactions on Signal Processing,* vol. 47, pp. 2600-2603, 1999.

[45] A. V. Oppenheim, R. W. Schafer, and J. R. Buck, *Discrete-time Signal Processing*, 2nd ed. Upper Saddle River, NJ: Prentice-Hall, 1999.

[46] ASTM C 215, "Standard Test Method for Fundamental Transverse, Longitudinal, and Torsional Resonant Frequencies of Concrete Specimens." West Conshohocken, PA: ASTM International, 2008.

[47] ASTM E 1876, "Standard Test Method for Dynamic Young's Modulus, Shear Modulus, and Poisson's Ratio by Impulse Excitation of Vibration." West Conshohocken, PA: ASTM International, 2009.

[48] ASTM C 856, "Standard Practice for Petrographic Examination of Hardened Concrete." West Conshohocken, PA: ASTM International, 2004.

[49] K. Natesaiyer and K. C. Hover, "Insitu identification of ASR products in concrete," *Cement and Concrete Research,* vol. 18, pp. 455-463, 1988.

[50] M. Bentahar, H. El Aqra, R. E. Guerjouma, M. Griffa, and M. Scalerandi, "Hysteretic elasticity in damaged concrete: quantitative analysis of slow and fast

dynamics," *Physical Review B (Condensed Matter and Materials Physics),* vol. 73, pp. 14116-1, 2006.

[51] J. A. TenCate, E. Smith, L. W. Byers, and T. J. Shankland, "Slow dynamics experiments in solids with nonlinear mesoscopic elasticity," in *Nonlinear Acoustics at the Turn of the Millennium. ISNA 15. 15th International Symposium on Nonlinear Acoustics, 1-4 Sept. 1999*, USA, 2000, pp. 303-6.

[52] J. A. TenCate, E. Smith, and R. A. Guyer, "Universal slow dynamics in granular solids," *Physical Review Letters,* vol. 85, pp. 1020-1023, 2000.

[53] P. A. Johnson, R. A. Guyer, and L. A. Ostrovsky, "A nonlinear mesoscopic elastic class of materials," in *Nonlinear Acoustics at the Turn of the Millennium. ISNA 15. 15th International Symposium on Nonlinear Acoustics, 1-4 Sept. 1999*, USA, 2000, pp. 291-4.

[54] P. A. Johnson and X. Jia, "Nonlinear dynamics, granular media and dynamic earthquake triggering," *Nature,* vol. 437, pp. 871-874, 2005.

[55] R. A. Guyer and P. A. Johnson, "Nonlinear mesoscopic elasticity: Evidence for a new class of materials," *Physics Today,* vol. 52, pp. 30-36, 1999.

[56] K. Van Den Abeele, P. Y. Le Bas, B. Van Damme, and T. Katkowski, "Quantification of material nonlinearity in relation to microdamage density using nonlinear reverberation spectroscopy: Experimental and theoretical study," *Journal of the Acoustical Society of America,* vol. 126, pp. 963-972, 2009.

[57] ASTM E 2001, "Standard Guide for Resonant Ultrasound Spectroscopy for Defect Detection in Both Metallic and Non-metallic Parts." West Conshohocken, PA: ASTM International, 2008.